ISBN 978-82-326-5020-0 (printed ver.)
ISBN 978-82-326-5021-7 (electronic ver.)
ISSN 1503-8181

Ershad P. Zarandi

Doctoral thesis

Doctoral theses at NTNU, 2020:337

Ershad P. Zarandi

Multiaxial fatigue analysis of offshore mooring chains, considering the effects of residual stresses and corrosion pits

NTNU
Norwegian University of Science and Technology

Doctoral theses at NTNU, 2020:337

NTNU
Norwegian University of Science and Technology
Thesis for the Degree of
Philosophiae Doctor
Faculty of Engineering
Department of Structural Engineering

NTNU
Norwegian University of Science and Technology

NTNU

Ershad P. Zarandi

Multiaxial fatigue analysis of offshore mooring chains, considering the effects of residual stresses and corrosion pits

Thesis for the Degree of Philosophiae Doctor

Trondheim, November 2020

Norwegian University of Science and Technology
Faculty of Engineering
Department of Structural Engineering

NTNU
Norwegian University of
Science and Technology

NTNU
Norwegian University of Science and Technology

Thesis for the Degree of Philosophiae Doctor

Faculty of Engineering
Department of Structural Engineering

© Ershad P. Zarandi

ISBN 978-82-326-5020-0 (printed ver.)
ISBN 978-82-326-5021-7 (electronic ver.)
ISSN 1503-8181

Doctoral theses at NTNU, 2020:337

Printed by NTNU Grafisk senter

To my beloved Fatemeh and Vanja

Abstract

The integrity of the mooring lines used to anchor offshore facilities and floating platforms has been always desired while its continuous achievement has been challenging. Many mooring line failures have occurred in the last decades and the failure rate has been higher than the industry expectations. Several joint industry projects have been conducted and many mechanisms and phenomena have been identified to be influential on the fatigue life of mooring chains, which are the most susceptible elements in mooring lines.

In this thesis, an overview of the knowledge and experimental studies on the phenomena and mechanisms influencing the fatigue life of mooring chains has been made and the gaps in the state-of-the-art have been identified. The effects of corrosion pits and residual stresses on the fatigue crack initiation life of pitted mooring chains have been closely studied. A comprehensive study on the fatigue behavior and cyclic plasticity of the mooring chain high strength steel grade R4, which is broadly used in the offshore industry, has been conducted. The material's fatigue and cyclic plasticity parameters have been identified and calibrated against the experimental data. A rapid cyclic softening behavior has been observed from the material, which is of great importance when fatigue crack initiation and propagation are of interest. Multiaxial fatigue performance of the material has also been studied experimentally. A quick material hardening followed by softening has been observed when the material is subjected to biaxial (both proportional and non-proportional) loading. An advanced material model based on non-linear kinematic hardening combined with isotropic hardening has been calibrated to the experimental data obtained from small-scale uniaxial fatigue tests and used in the established finite element models of mooring chains to predict the residual stresses due to proof loading. Artificial hemispherical pits at the fatigue critical locations on a typical studless mooring chain were introduced to the FE models and strain localization at the pit sites was studied for different service load levels. Further, the residual stress redistribution due to corrosion pitting and cyclic service loads applied to large mooring chains has been investigated both numerically and experimentally using two different measurement techniques. Ultimately, fatigue crack initiation from the critical pit at the chain crown was assessed using a strain-energy based fatigue damage parameter and a critical plane approach to account for the stress multiaxiality, residual stresses, and corrosion pits effects. The predicted crack initiation lives from the two approaches were comparable and in the range of 15-40 % of the (total) experimental lives depending on the applied load level.

Preface

This thesis is submitted to the Norwegian University of Science and Technology (NTNU) for partial fulfilment of the requirements for the degree of Doctor of Philosophy in Structural Engineering.

This doctoral work has been performed at the Department of Structural Engineering under supervision of Professor Bjørn H. Skallerud and with co-supervision of Professors Jochen Köhler and Per J. Haagensen.

The experimental work conducted in this PhD project was financed by Equinor through the project KPN LifeMoor (RCN contract No: 280705).

Acknowledgements

It is a pleasure to express my gratitude to Professors Bjørn H. Skallerud, Jochen Köhler, and Per J. Haagensen for giving me the opportunity to study this topic. Professor Bjørn H. Skallerud served as the main supervisor and Professors Jochen Köhler and Per J. Haagensen as the co-supervisors. Their guidance, constructive comments, and continuous support throughout the course of this work are highly acknowledged.

I would like to thank my colleagues and friends at the structural engineering department who together created an international and productive research environment. I wish to thank Associate Professor Sigmund Ås for guidance on interpreting X-ray experimental data, Dr. Håkon Nordhagen (SINTEF) and Mr. Øystein Gabrielsen (Equinor) for their openness and technical discussions, Paul Qvale for diverse discussions and his assistance in the 3-point bending experiment. I am also grateful to Mr. Odd Nerdahl for his support in the lab, Oddvin Ørjasæter for his insightful comments regarding low-cycle fatigue tests, Dr. Egil Fagerholt for guidance on the digital image correlation (DIC) analyses, and Christian Frugone for his involvement and assistance in the uniaxial and 3-point bending fatigue experiments.

Acknowledgement is given to Equinor for providing test materials and financially supporting the experiments through the project KPN Lifemoor (RCN contract No: 280705).

Finally, I would like to thank my family for their encouragement and support throughout this work. A special thank you goes to my dear Fatemeh for her love and patience.

Ershad P. Zarandi

July 2020

Trondheim, Norway

Contents

List of Figures

List of Tables

Abbreviations

CP	Critical Plane
DIC	Digital Image Correlation
FEM	Finite Element Modeling
FS	Fatemi-Socie
HD	Hole Drilling
IP	In-Phase
JIP	Joint Industry Project
LEFM	Linear Elastic Fracture Mechanics
MBL	Minimum Breaking Load
ND	Neutron Diffraction
NTNU	Norwegian University of Science and Technology
OP	Out-of-Phase
OPB	Out-of-Plane Bending
PL	Proof Loading
RQ	Research Question
RS	Residual Stresses
SED	Strain Energy Density

1. Introduction

1.1. Background

The offshore industry has been growing in the past few decades due to the energy sources at sea being the center of petroleum engineers' attention. The number of offshore floating production storage and offloading systems, as a result, have increased globally [1]. To properly operate, these expensive systems require to be position fixed during operation. This is normally done utilizing mooring systems. Continuous operation of offshore facilities directly depends on the integrity of their mooring systems that keep these facilities in position. Offshore industry standards, e.g. refs. [2, 3], present guidelines for design and maintenance of mooring systems for different types of facilities. A mooring line can be made of elements such as steel chains, steel wire/fiber ropes, connectors, etc. Failure in any of these elements fails the entire mooring line causing tension increase in the adjacent lines. Multiple line failure may lead to catastrophic consequences. This, however, can be possibly avoided by planning regular and risk-based inspection programs at service time [4, 5].

The mooring system is designed to sustain the loads from waves, wind, and current during the 20- to 30-year service life of offshore facilities. However, these loads and above all the environmental impacts significantly depend on the geographical location where the facility is operating. Several mooring line failures have been observed and reported in the past years. Twenty-one incidents between the years 2001 and 2011 have been reported

by Ma et al. in ref. [6]. Chains, connectors, and wire ropes were identified as the top three susceptible components. Kvitrud in ref. [7] reported anchor line failures occurred in Norwegian Continental Shelf between the years 2010 and 2014, where fatigue and overload in chains were the main failure reasons. The failure rate was reported to be more than $9 * 10^{-3}$ per line-year in the studied time period. Fontaine et al. in ref. [1] investigated mooring line failures between the years 1997 and 2013. In total, 80 failures arisen to 55 ship-shape floating production units were studied, where almost half of which were associated with chains. The main cause of failure was identified to be fatigue or corrosion related. Further, the component's location in a mooring line was identified to be an influential factor in the mooring chain fatigue life. The failure rate was found to be $3.5 * 10^{-3}$ per facility-year. This is while the acceptable annual probability of failure is 10^{-3} for single line and 10^{-5} for multiple line failures [2].

The high rate of mooring line failures necessitates the improvements of the guidelines by investigating the influential factors on the fatigue life of mooring lines and specifically mooring chains that are widely used as the main element of mooring lines for offshore oil platforms. Several investigations have been carried out to enhance the understanding of phenomena and mechanisms e.g. tension-tension fatigue, out-of-plane bending (OPB), wear, corrosion, overload, manufacturing defects, and accidental damage to improve mooring lines integrity, monitoring, and inspection. The findings were reviewed in ref. [8]. The needs for improvement of corrosion/wear degradation models, a better understanding of OPB effects, and consideration of chain size and material in the fatigue analysis of mooring chains were emphasized.

Several joint industry projects (JIPs) have been conducted to investigate different phenomena and mechanisms influencing the integrity of mooring lines and more specifically mooring chains. The Mooring integrity JIP was conducted in two phases; in phase 1, the integrity of mooring systems was generally investigated, the influential factors on the failure of mooring systems were identified, and potential risks in case of mooring system failures were discussed [9], and in phase 2, some of the identified factors were studied more in details and the influence of proof loading (PL) on the fatigue life of mooring chains was highlighted [10]. The SCORCH (Seawater Corrosion of Ropes & CHains) JIP was conducted to inspect corrosion pits and examine the residual strength of heavily corroded mooring chains experimentally [11]. The work was continued in the Chain FEARS (Finite Element Analysis of Residual Strength) JIP by numerical analysis of the scanned geometry of severely corroded chains to assess their residual strength [12]. The chain OPB fatigue JIP was launched to experimentally and numerically study OPB in the chains at fairleads [13]. Although extensive experimental works have been carried out, not every factor influencing mooring line chains failure has been known and addressed properly to date. Recently, the FoCCs (Fatigue of Corroded Chains) JIP was formed to investigate the fatigue performance of corroded chains retrieved from service [14]. Also, the LifeMoor JIP is currently running to study the effects of corrosion and wear on the fatigue crack initiation and propagation life of mooring chains, and thus,

improve the mooring lines integrity and provide a cost-effective and safe lifetime extension of existing mooring lines.

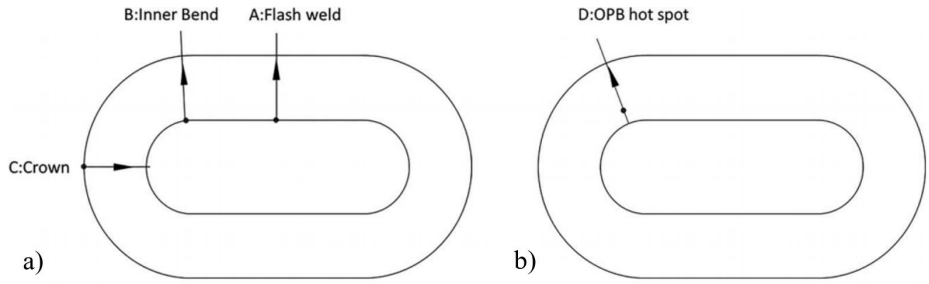

Figure 1: critical locations on a studless chain link subjected to a) T-T fatigue and b) OPB, curtesy of [15]

Figure 1 illustrates a typical studless offshore mooring chain as well as the locations that fatigue cracks are frequently observed. These locations experience high local stress values resulted from cyclic service loads and other mechanisms and phenomena such as residual stresses (RS) from the manufacturing process and PL, corrosion and/or wear, OPB. These phenomena and mechanisms are further explained in the next section.

Employing 3D scanning methods is beneficial in inspecting the chain links surfaces in assessing the material's strength degradations. The collected data can be used to plan for the inspection intervals, as well as, being a reference for repair and maintenance to avoid failures. Also, the scanned geometry can be used in e.g. a finite element model to estimate the remaining fatigue life of corroded chains. Figure 2 illustrates an example of a 3D surface scanning of a corroded chain link. However, the inspection of mooring lines is still challengeable due to the difficulties regarding inspection under seawater, long length of lines, inaccessible components such as anchors, and relatively high cost. Thus, any consideration and acts are appreciated to be taken in the design phase of mooring systems to reduce the probability of failure and ensure expected performance during the entire service life.

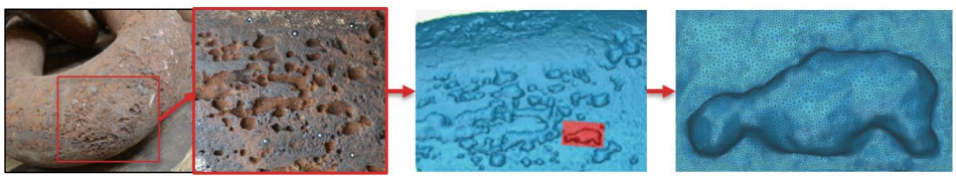

Figure 2: a) corrosion pits on a chain link surface, b) 3D scan of the surface, c) 3D finite element model of a corrosion pit, curtesy of [16]

1.2. Objectives and scope of the thesis

The main objective is to develop the understanding of phenomena correlating the fatigue life of mooring chains used in the offshore industry to improve their design and maintenance, and thus, enhance their reliability against failure. Further, the developed models can be used to quantitatively assess the fatigue life of corroded mooring chains already used at service and improve the knowledge for their lifetime extension. This is done by conducting small-scale and large-scale experiments as well as employing and developing theoretical and numerical models to account for the effects of corrosion pits and RS due to PL on mooring chains fatigue life. The chains have been broadly used within the offshore industry and are still in service. Thus, the outputs of this study can be valuable inputs to the industry standards and associates as well as being used for an in-service chain fatigue performance assessment to enable science-based decision making for the inspection intervals and chain replacement.

The overall research objectives are to:

- Understand the state-of-the-art in fatigue analysis of mooring chains and identify the most critical factors influencing fatigue life in these chains.
- Conduct small-scale uniaxial and biaxial fatigue tests to investigate the chain material response under monotonic and cyclic loadings.
- Develop an advanced material model calibrated to the experimental data to account for the material's transient and stable response under cyclic loadings.
- Establish numerical models using the calibrated material model to account for the effects of corrosion pits at fatigue critical locations, shown in Figure 1a, and RS due to PL on mooring chains fatigue crack initiation life.
- Conduct RS measurement on large-scale mooring chains to study RS changes over service life and validate the numerical results.

The overall scope of the project is dedicated to the mooring chains, as one of the most susceptible elements of mooring lines, used to anchor offshore production systems and installations. The focus will be on the prediction of fatigue crack initiation life of pitted chains under constant amplitude cyclic loads corresponding to the loading conditions used in the full-scale mooring chain fatigue tests representing harsh sea state loading conditions. The effects of RS due to PL and corrosion pits are taken into account and the suitability of the models developed in this project is assessed for 114mm diameter studless mooring chains made of steel grade R4. However, the developed models and framework are also applicable to the chains used in the offshore wind turbine and fish farms mooring systems.

The dynamic analysis of mooring systems as well as the probabilistic analysis of sea loads are out of the scope. OPB, twist, and wear are not considered herein, however, the implemented theory and principles are robust and can be applied to the cases where the mentioned issues are also present.

Figure 3: 3D scan of a studlink retrieved from service, curtesy of [17]

1.3. Research Design

After comprehensive research on the failures of mooring systems used in offshore facilities, mooring chains were identified to be the most critical elements in a mooring line, and fatigue and corrosion to be the main failure reasons. To date, little information is available regarding the fatigue assessment of pitted chains. Accordingly, the following research questions (RQ) have arisen in addressing this problem:

RQ1. How does the chain material perform under monotonic and cyclic loads?
RQ2. How is the material's fatigue performance under multiaxial loading condition?
RQ3. How are the RS distributed in a typical studless mooring chain and do they change over several years of service life? How to predict these RS using finite element modeling (FEM)? How accurate the predictions are comparing to experimental measurements?
RQ4. How to account for the effect of corrosion pits on the fatigue crack initiation life?
RQ5. How to incorporate the obtain knowledge from the studies on RS and corrosion pits effects into an advanced multiaxial fatigue analysis approach for pitted chains?

The following researches and studies have been conducted during this PhD project to find the answers the RQs:

- A comprehensive research on mooring systems used in offshore facilities with focus on their main critical elements (chains) to identify the influential factors and mechanisms on their fatigue life. The focus has been then put on the effects of corrosion pits and RS on the chains fatigue life to help filling the existing gap in the industry understanding of these phenomena.

- Uniaxial and biaxial fatigue tests on the small specimens cut from large mooring chains retrieved from service to:
  - Investigate the material's fatigue performance under different loading conditions and identify the correlated parameters.
  - Evaluate the materials cyclic softening and its effect on the
- Numerical simulation of the material's cyclic response and parameters calibration using the obtained experimental data.
- Development of analytical and numerical models to analyze the fatigue crack initiation of pitted mooring chains using the calibrated material model considering the chain material's transient and stable material response and multiaxial damage parameters e.g. strain-energy based and critical plane (CP) approaches.
- Investigation of the effects of:
  - A smooth surface hole resembling corrosion pits at the fatigue critical locations.
  - Multiaxial stress state resulted from service loads, geometry complexity of the chain link, and RS due to PL.
- RS measurements at certain location on large-scale chain links before and after several years of being at service to evaluate and calibrate the results of FE simulation of PL process and investigate RS redistribution over a service life.

1.4. Published papers and contributions

This thesis contributes to the sate-of-the-art by investigating the effects of RS due to PL and corrosion pits on the fatigue crack initiation life. Large-scale offshore mooring chains made of high strength steel were selected as the studied case. The work conducted in this PhD project has been presented at international conferences (Fatigue design 2019, Senlis, France and DP and anchoring of offshore installations 2020, Trondheim, Norway) and published in international peer-reviewed journals. As the first author of all three papers, I was responsible for establishing the models, designing the test programs, performing the calculations, simulations, analysis, providing the results, and writing the papers under the supervision of Prof. Bjørn H. Skallerud. He was the 2nd author of Paper 1 and 2 and the 3rd author of Paper 3 and provided valuable inputs, constructive comments, and corrections. Dr. Tung L. Lee was the 2nd author of Paper 3. He assisted me in performing the ND experiment and analyzing the test data and made helpful corrections and comments on the text of Paper 3. The main publications from this PhD project are:

Paper 1. Zarandi, E.P. and B.H. Skallerud, Cyclic behavior and strain energy-based fatigue damage analysis of mooring chains high strength steel. Marine

Structures, 2020. 70: p. 102703.
https://doi.org/10.1016/j.marstruc.2019.102703

Abstract:
This study investigates the low-cycle fatigue behavior of mooring chains high-strength steel grade R4 under different strain amplitudes and strain ratios at room temperature. A fatigue test program has been carried out on small low cycle fatigue specimens cut from large mooring chains. The experimental results characterize the cyclic stress-strain relationship, the mean stress relaxation behavior, and the cyclic plasticity parameters of the material. Strain energy density is correlated with fatigue life through a simple power-law expression and very well represented by Basquin-Coffin-Mansion relationship. Further, a non-linear elastic-plastic material model is calibrated to the experimental stress-strain curves and used for the estimation of energy dissipation in the specimens under applied cyclic loads. The predicted fatigue life using the calibrated material parameters demonstrates a close agreement with the experimental fatigue life. Numerical simulations are carried out to analyze local plastic straining and assess crack initiation at the pit site of corroded mooring chains considering the multiaxial stress state. An energy-based approach is employed to estimate the number of cycles needed for a crack to initiate from an existing corrosion pit.

Relevance to this thesis: This paper discusses answers to RQ1, RQ4, RQ5

Paper 2. Zarandi, E.P. and B.H. Skallerud, Experimental and numerical study of mooring chain residual stresses and implications for fatigue life. International Journal of Fatigue, 2020. 135: p. 105530.
https://doi.org/10.1016/j.ijfatigue.2020.105530

Abstract:
Residual stresses in large mooring chains were measured for the first time in this study. Two measurement techniques were employed (neutron diffraction and hole drilling). Elastic-plastic finite element simulation of the proof loading was conducted, and the computed residual stresses were compared to the experimental measurements. Further, the cyclic plasticity of the material was taken into account to investigate residual stress redistribution caused by introduction of corrosion pits and cyclic service loads. A critical damage parameter was employed to estimate fatigue crack initiation life of corroded mooring chains subjected to various service load levels considering the effect of residual stresses.

Relevance to this thesis: This paper discusses answers to RQ3, RQ4, RQ5

Paper 3. Zarandi, E.P., T.L. Lee, and B.H. Skallerud, Data on residual stresses of mooring chains measured by neutron diffraction and hole drilling techniques. Data in Brief, 2020. 30: p. 105587.
https://doi.org/10.1016/j.dib.2020.105587

Abstract:
Residual stresses in large offshore mooring chains have been measured for the first time and presented in this article. Two chain links with the same size and material, one only subjected to proof load and no cyclic service loads and the other exposed to service loads as well as the proof load, were selected for the experiment. The residual stresses just below the surface were measured using the hole-drilling technique and the neutron diffraction technique was employed for deeper measurements. The data can be used to investigate residual stress redistribution in the chain links because of material removal due to corrosion and cyclic service loads that the chains are exposed to during the service time. Moreover, the data can be used to validate numerical models for predicting residual stresses. A more detailed interpretation of the data presented in this article is provided in “Experimental and numerical study of mooring chain residual stresses and implications for fatigue life”.

Relevance to this thesis: This paper presents the findings regarding RQ 3

Table 1: Summary of the contributions to the state-of-the-art

Source	Research Question	Focus
Journal Paper 1	RQ1, RQ4, RQ5	• Material characterization and modeling • FE simulation of pitted mooring chains • Fatigue crack initiation life calculation using SED approach
Journal Paper 2	RQ3, RQ4, RQ5	• Experimental and numerical investigation of mooring chains residual stresses • Fatigue crack initiation life estimation of pitted mooring chains using a critical plane approach
Journal Paper 3	RQ3	• Experimental investigation of mooring chains residual stresses using two measurement techniques
This publication	RQ2	• Axial-torsional fatigue of the material

2. Fatigue of mooring chains

A brief overview of the topics relevant to this thesis is provided in this chapter. The effects of different factors and phenomena such as multiaxial loading, corrosion, and RS on the fatigue life are discussed in a general perspective, and a more subjective review of their effects on the fatigue life of offshore mooring chains is presented.

2.1. Mooring chain fatigue design rules

Currently, the fatigue life of mooring chains is estimated using linear damage accumulation models, and stress-life (S-N) or tension-life (T-N) curves, which are available in offshore industry standards, e.g. [3, 18]. These curves were constructed using the data collected from fatigue testing on average size mooring chains (mostly D=76 mm) under free corrosion in simulated seawater conditions in the lab [19]. The tests were run at a mean tension, normally 20% of the minimum breaking load (MBL), higher than what the chains are typically exposed to at sea (i.e.5-10% of MBL) [20]. Further, due to time and commercial limitations, the cyclic loading frequencies in the fatigue tests were selected to be higher than the wave frequency at sea. Consequently, the corrosion effect is underestimated, as this phenomenon is time-dependent [21, 22]. To account for the corrosion effect, DNVGL in ref. [2] defines a uniform corrosion allowance that varies between 0.2 to 1 mm/year reduction in the chain diameter depending on the chain location on a mooring line and the geographical location of a moored vessel. However, no consideration is given to the effect of corrosion pits at the chain link surface on fatigue life.

To date, the industry standards lack an explicit consideration of the effects of PL level and material grade on fatigue life of different size mooring chains [23]. The RS effect is embedded in the curves, as the chains were proof loaded before being fatigue tested. However, the proof load and RS distribution after the proof load removal vary by the chain material, dimension, and PL level [24-26]. Thus, caution is needed when larger chains are designed based on the guidelines' S-N or T-N curves, as this may result in inaccurate life estimations.

Further, fatigue calculation in the standards is limited to the links in a catenary, i.e. only tension to tension (T-T) fatigue is considered, while links at the line terminations are subjected to extra loads such as twist and/or OPB. It has also been revealed that OPB significantly reduces the fatigue life of mooring chains and the effect of twist is noticeable when the twist angle is more than 10 deg [15]. Several large-scale tests have been carried out to investigate OPB in newly manufactured mooring chains. As an outcome, a safety factor was recommended to be applied on the fatigue life of the chains subjected to OPB [2, 27]. In some cases, different factors, e.g. OPB, twist, and corrosion pitting, may correlate and accelerate damage development ending up with undesirable outcomes. Thus, a more advanced methodology explicitly accounting for the effects of different factors on the fatigue life of chains is crucial.

Linear elastic fracture mechanics (LEFM) has been employed to estimate fatigue crack propagation life of mooring chains, where semi-elliptical and semi-circular crack shapes were considered [28, 29]. Comparable life estimations to the S-N or T-N curve based approaches applying the safety factors recommended in the industry standards have achieved [15]. However, the choice of initial crack shape and size that are decisive factors in LEFM is still debatable.

It is known that the stress state affects the material behavior, especially when the load exceeds the yield strength of the material, stress-strain relationship under multiaxial and uniaxial loading can differ considerably [30]. Besides, crack initiation and propagation depend on the combination of the material and loading direction and amplitude. The standards recommend applying a minimum safety factor of 3 and 5 on the fatigue lives estimated using the T-N and S-N curves, respectively, to cover uncertainties at operational conditions and deviations from the testing conditions. Nevertheless, failures occur occasionally before the expected service life ends, and even move to the higher grades of steel failed to noticeably improve the fatigue performance of mooring chains [31].

In the following sub-sections, major phenomena and mechanisms affecting the fatigue life are briefly discussed and the approaches to account for these effects are reviewed.

2.2. Multiaxial loading consideration

Mechanical components subjected to fatigue are generally exposed to multiaxial variable/constant amplitude and in-phase/out-of-phase cyclic loads. Even under uniaxial loading, the stress state inside the component can be multiaxial due to the geometry complexity. Multiaxial stress state in a typical mooring chain can be as a result of OPB, twist, geometry complexity, RS, and local corrosion and wear.

Out-of-plane bending (OPB)

OPB refers to the bending of the chain link out of its main plane aligned with its elliptical shape, see Figure 4. An off-loading buoy has experienced failure due to OPB in four of its eight mooring lines in less than 8 months of being at service; this unforeseen incident has forced engineers to reconsider the design of the mooring system. Several experimental tests on the chains from the failed mooring lines have been carried out to better understand the mechanism of OPB, and to introduce an empirical expression to determine the OPB interlink stiffness, and subsequently OPB stress [27, 32-35]. Research has shown that OPB has a significant effect on the fatigue life of the chains near chain hawses and chain stoppers [36]. Elastic-plastic numerical simulations of large-scale mooring chains have shown that the chains that are subjected to T-T fatigue as well as OPB with only a 5 deg interlink angle have 20% shorter fatigue life comparing to those subjected to T-T fatigue only [15]. Rampi et al. in ref. [37] conducted full-scale chain fatigue tests including OPB and investigated the effects of parameters such as stress range, frequency, environment, chain size, and mean tension. It was observed that OPB replaces the hotspots and accordingly, the crack initiation location from the outer crown (which is normally observed in the chains subjected to T-T fatigue) to inner bend, as schematically shown in Figure 1b. Numerical simulation shows that shear stresses are maximum at a location in the inner bend part of the chain subjected to OPB [37].

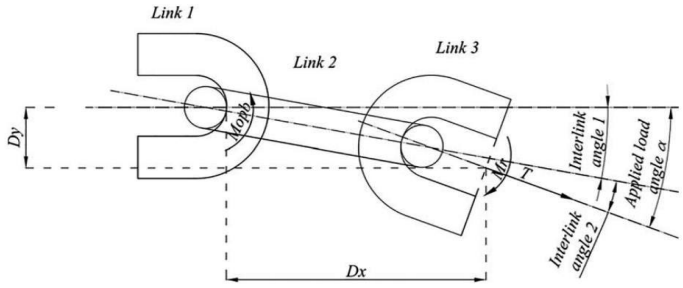

Figure 4: Representation of OPB of a chain link, curtesy of [15]

Experimental large-scale tests have revealed that OPB stress linearly depends on the interlink angle and friction [38]. Later it was shown that OPB is influenced by the chain

size, contact area between two adjacent links that is influenced by proof load, stopper arm, fairlead bearing friction, and mooring line pretension [33]. Further studies have empirically expressed OPB as a function of the mooring line tension, interlink friction coefficient at the links contact region, and interlink angle, as shown in Figure 4 [13]. OPB can be reduced by reducing any of the mentioned parameters. Mooring line tension and interlink friction coefficient cannot be easily altered as the former is decided based on different factors such as environmental and operational conditions and the type of mooring system, and the latter is dependent on the links hardness and surface roughness. Hence, the interlink angle should be kept within an acceptable range to minimize OPB. The use of rod connecting arms with low rotational friction and/or changing the chain hawse design was proved to be beneficial in reducing OPB and thus improve the mooring chain reliability [39-41]. Yet, OPB cannot be completely avoided, and thus, needs to be accounted for in the mooring chains design phase by means of multiaxial fatigue analysis approaches [23].

Chain twist

Since mooring lines may consist of fiber/steel wire ropes as well as chains, it is likely to have chains twisted after the mooring line being exposed to tensile loads as the ropes may not be intrinsically torque balanced. Chain twist may also occur during installation and anchoring step. Experimental, analytical, and numerical studies have been carried out to predict the torsional response of mooring chains and characterize the torque resulted from chain twist [15, 42, 43]. Figure 5, illustrates a stud-link chain subjected to 10kN axial load as well as approximately 30 deg twist per link. It is worth noting how the contact areas between adjacent links have been moved from its usual location, i.e. at the middle of the bent part, because of the chain twist. Numerical simulation of twisted studless mooring chains has revealed that there is a multiaxial stress state at the boundary of the contact area between two neighboring links that is dependent upon the mean tension, twist angle, and load amplitude [44]. If this is combined with OPB explained earlier, the resulted stresses may superimpose and the outcome can be detrimental.

Figure 5: Illustration of a stud-link chain under tension and twist, curtesy of [45]

The special shape of the bent part of a chain link generates a multiaxial stress state in this region even though the chain segment is being subjected to tension only. The shear stresses play an important role in crack initiation in this region resulting in fatigue failure at the bent part [31, 46]. This adds further complexity to the estimation of the chain fatigue life. The multiaxial stress can also be caused by phenomena such as RS from manufacturing and PL of mooring chains and corrosion pits at the chain surface. This is deliberated further in the following sub-sections.

2.3. Residual stress and mean load consideration

Manufacturing of mooring chains includes several stages, in which hot rolled steel bars are cut in pieces, bent, flash butt welded, heat-treated, and finally proof loaded. Each stage imposes large plastic deformations on the steel bars to turn them into the large mooring chains used in the offshore industry as the final product. It is assumed that RS due to manufacturing is released after heat treatment to a large extent. However, numerical simulation of the heat treatment process shows that some multiaxial RS remain in the chain as a result of nonhomogeneous plastic deformation caused by different heating/cooling times of the material at the surface and in the core of a chain. This phenomenon is more pronounced in larger chains [26]. PL includes axially loading chains up to 70% of the chain MBL to assure their suitability for being used at service. The proof load level depends on the chain size and material and is specified in the industry standards e.g. [47]. As a result of PL, high RS are introduced to the chains due to excessive plastic straining. Depending on the location on a chain link, these stresses may be compressive or tensile [24]. It is well known that tensile RS are harmful and compressive ones are beneficial when a component is subjected to fatigue loadings. Therefore, it is crucial to know how the RS are distributed in a mooring chain to better predict its fatigue life.

Numerical studies have shown that improved fatigue life estimation can be achieved when the RS due to PL are accounted for [23]. Tension-tension fatigue testing of new proof loaded small anchor chains has highlighted the beneficial effect of RS due to PL, with a higher PL level resulting in longer fatigue life. [46, 48]. This is because of the compressive RS due to PL that exists at the fatigue critical locations on a chain link, e.g. at the outer crown as shown in Figure 1 [49]. However, RS may redistribute/relax in a component. Experimental investigations have shown that RS relaxation depends on the initial RS field, material yield stress, load amplitude, and the number of cycles [50]. RS in mooring chains may also redistribute due to cyclic service loads and the formation of corrosion pits at chain surfaces. Thus, the prediction of the initial and stable RS field in mooring chains are essential for the estimation of the new chains' fatigue life and the remaining fatigue capacity of the chains already being at service. Further, the FE predictions need to be validated against RS measurement data. This has been successfully conducted and presented in Paper 2 and Paper 3 appended to this thesis.

Similar to RS, mean tension has also a significant effect on the mooring chains fatigue life and thus, a mean load correction needs to be applied on the standards' S-N or T-N curves as they were constructed based on fatigue tests with a mean tension of 20% of the chains MBL, which is much higher than the mean tension at service i.e. 5-10% of MBL [51, 52]. Alternatively, a nonlinear FEM tied with a multiaxial fatigue damage parameter, e.g. energy-based or CP approaches, can be employed to account for the effects of multiaxial loading, RS, and corrosion pits in addition to the mean tension effect on the fatigue crack initiation life of mooring chains. The suitability of these fatigue damage parameters has been evaluated for studless pitted mooring chains and presented in Paper 1 and Paper 2 appended to this thesis.

2.4. Corrosion consideration

At present, the industry standards recommend to account for the effect of uniform corrosion and wear on the mooring chains via an annual reduction of chain bar diameter. Numerical investigations have shown that although uniform corrosion decreases the chain MBL slightly, it significantly increases the annual probability of failure as the chain is further corroded [53]. Some research has been conducted to assess the residual breaking strength of these severely corroded chains, see e.g. [11, 12, 54]. It was found that despite the severe material loss and reduction in the chain cross-section, the residual strength of these chains was 80-90 % of MBL. Although uniform corrosion decreases the chain MBL slightly, numerical investigations have shown that it significantly increases the annual probability of failure as the chain is further corroded [53].

Mooring lines inspection at different stages of their service life has revealed that some mooring chains occasionally experience severe local corrosion largely due to marine growth [12] or local wear at the chains contact region and the touch-down zone [55]. To investigate the effects of large corrosion pits on the fatigue performance of mooring chains, Wang et al. in ref [56] established an experimental program, in which big artificial pits were manufactured on the non-proof loaded newly produced chains. SCF was investigated at the pit sites and a good agreement between the fatigue hotspots determined by FEM and failure locations in the tested chains was observed. However, the fatigue life of the tested chains does not represent the life of severely corroded chains at service, as the tested chains were not proof loaded, and thus, no RS was present in the chains.

Even smaller corrosion pits act as stress raisers and the higher local stress cycling at the pit site can accelerate pit to crack transition [57-59]. To investigate the effect of corrosion, Rampi and Vargas in ref. [60] conducted fatigue tests on small-scale cylindrical samples cut from the chain material and defined endurance limits for the Dang Van fatigue criterion for both corroded and non-corroded samples. For the fatigue loads considered, corroded samples had an endurance limit approximately 40% lower compared to the non-corroded samples.

The significant effect of corrosion on mooring chains fatigue life has been experimentally shown since 1996 [21]. More subjective experimental work has been carried out to investigate the T-T fatigue performance of large pitted mooring chains retrieved from service [14, 20, 61]. Fatigue cracks were mainly observed at the outer crown of the failed chains and initiation sites were recognized to be from corrosion pits. FEM with a linear elastic material model was employed to investigate stress intensity factors (SIFs) around the straight and semi-circular cracks at the crown of both proof loaded and non-proof loaded chains. SIFs were shown to be directly related to the applied load, and smaller SIFs were calculated for the proof loaded chains indicating the beneficial effect of RS due to PL at the considered cracked regions [62]. A similar study was conducted on a geometry that was built using the data from 3D scanning of corroded chains at service [63]. The results have revealed that the most destructive cracks and pits the those formed at the chain crown.

To date, no explicit consideration regarding the effects of corrosion pits on the chain fatigue life exists in the industry guidelines and the fatigue strength of corroded chains is still debatable. The standards S-N and T-N curves were constructed using the data from new chains tested in simulated seawater conditions and at a higher frequency than what the chains experience at sea. This, however, underestimates the corrosion effect as this phenomenon needs time to act. Thus, these curves cannot be used to estimate the remaining fatigue life of corroded mooring chains. Instead, local analyses should be conducted on the pitted chains and the data from small-scale fatigue test specimens would be a better tool for comparison. Hence, a quantitative understanding of fatigue crack initiation on pitted chain links is essential for a more reliable fatigue life prediction. This study has been conducted and presented in Paper 1 appended to this thesis.

2.5. Multiaxial fatigue analysis

To obtain a better prediction of the mooring chain fatigue life considering the effects of the phenomena and mechanisms explained earlier, the employment of a multiaxial fatigue damage parameter is essential. Strain-energy based and critical plan approaches have shown to be applicable to a wide range of engineering materials and applications, and thus, suitable for the case of mooring chains.

Lately, the Dang Van fatigue damage parameter [64], a CP approach, has been employed to estimate the mooring chains fatigue crack initiation life considering the effects of RS and OPB [37, 65]. Conservative life predictions were obtained due to the presence of high compressive hydrostatic stress existing at the critical points considered [65]. Further, only an ideal new chain geometry was considered, and the corrosion effects were not accounted for. The Dang Van criterion is applicable when high cycle fatigue is expected and the loads are low enough to keep the stress levels in the material within the elastic domain. However, corrosion pits are created at the chain surface shortly after these chains being at service, and as discussed earlier, the stress levels at the pit site are much higher

than the nominal stresses. Consequently, cyclic plasticity is expected to occur, and the assumptions for the applicability of the Dang Van criterion are doubted.

Strain-energy based approaches, e.g. see ref. [66], and the Fatemi-Socie (FS) damage parameter (a CP approach) [67], however, have shown to be applicable to the cases where compressive RS and cyclic plasticity exist, and thus, suitable for the fatigue crack initiation life estimations of pitted chains. For cylindrical specimens, the SED approach was shown to result in better life predictions comparing to the classic nominal stress-based approach [68]. Both approaches are capable of accounting for the multiaxial loading as well as the mean load effect without extra modification e.g. SWT, Goodman, etc. The applicability of these two approaches have been evaluated for the case of mooring chains and presented in Paper 1 and 2.

3. Context and Research Design

3.1. Research Goal

The main goal of the project is to establish numerical and analytical models to account for the effects of corrosion pits, multiaxial stress state, and RS on fatigue crack initiation life of corroded chain links. As discussed earlier, many JIPs have been conducted to experimentally investigate the effects of corrosion on the mooring chain fatigue life. Since the tests were carried out at higher frequency and load levels than what mooring lines are subjected to at service, the tests are somewhat fatigue biased and the effect of corrosion is underestimated. The full-scale tests are, however, costly and time consuming and the output of them is limited. Thus, it is of high necessity to combine the full-scale fatigue tests with small-scale tests to evaluate the materials response at different loading conditions and environments and investigate the effects of influential factors on fatigue life more closely. Numerical simulations can be used to estimate the remaining life of corroded chains at service. An advanced material model that accounts for the material's cyclic response can be employed in FE simulations. If the actual surface topology of a corroded chain is available by 3D scanning tools, the residual life of corroded chains can be estimated using fatigue approaches such as strain energy density (SED) or CP approach.

The work presented here contributes to the state-of-the-art by developing models with the aim to increase the understanding the effects of RS and ideal geometry (hemispherical) corrosion pits on fatigue crack initiation life, and thus, enhance the reliability of offshore mooring chains against failure. This has been done by means of experimental work as

well as analytical and numerical models. To reach the main goal of the research, several investigations and studies were conducted to address the arisen research questions mentioned in Sec. 1.3.

3.2. Research Process

In this project 114 mm diameter offshore studless mooring chains made of high strength steel grade R4 were chosen as the case study. This type of chain has been broadly used in offshore mooring systems. Thus, the outputs of this study can be valuable inputs to the industry standards and associates as well as being used for an in-service chain fatigue performance assessment to enable science-based decision making for the inspection intervals and chain replacement.

To address the goal of the project, FE models of studless mooring chains have been established to investigate the effects of RS and corrosion pits on the fatigue crack initiation life. The employed material model was calibrated to the small-scale uniaxial fatigue test data, where the specimens were cut from the chains retrieved from service. Later, the stress-strain history at the hotspots at the pit sites on the modeled chain link were used in a strain-based fatigue damage parameter and a CP approach to estimate the number of cycles required for a crack to initiate from the considered pits located at the frequently observed fatigue cracks on real chain links. Further, RS due to PL were predicted and their redistribution over service life was studied and the results from numerical simulation were compared with the measurements using ND and HD techniques. The procedure mentioned above is further outlined in the following sub-sections.

3.2.1. Small-scale fatigue tests

Three small-scale test programs have been designed and conducted; uniaxial strain-controlled fatigue test, axial-torsional strain-controlled fatigue test, and three-point-bending test to investigate RQ1, RQ2, and RQ4 respectively.

Uniaxial cyclic plasticity test

The details on the uniaxial test program and setup are outlined in Paper1, and the results were discussed thoroughly. The data was employed to establish the materials cyclic stress-strain curve and characterize the material's fatigue parameters. Since the strain levels were selected such that the material experiences cyclic plasticity, the data were also employed to calibrate the hardening parameters of the material.

Axial-torsional cyclic plasticity test

The finite element simulation of mooring chains subjected to a typical service load shows that due to the complex geometry of the chains and RS, the stress state in the chains is multiaxial even if the chain is subjected to T-T fatigue only. Besides, service loads e.g. twist and OPB yield high shear stresses in the bent part of a chain link. Therefore, it was of interest to investigate the material's fatigue performance under multiaxial loading condition. Accordingly, the axial-torsional was programed and conducted.

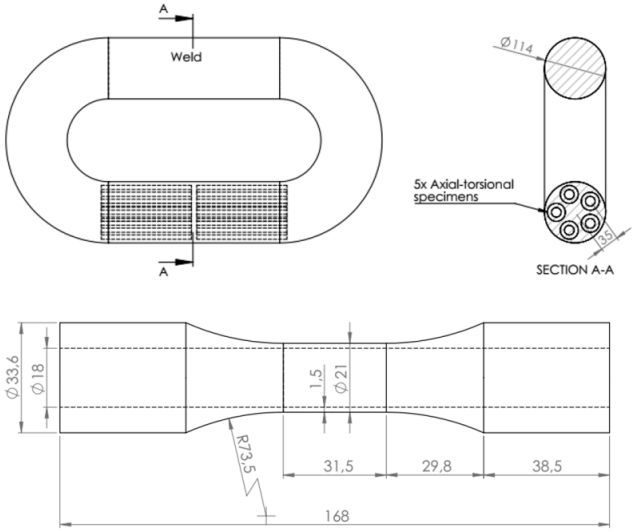

Figure 6: Details of the axial-torsional test specimens, dimensions in mm

The samples were machined out from the straight part (non-welded side) of a 114 mm diameter chain link grade R4. The specimens were polished in a drilling machine using first a 320- and then a 600-grit sandpaper. The final polishing stage was done longitudinally using a 1000-grit sandpaper to remove circumferential machining marks and generate a smooth surface (with roughness no higher than 0.2µm). The geometry of the specimens is according to ASTM E606 [69] and illustrated in Figure 6. The ASTM E2207 [70] procedure was employed for the axial-torsional strain-controlled cyclic tests. The tests were carried out in Instron 8550 test rig with 100 kN axial load and 1000 N.m torque capacity. The test frequency was 0.125Hz. The axial and torsional strain was measured continuously throughout each test using a calibrated Epsilon's axial-torsional extensometer (model: 3550-025M-005-003-ST) attached to the specimen as illustrated in Figure 7. The triangular waveform was used for the straining of the specimens as it provides a constant effective strain rate. Failure was defined based on a 50% tensile load/torque drop, i.e. the ratio of the maximum tensile load/torque at the cycle of failure

goes below 50% of that at the first cycle. The experiment included both in-phase and out-of-phase axial-torsional fatigue tests. Two axial strain amplitudes of 0.0045 and 0.006 and one torsional strain amplitude of 0.0052 were used. The test program was Single-step and fully reversed ($R_\varepsilon = -1$). All experiments were conducted in room temperature and 200 data points per cycle and for cycles 1, 2, 3, …, 10, 20, 30, …, 100, 200, 300, …, 1000, 2000, 3000, … were collected for data analyses.

Figure 7: Illustration of the axial-torsional extensometer mounted on a test specimen

Effective stresses (σ_{eff}) and strains (ϵ_{eff}) at different in-phase (IP) and out-of-phase (OP) load levels are defined based on von Mises criterion as follows:

$$\sigma_{eff} = \sqrt{\frac{3}{2}\sigma' : \sigma'} \quad , \quad \varepsilon_{eff} = \sqrt{\frac{2}{3}\varepsilon' : \varepsilon'} \tag{1}$$

Where σ' and ε' are the deviatoric stress and strain respectively. For the considered axial-torsional loading with Poisson's ratio of 0.5, ε_{eff} can be expressed as:

$$\varepsilon_{a,eff} = \sqrt{\varepsilon_a^2 + \frac{1}{3}\gamma_a^2} \tag{2}$$

where ε_a and γ_a are the axial and shear strain amplitudes respectively.

Three-point-bending (3PB) fatigue test

This experiment has been designed to investigate the effects RS on the crack initiation life from a manufactured pit on the surface of the square-section specimens with flat surfaces cut from the straight parts (non-welded side) of two chain links retrieved from service. The specimens are schematically illustrated in Figure 8. The specimen surfaces were ground using NORTON 5SG 46 G12VXP grinding stone with a rotational speed of $3000\ rpm$. Later, the specimens were divided into 2 groups. The first group of specimens was preloaded-unloaded at the test rig with a $44\ kN$ force to generate compressive RS at the region, where artificial pits were going to be manufactured in a later stage. The idea was to investigate the crack initiation from a pit at the presence of compressive RS. The specimens of the second group were not preloaded, and thus, no RS existed in them. A $3\ mm$ diameter hemispherical artificial pit was milled in the middle of each specimen of both groups, as shown in Figure 8, using a SECO mill rotating at $12000\ rpm$ in a Mazak VCN-530C milling machine. The feed rate was $180 mm/min$ for the non-preloaded specimens and $0.2 mm/min$ for the preloaded specimens to keep the RS field as less affected as possible. The specimens' surfaces with the artificial pits were later painted for the DIC study. The specimens were fatigue tested in a 250 kN Instron testing rig with the test setup shown in Figure 9. Details of the load levels are presented in Table 2. The cycle frequency was $3\ Hz$. A 3D DIC setup was employed to study the axial strain localization at the artificial pit sites and monitor the crack initiation and its width growth. Two cameras were used and placed on both sides of the specimen as shown in Figure 10. Pictures were taken every 100 cycles and at the maximum and minimum of the applied load. Failure was defined to occur when the deflection at maximum load (the displacement along the loading direction in the middle of the specimen with respect to the non-loaded specimen) was 4 times larger than that at the first cycle:

$$\left|d_{Load\_max}^{at\ failure}\right| \geq 4 * \left|d_{Load\_max}^{at\ 1st\ cycle}\right| \tag{3}$$

where $d_{Load\_max}^{at\ failure}$ and $d_{Load\_max}^{at\ 1st\ cycle}$ are the deflections at the maximum applied load at the time of failure and at the first cycle respectively.

The third group of specimens with the same size as the first two groups were cut at the surface of the chains, and thus, have one surface with actual corrosion pits instead of a manufactured pit. These tests will be conducted in the near future and the results of this experiment as well as the DIC analysis will be discussed in a separate publication.

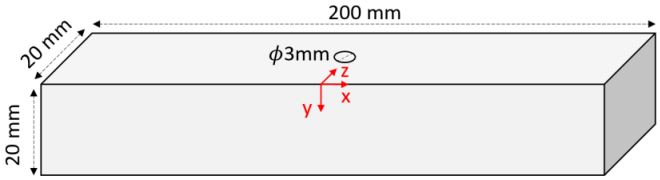

Figure 8: Schematic of the 3PB fatigue test specimen

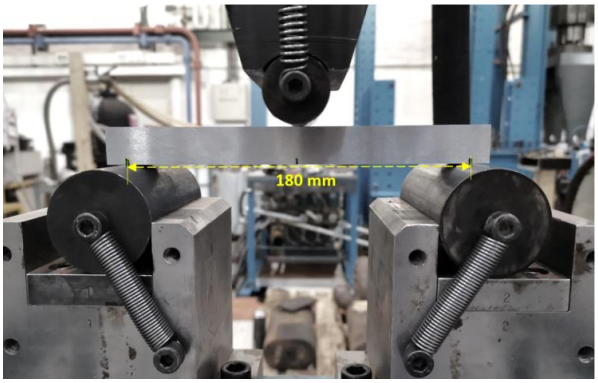

Figure 9: The 3PB fatigue test setup. The surface with the artificial pit is facing down

Figure 10: The DIC camera setup, one camera on either side of the specimen

Table 2: Details of the loading cases used in the 3PB fatigue tests

Loading case	Preload-unload [kN]	Mean load [kN]	Load amp [kN]	Load ratio ($R = L_{min}/L_{max}$)
1	0	-15	10	0.2
2	-44	-15	10	0.2
3	0	-18	12	0.2
4	-44	-18	12	0.2

3.2.2. Material characterization

Earlier studies have shown that using a linear-elastic material model in FEM may result in incorrect and possibly non-conservative life estimations for mooring chains [23]. Thus, the material's cyclic plasticity and fatigue performances have been evaluated and studied through the uniaxial fatigue test program and numerical simulations. MATLAB scripts have been written and optimized to simulate the material's response at high cyclic strain ranges, and thus, its cyclic softening behavior. A kinematic hardening based on Armstrong-Frederick [71] combined with isotropic hardening was used. The Armstrong-Frederick plasticity model has been shown to be capable of accounting for phenomena e.g. cyclic hardening/softening, ratcheting, and non-proportional hardening [72, 73]. Further, the cyclic stress-strain curve and Basquin-Coffin-Mansion strain amplitude vs life curve were constructed for the material, and the expression's parameters were calibrated. SED was shown to be well correlated with the fatigue life of the uniaxial fatigue test specimens' lives, and the associated material constants were identified. More details on the mentioned studies and the material characterization are provided in Paper 1.

3.2.3. Numerical simulation

A 3D model of a complete chain link and two neighboring half chain links has been constructed in Abaqus 6.14. The calibrated elastic-plastic material model was employed to capture the material softening at the pitted areas at the surface of the modeled chain link. The pits were introduced to the models as hemispherical smooth surface holes at three fatigue critical location shown in Figure 1a. Details on the loading and boundary conditions as well as the mesh study result are presented in Paper 1.

The 3PB test has also been simulated in Abaqus 6.14. The support rollers and the loading roller were considered to be rigid parts and the 3PB test specimen was positioned between them as shown in Figure 11a. The model was meshed using first-order hexahedral elements with reduced integration schemes (C3D8R) and a finer mesh was employed in the middle of the specimens, where an artificial pit was supposed to be modeled, to obtain the local strains and stresses in this region accurately. All degrees of freedom of the 3

rollers except the displacement of the loading roller along the y-axis were constrained. To keep the computational costs low, only one-quarter of the volume was modeled and two symmetry planes (i.e. x-y and y-z planes) were used. The loads were applied as concentrated forces on a reference point at the center of the loading roller. The reference point was kinematically coupled with the loading roller in all directions. The pre-loading process consisted of applying a $44\ kN$ force on the reference point and unloading. Only the specimens in group 1 were preloaded while the preloading step was suppressed for the specimens in group 2. Later, a hemispherical pit with a diameter of $3\ mm$ was introduced to the model by removing the elements inside the pit. The final step was to apply fatigue loads corresponding to those used in the experiments.

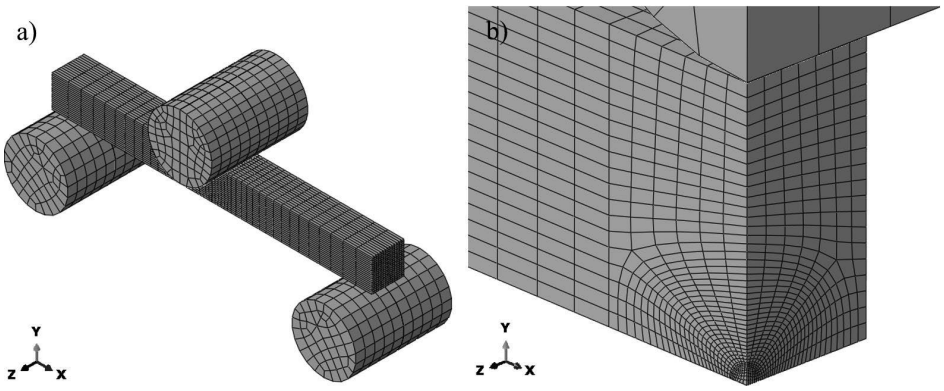

Figure 11: a) illustration of the 3D model of the 3PB test setup, and b) refined mesh in the pit site

3.2.4. Residual stresses measurement

As discussed in Sec. 2.3. RS have a noticeable effect on the mooring chain fatigue life. However, little attention has been paid to the calculation of RS along large mooring chains and no RS measurement has been conducted on these chains. Therefore, in this PhD project, a test program was designed to measure RS at the chain crown and straight parts using the neutron diffraction (ND) and hole drilling techniques (HD). Two 114mm diameter chain links made of steel grade R4 and produced by the same manufacturer were selected for the experiment; one was exposed to the service loads and seawater for 18 years and the other was 10 years old but never exposed to service loads as it was laid over the vessel's deck. These, two links had experienced different corrosion levels and thus, larger corrosion pits were seen on the older link. The choice of links was made purposefully to investigate the effects of corrosion and cyclic service loads on the redistribution of RS. Later, the obtained data were analyzed and used as a validation tool for the FE predictions of RS due to PL.

The experimental setups have shown in Figure 12 and Figure 13. Further details of the experimental setup, used equipment, and test procedure as well as the raw and analyzed data is provided in Paper 3 and the interpretation of the obtained data is presented in Paper 2 appended to this thesis.

Figure 12: The HD experimental setup. Due to the limited space between the chain straight parts, only RS at the chain outer surface were measurements using the HD technique

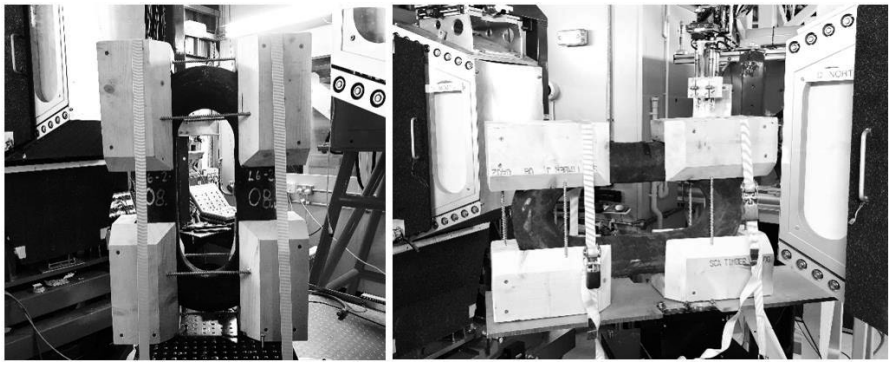

Figure 13: The ND experimental setup. The links are repositioned to enable the 3-axis RS measurement, curtesy of [74]

3.2.5. Fatigue crack initiation life estimation

To address the main goal of this project that was to investigate the effects of corrosion pits and RS on the fatigue crack initiation life of offshore mooring chains, the obtained data from experimental activities described earlier along with the developed FE models

and calibrated material model have been used to find the stress-strain history the pit sites at the fatigue critical locations on the chain link, shown in Figure 1a. The stress-strain history was then used to investigate the material softening and RS redistribution in the material enclosing the pits. Further, the strain energy dissipation at the critical location on the pits was employed as a fatigue damage parameter to estimate the crack initiation from the considered pits. The methodology is described, and the results are discussed and presented in Paper 1. CP approaches have also shown to be beneficial when the stress state in the component is multiaxial. Thus, FS fatigue damage parameter combined with Rossel-Fatemi hardness method, which has shown to yield good life predictions for a wide range of steels, has been employed as an alternative crack initiation method to the strain energy-based approach used in Paper 1. The methodology and results from this approach have been explained and discussed in Paper 2.

4. Results & discussions

The experimental and numerical results from the studies described in Sec. 3.2. are presented in this chapter. The results from the numerical modeling, uniaxial cyclic plasticity testing, and RS measurement using the ND and HD techniques are briefly presented herein. Details on these studies can be found in the appended papers. Further, the results from the axial-torsional cyclic plasticity testing are presented and thoroughly discussed in this chapter. Finally, the 3PB test (which is in progress at the time being) data will be presented and discussed at the end of this chapter.

The results presented and discussed in this thesis along with the appended papers contribute to the state-of-the-art by filling the gap in the multiaxial fatigue analysis of mooring chains exposed to the corrosive marine environment and different loadings sourced from waves, wind, current, OPB, twist, etc. as well as RS.

4.1. Experimental and numerical study of uniaxial cyclic plasticity

The experimental results from the uniaxial fatigue test program have been analyzed and presented in Paper 1. A comprehensive study on the material behavior under monotonic and cyclic loadings was conducted. The material fatigue parameters were identified, and the cyclic plasticity parameters were calibrated using the data obtained from the uniaxial test program. Further, the strain-life and strain energy-life curves have been constructed and decent life estimations have been achieved using each curve. Moreover, the material softening was studied by tracking the maximum and minimum stress amplitudes as the number of load cycles increased. Numerical simulations have been carried out to simulate the material cyclic response and accordingly, energy dissipation per cycle. This was done via MATLAB scripts coded and developed by the author of this thesis. A good agreement

was observed between the experimental and simulated stress-strain curves at different load cycles. The material cyclic plasticity parameters were calibrated for the tested strain ranges and presented in Paper 1. The calibrated material model was later used in a FE model of pitted chains subjected to various service load levels. The first 1000 load cycles were simulated and the energy dissipation at the pit sites was studied. The pit located at the chain crown was identified to be the most critical pit among the considered pits at the fatigue critical locations. This was in absolute agreement with the experimental observations from full-scale fatigue testing of corroded chains. The dissipation at the critical point at the pit site together with the experimental data were used to predict the fatigue crack initiation life from the considered pit. Further details on the numerical and experimental results are found in Paper 1 appended to this thesis.

4.2. Experimental and numerical study of residual stress

The raw and analyzed data from RS measurement experiment has been presented in Paper 3. It can be seen that RS field in the measurement points is multiaxial and they are mostly compressive. The numerical simulation of PL has been conducted and the residual stress field around a pit at the chain crown was investigated both before and after applying service loads. The results of this study have been presented in Paper 2. A good agreement between numerical predictions of the largest magnitude RS (i.e. the longitudinal RS) and the experimental measurements have been achieved. Further, the stress-strain values at the critical point at the pit site were used in the FS CP damage parameter, and crack initiation life from the considered pit was estimated at different service load levels. A more detailed discussion on the results of this study is provided in Paper 2 appended to this thesis.

4.3. Axial-torsional cyclic plasticity test

The details of the axial-torsional fatigue test program are tabulated in Table 3. All specimens have been failed due to loosing 50% of their axial load carrying capacity comparing to the first cycle. For comparison, the data for the uniaxial fatigue test specimens tested with the same axial strain levels are presented in Table 4. It is seen that for a certain axial strain amplitude, the specimens exposed to the axial-torsional straining with 90 deg out-of-phase (OP) condition had the shortest fatigue life. The specimens exposed to the in-phase (IP) condition had longer lives and the specimens tested under uniaxial loading had the longest lives. This is clearly due to the higher amount of plastic energy that is dissipated per cycle for the specimens subjected to OP straining condition comparing to that for the specimens subjected to IP or uniaxial straining.

Table 3: Details of the axial-torsional fatigue tests and the number of cycles to failure at various straining conditions

Test ID	Axial strain amplitude (ε_a)	Shear strain amplitude (γ_a)	Cycles to failure	Dissipation at half-life ($\Delta w_{HL}^{p}[MJ/m^3]$)	Note
T37S37	0.0045	0.0052	3306	2.27	$\Delta\phi = 180°$
T43S43	0.0045	0.0052	1397	2.91	$\Delta\phi = 90°$
T44S44	0.006	0.0052	1581	4.94	$\Delta\phi = 0°$
T40S40	0.006	0.0052	1278	5.80	$\Delta\phi = 90°$

Table 4: Uniaxial fatigue life of the test specimens at various strain ranges [75]

Test ID	Strain amp (ε_a)	Strain ratio (R_ε)	Cycles to failure (N_f)	Dissipation at half-life ($\Delta w_{HL}^{p}[MJ/m^3]$)
T3S3	0.0045	-1	4489	2.16
T4S2	0.006	-1	3022	4.64

The crack shape on the surface of the tubular specimens used in the axial-torsional fatigue tests are studied and presented in Figure 14. It is seen that the cracks are inclined with respect to the axial loading axis when the axial-torsional loading is IP and almost normal to the axial loading axis when the axial-torsional loading is 90 deg OP. Similar crack shapes were observed to initiate and propagate from a manufactured notch on tubular specimens fatigue tested under axial-torsional loading [76].

The evolution of axial and shear stress for the axial-torsional specimens are presented in Figure 15. The axial stress evolution from the uniaxial tests at the same strain ranges is also added to Figure 15a. A quick hardening, which is observed as a raise in the axial stress amplitude, can be seen for the specimens subjected to axial-torsional straining. A higher amount of hardening is seen when the loading is OP comparing to IP loading. This hardening occurs in the first 2% of the total life of each specimen. The material tends to soften after the quick initial hardening, and the softening trend is similar to that when the loading is uniaxial. It is worth noting the saturated axial stress amplitude, where the smallest amplitudes are for those specimens subjected to IP loading with an almost 10-25% lower saturated stress amplitude comparing to that for the uniaxial test. This value is about 2-3% for the specimens subjected to OP loading.

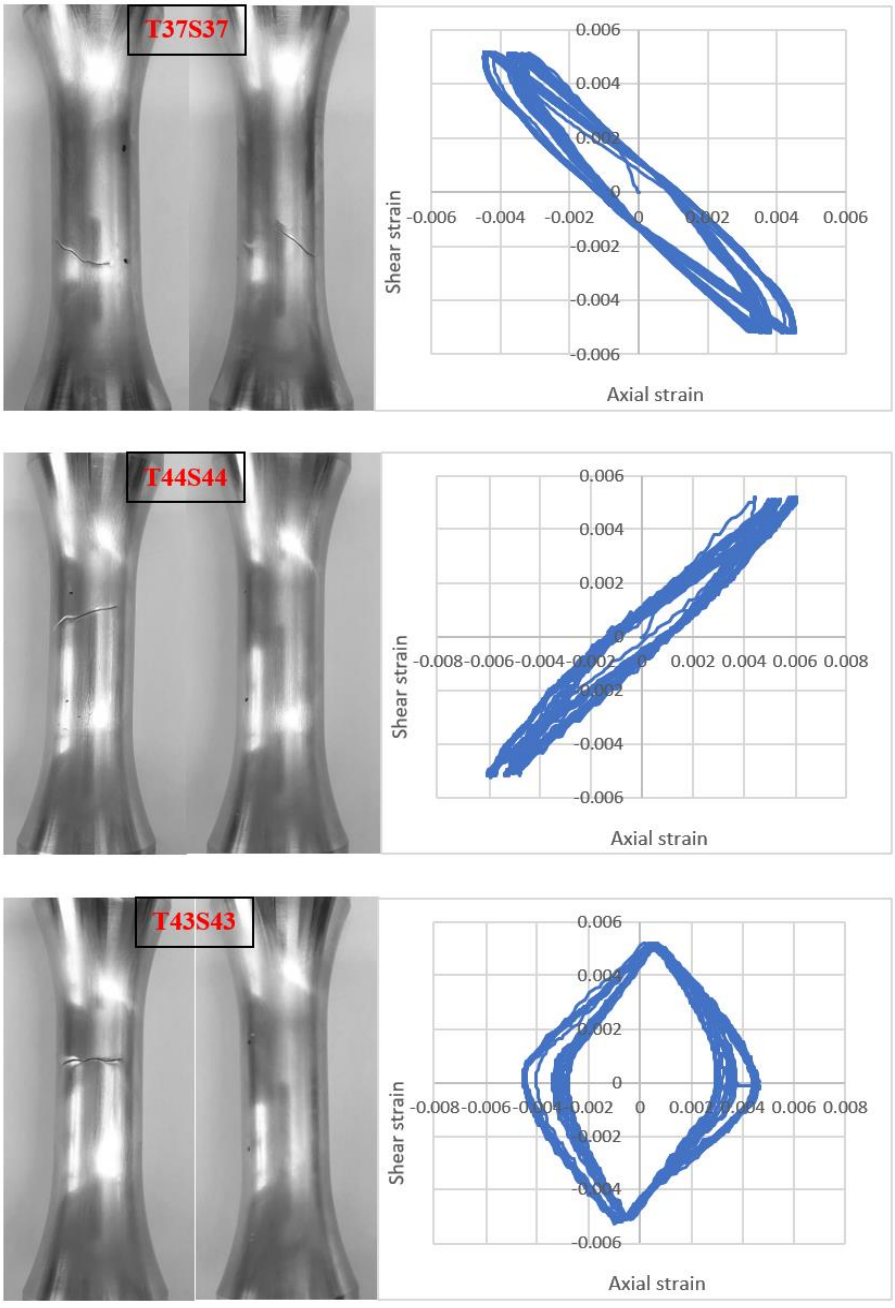

Figure 14: The front and back sides of the failed specimens used in the axial-torsional fatigue tests (left) and shear strain-axial strain curves throughout the specimens' lives (right)

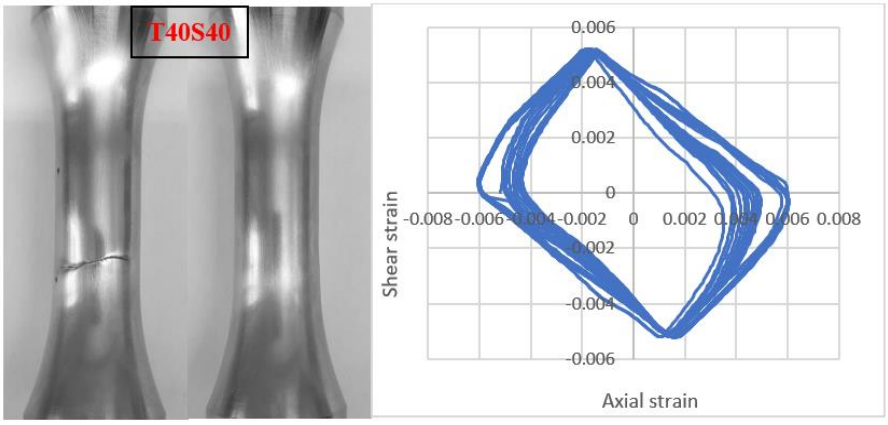

Figure 14: continued

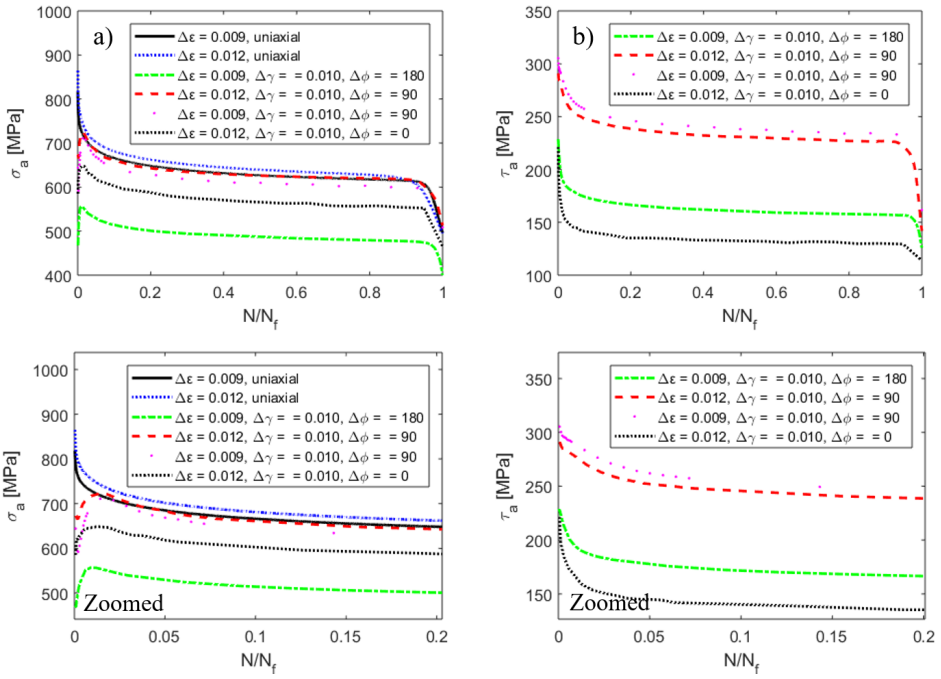

Figure 15: a) axial stress amplitude and b) shear stress amplitude vs normalized fatigue life of the axial-torsional specimens

The effect of material softening is also visible on the shear stress amplitudes where a rapid softening occurs at the first 10% of the specimens' lives, see Figure 15b. Comparing

shear stress amplitude evolution for IP loading cases, the test with the larger axial strain amplitude has a smaller saturated shear stress amplitude. This behavior is also seen for the OP loading condition, however, the difference in the saturated shear stress amp is less. Also comparing the saturated shear stresses for IP and OP loading, a great effect of OP loading is seen for similar axial and shear strain levels, e.g. see the red and black curves for the tests with $\Delta\varepsilon = 0.012$ or pink and green curves for the tests with $\Delta\varepsilon = 0.009$. This difference is more pronounced for the test with $\Delta\varepsilon = 0.012$, where the IP saturated shear stress amplitude is 43% lower than that for the OP loading.

The hysteresis loops at the specimens half-life are plotted in Figure 16a for the tests with $\Delta\varepsilon = 0.009$ and in Figure 16b for the tests with $\Delta\varepsilon = 0.012$. It is seen that while the stress amplitudes for the uniaxial and OP loading are nearly the same, the hysteresis loop area is larger for the OP loading. Also, note that the stress amplitude for IP loading is smaller than that for the uniaxial and OP loading, however, the IP hysteresis loop area is larger than that for the uniaxial and smaller than that for the OP loading. This is observed for both axial strain levels.

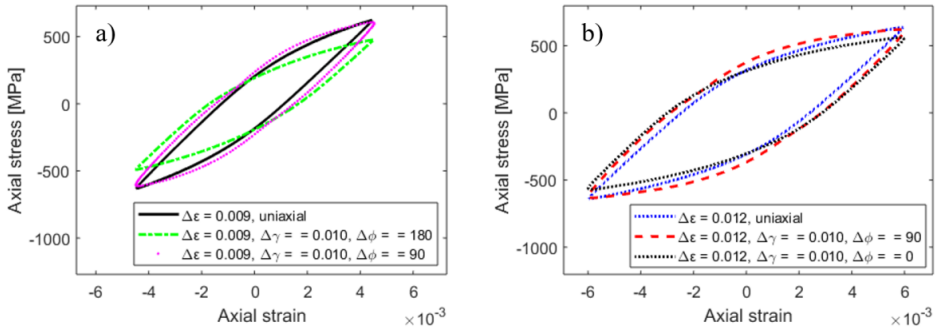

Figure 16: Comparison of the uniaxial with axial-torsional specimens' stable hysteresis loops for axial strain range of a) 0.009 and b) 0.012

The effective stress and strain amplitude have been calculated based on von Mises criterion for each axial-torsional test and plotted together with the uniaxial cyclic stress-strain curve from ref. [75]. It is seen that for the mooring chain steel grade R4 and the strain levels tested, the effective stress amplitudes in IP loading lay below the cyclic stress-strain curve while they are nearly on the curve when the load is OP. The considered chain material response to IP and OP loadings is of great importance when multiaxial fatigue crack initiation and propagation in chains is of interest. The loads at sea come from different sources that can be IP or OP depending on the loading frequencies and phase difference between the load sources.

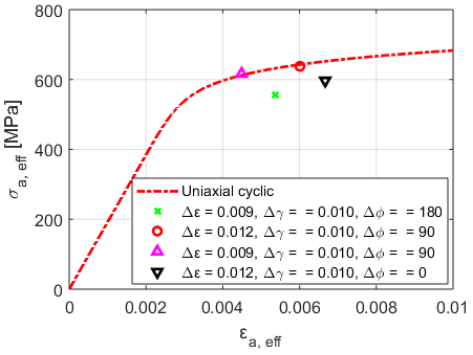

Figure 17: Cyclic stress-strain curve and effective stress-effective strain data points from the axial-torsional tests

4.4. Three-point bend test

The details of the 3PB tests, as well as the number of cycles to failure for the tested specimens, are presented in Table 5. As the tests were load controlled, monitoring the maximum deflection in the middle of the specimens could help to detect the crack initiation or to construct a relation between the crack width observed in the images captured every 100 cycles and an increase in the maximum deflection of the specimen. To evaluate this, the number of cycles needed to observe the smallest measurable increase in the maximum deflection of the specimen (i.e. 14% of the maximum deflection at the first cycle and in the order of $200\ \mu m$) are also presented in Table 5. Comparing the calculated number of cycles with the number of cycles to failure for each specimen and looking at the captured images at those cycles (see Figure 20a and b), it can be found that monitoring the maximum deflection during a fatigue test is not a precise tool for crack initiation detection. As it is seen in Figure 20a, the cracks were grown to 50~100% of the specimen's width (with the wider cracks in the preloaded specimens) when the maximum deflection was just 14% larger than that at the first cycle. The crack growth was faster after this point resulting in a 400% increase in the maximum deflection (corresponding to the defined failure point) over just a few thousand cycles.

Figure 18 illustrates the 3PB model (one-quarter of the entire volume) and the defined paths for further investigation of in-depth RS distribution and local stresses. The preloading-unloading process has been simulated in Abaqus 6.14 and the in-depth longitudinal RS distribution after removing this load is presented in Figure 19. The RS distribution follows a zig-zag pattern through the specimen's bulk with compressive RS close to the specimen's bottom surface, where a hemispherical pit was created in a later step in the simulation. It's worth noting the RS gradient (approximately $100\ MPa/mm$) that changes the direction of RS through the specimen's bulk and turns beneficial

compressive RS into harmful tensile ones. This significantly affects the fatigue crack initiation and propagation in the preloaded specimens.

Table 5: 3PB fatigue life of the test specimens at various load levels

Test ID	Load case	Cycles to failure (N_f)	Life ratio (preloaded/non-preloaded)	Cycles to 14% increase in the max deflection
T07SH	1	64916	1.44	62246
T06S4	2	93601		92541
T05SF	3	33449	1.19	27839
T04SD	4	39676		38524

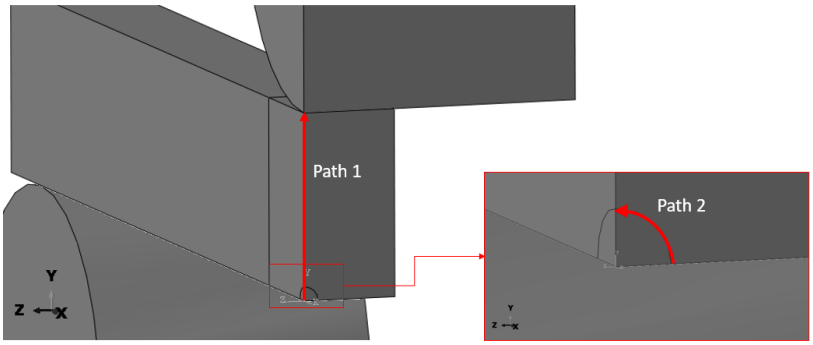

Figure 18: Defined paths through the specimen's depth and on the pit side

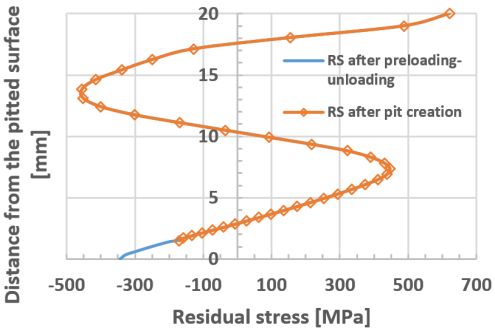

Figure 19: Distribution of the longitudinal RS ($\sigma_{x,residual}$) along path 1, shown in Figure 18, before and after pit creation

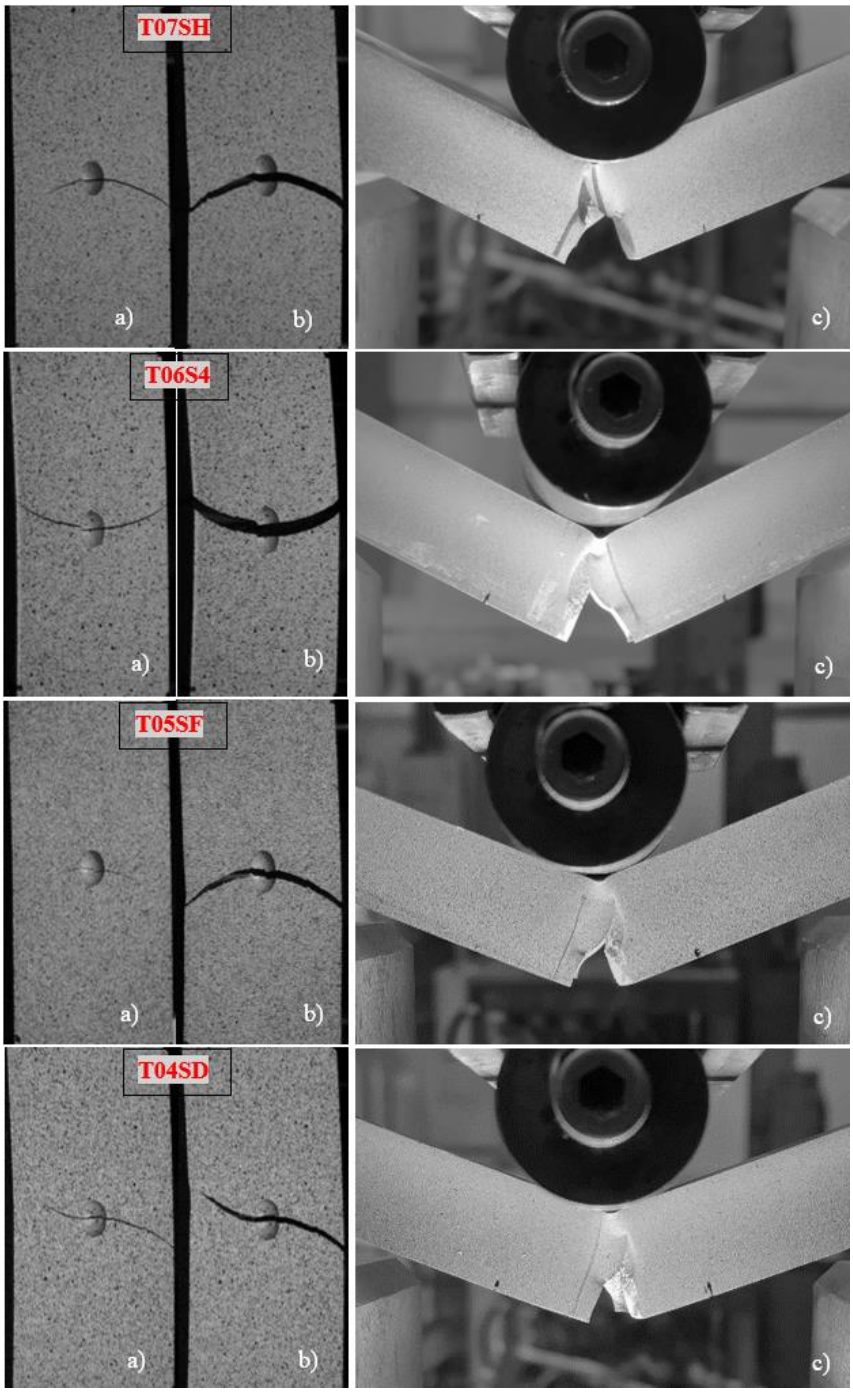

Figure 20: Pictures of the specimens when the deflection at maximum load is a) 14% and b) 400% larger than that at the 1st cycle, and c) side view of the specimens after failure

For comparison, the distribution of longitudinal stress along path 1 for a non-preloaded and a preloaded specimen subjected to loading cases 1 and 2 respectively are plotted in Figure 21. It is seen that at a short distance from the pit bottom (up to 3 mm from the pitted surface), the maximum longitudinal stress in the pre-loaded specimen is slightly lower due to the existence of compressive RS in this region. Accordingly, a longer crack initiation life is expected for the preloaded specimen. However, at a distance of 3 to 10 mm from the pitted surface, the stresses from the applied load are superimposed with the tensile RS in a preloaded specimen causing the maximum stress to be much higher than that in a non-preloaded specimen. This indicates a faster crack growth in this region in the pre-loaded specimen comparing to the non-preloaded specimen. In general, the positive effect of the compressive RS (due to pre-loading) in the pit site on the fatigue crack initiation and the specimens total life is clear, as it lowers the effective mean stress of the fatigue loading, as seen in Figure 22. This effect is more pronounced at the lower load level.

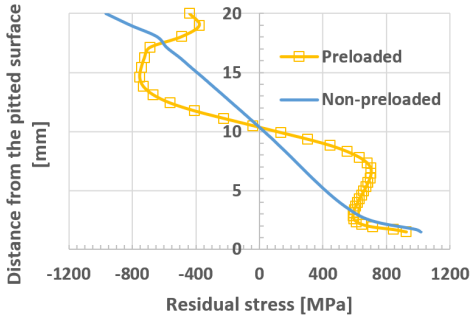

Figure 21: Distribution of maximum longitudinal stress (σ_x) for the loading cases 1 and 2 along path 1 shown in Figure 18

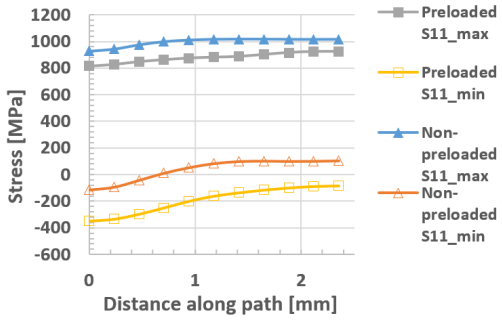

Figure 22: Minimum and maximum longitudinal stresses (σ_x) for the loading cases 1 and 2 along path 2 shown in Figure 18

5. Conclusion

The results presented and discussed in this thesis along with the appended papers contribute to the state-of-the-art by filling the gap in the multiaxial fatigue analysis of mooring chains exposed to the corrosive marine environment and tension-tension fatigue loading considering the effects of residual stresses. The developed models are robust and can account for different loading conditions, such as OPB, twist, etc. Studless mooring chains made of high strength steel grade R4 have been selected as the case study. These chains have been widely used in the offshore mooring systems; thus, the calibrated material model as well as the established numerical and experimental framework are advantageous to the chain producers, offshore production system owners, and the offshore industry standards.

An overview of the phenomena and mechanisms affecting the fatigue life of offshore mooring chains has been presented in this thesis. The emphasis has been to fatigue and corrosion as the main causes of mooring chain failures. Further, the effect of residual stresses (RS) due to proof loading has been discussed and accounted for in the performed fatigue analyses.

Small-scale uniaxial and biaxial cyclic plasticity tests have been conducted and different aspects of the material behavior under cyclic loadings have been investigated and discussed. The test specimens were cut from used mooring chains made of high strength steel grade R4. The material has shown a rapid cyclic softening behavior when subjected to uniaxial loading. However, when the load is biaxial, the material exhibits a quick hardening followed by softening. This behavior has been observed in both in-phase (IP) and out-of-phase (OP) biaxial loading conditions. From the fatigue perspective, the biaxial OP loading has been identified as the most detrimental loading condition followed

by the biaxial IP and uniaxial loading conditions. The material fatigue and cyclic plasticity parameters have been calibrated using the obtained experimental data and through developed MATLAB codes. The calibrated material model was used in the established finite element model of mooring chains subjected to proof loading and service loads, as well as the 3-point bending test specimens. The numerical simulations were mainly performed in Abaqus 6.14 commercial software. The computational fatigue crack initiation life estimation is composed of two steps:

1. Perform FEM to obtain stress-strain history at the critical point in the pit sites
2. Use the FEM outputs as the inputs to fatigue crack imitation life estimation approaches that can deal with multiaxial and variable amplitude loading as well as compressive RS.

The residual stresses, which have recently shown to be important to the fatigue crack initiation and propagation life in mooring chains, were studied both numerically using the calibrated material model in FEM and experimentally employing a non-destructive method (neutron diffraction) and a semi-destructive method (hole drilling). The experiments and simulations provide valuable insight to the multiaxial fatigue assessment of pitted mooring chains as well as the redistribution of RS over the chain service life. Longitudinal residual stresses due to proof loading have shown to be in agreement with the experimental measurement at the chain crown. These RS are of great importance as they are normal to the fatigue crack surfaces usually observed in this region. Further, the redistribution of RS due to different cyclic service loads in the pit site at the chain crown has been investigated.

Paper 1 deals with the R4 chain material characterization, fatigue and cyclic plasticity model parameters identification, as well as numerical simulation of pitted mooring chains subjected to proof loading and service loads. The fatigue crack initiation from hemispherical pits at the fatigue critical locations on a typical studless chain has been assessed using the SED fatigue approach.

Residual stresses due to proof loading have been studied both numerically and experimentally in Paper 2. Further, the material's cyclic softening behavior has been taken into account to investigate the RS redistribution over the chain service life. The fatigue crack initiation from a considered hemispherical pit at the chain crown has been assessed using a critical plane fatigue approach based on the Fatemi-Socie damage parameter combined with the Rossel-Fatemi hardness method.

Details of the experimental setup and procedure for the RS measurement in large mooring chains as well as the raw and analyzed data have been presented in Paper 3.

Future Work

In this thesis, the effect of corrosion has been considered by considering ideal hemispherical pits at the fatigue critical locations on a typical studless chain link. The

expected extension of this work is to use 3D scanners to generate point clouds that can be used to create 3D models of corroded chains for FE analysis. Using this technique, one can estimate the residual life of the scanned chain link employing the methodology explained in this thesis.

The service loads considered herein were constant amplitude tension-tension fatigue loads corresponding to storm condition and the loading applied in the full-scale fatigue tests. A continuation of this work can be to consider OPB, twist, and variable amplitude loading, using the data from several sea states to form a load history that the chain links experience at service, in the numerical simulations. A linear damage accumulation rule can be employed to sum up the damage caused by the loading at each considered sea state.

The fatigue crack initiation life estimation using either the SED or FSCP approaches need to be compared to the experimental data and a simplified case is to model the 3-point-bend test specimens and compare the predicted lives with the experimental lives. The fatigue crack initiation life estimation approaches employed in this thesis can be combined with crack propagation approaches e.g. linear elastic fracture mechanics to provide a total fatigue life estimation for notched components in general and pitted offshore mooring chains in specific at a much lower cost than full-scale fatigue tests.

References

[1] Fontaine, E., et al., *Industry Survey of Past Failures, Pre-emptive Replacements and Reported Degradations for Mooring Systems of Floating Production Units*, in *Offshore Technology Conference*. 2014, Offshore Technology Conference.

[2] DNVGL, *Offshore Standards DNVGL-OS-E301 Position mooring*. 2018.

[3] API-RP-2SK, *Design and analysis of Stationkeeping Systems for Floating Structures*, in *Third ed. American Petroleum Institute (API)*. 2005.

[4] Apos, R. Souza, and S. Majhi, *Application of Lessons Learned From Field Experience to Design, Installation and Maintenance of FPS Moorings*, in *Offshore Technology Conference*. 2013, Offshore Technology Conference.

[5] Mathisen, J. and K. Larsen, *Risk-Based Inspection Planning for Mooring Chain.* Journal of Offshore Mechanics and Arctic Engineering, 2004. **126**(3): p. 250-257.

[6] Ma, K.-t., et al., *A Historical Review on Integrity Issues of Permanent Mooring Systems*, in *Offshore Technology Conference*. 2013, Offshore Technology Conference.

[7] Kvitrud, A., *Anchor line failures Norwegian continental shelf 2010-2014*. 2014.

[8] Gordon, R.B., M.G. Brown, and E.M. Allen, *Mooring Integrity Management: A State-of-the-Art Review*, in *Offshore Technology Conference*. 2014, Offshore Technology Conference.

[9] Brown, M.G., et al., *Floating Production Mooring Integrity JIP - Key Findings*, in *Offshore Technology Conference*. 2005, Offshore Technology Conference.

[10] Brown, M., et al., *SS: Mooring System Integrity: Phase 2 Mooring Integrity JIP - Summary of Findings*, in *Offshore Technology Conference*. 2010, Offshore Technology Conference.

[11] Fontaine, E., et al., *SCORCH JIP: Examination and Testing of Severely-Corroded Mooring Chains From West Africa*, in *Offshore Technology Conference*. 2012, Offshore Technology Conference.

[12] Rosen, J., et al., *Chain FEARS JIP: Finite Element Analysis of Residual Strength of Degraded Chains*, in *Offshore Technology Conference*. 2015, Offshore Technology Conference.

[13] Rampi, L., F. Dewi, and P. Vargas, *Chain Out of Plane Bending (OPB) Joint Industry Project (JIP) Summary and Main Results*, in *Offshore Technology Conference*. 2015, Offshore Technology Conference.

[14] Ma, K.-t., et al. *Fatigue Tests on Corroded Mooring Chains Retrieved From Various Fields in Offshore West Africa and the North Sea*. in *ASME 2019 38th International Conference on Ocean, Offshore and Arctic Engineering*. 2019.

[15] Xue, X., N.-Z. Chen, and Y. Pu, *Mooring Fatigue Assessment Evaluating Chain Twist and Out-of-Plane Bending for a Semi-submersible.* Journal of Offshore Mechanics and Arctic Engineering, 2020. **142**(6).

[16] Hove, M., *Growth of Fatigue Cracks in Mooring Line Chains*, in *Structural Engineering*. 2016, Norwegian University of Science and Technology (NTNU).

[17] Fontaine, E., et al. *SCORCH JIP - Feedback on MIC and pitting corrosion from field recovered mooring chain links*. in *Proceedings of the Annual Offshore Technology Conference*. 2014.

[18] DNVGL, *Offshore standards DNVGL-OS-E301 Position mooring*. 2015, DNV GL AS.

[19] Denton, N., *Corrosion Fatigue Testing of 76mm Grade R3 & R4 Studless Mooring Chain*. 2002, Report no.

[20] Gabrielsen, Ø., K. Larsen, and S.-A. Reinholdtsen, *Fatigue Testing of Used Mooring Chain.* ASME 2017, 2017(57632): p. V001T01A072.

[21] Stiff, J.J., D.W. Smith, and N.F. Casey, *Fatigue of Mooring Chain in Air and Water - Results and Analysis*, in *Offshore Technology Conference*. 1996, Offshore Technology Conference.

[22] Pérez-Mora, R., et al., *Very high cycle fatigue of a high strength steel under sea water corrosion: A strong corrosion and mechanical damage coupling.* International Journal of Fatigue, 2015. **74**: p. 156-165.

[23] Farrow, G.H., A.E. Potts, and D.G. Washington, *Investigations Into Fatigue Performance of Offshore Mooring Chains.* ASME 2017, 2017(57632): p. V001T01A025.

[24] Bastid, P. and S.D. Smith. *Numerical Analysis of Contact Stresses Between Mooring Chain Links and Potential Consequences for Fatigue Damage*. in *ASME 2013 32nd International Conference on Ocean, Offshore and Arctic Engineering*. 2013. American Society of Mechanical Engineers.

[25] Pacheco, P.M.C.L., et al. *Analysis of the Influence of Mechanical Properties on the Residual Stress in Offshore Chain Links Using the Finite Element Method*. in *ASME 2003 22nd International Conference on Offshore Mechanics and Arctic Engineering*. 2003. American Society of Mechanical Engineers.

[26] Perez, I.M., P. Bastid, and V. Venugopal. *Prediction of Residual Stresses in Mooring Chains and its Impact on Fatigue Life*. in *ASME 2017 36th International Conference on Ocean, Offshore and Arctic Engineering*. 2017. American Society of Mechanical Engineers.

[27] Veritas, B., *Fatigue of Top Chain of Mooring Lines due to In-plane and Out-of-plane Bendings*. 2014, Bureau Veritas.

[28] Xue, X. and N.-Z. Chen, *T-N Curves and Fracture Mechanics Based Mooring Fatigue Analysis for a Semi-Submersible.* ASME 2017, 2017(57632): p. V001T01A075.

[29] Lassen, T., et al., *Crack Growth in High Strength Chain Steel Subjected to Fatigue Loading in a Corrosive Environment.* ASME 2005, 2005(41979): p. 93-101.

[30] Dowling, N.E., *Mechanical behavior of materials*. Pearson. 2012.

[31] Fernández, J., W. Storesund, and J. Navas. *Fatigue Performance of Grade R4 and R5 Mooring Chains in Seawater*. in *ASME 2014 33rd International Conference on Ocean, Offshore and Arctic Engineering*. 2014. American Society of Mechanical Engineers.

[32] Rampi, L.V., Pedro *Fatigue Testing of Out-of-plane Bending Mechanism of Chain Links*, in *ASME 2006*. 2006: Hamburg, Germany.

[33] Lassen, T., J. Aarsnes, and E. Glomnes, *Fatigue Design Methodology for Large Mooring Chains Subjected to Out-of-Plane Bending.* ASME 2014, 2014(45424): p. V04AT02A029.

[34] Vargas, P. and P. Jean, *FEA of Out-of-Plane Fatigue Mechanism of Chain Links.* ASME 2005, 2005(41979): p. 173-182.

[35] Rampi, L., et al. *Chain Out of Plane Bending (OPB) Fatigue Joint Industry Project (JIP) Static Test Program and OPB Interlink Stiffness*. in *ASME 2016 35th International Conference on Ocean, Offshore and Arctic Engineering*. 2016. American Society of Mechanical Engineers.

[36] Melis, C., P. Jean, and P. Vargas, *Out-of-Plane Bending Testing of Chain Links.* ASME 2005, 2005(41979): p. 163-172.

[37] Rampi, L., et al., *Chain Out of Plane Bending (OPB) Fatigue Joint Industry Project (JIP) Fatigue Test Program Results and Methodology.* ASME 2016, 2016(49927): p. V001T01A003.

[38] Lassen, T., E. Storvoll, and A. Bech, *Fatigue Life Prediction of Mooring Chains Subjected to Tension and Out of Plane Bending.* AsME 2009, 2009(43413): p. 229-239.

[39] Jean, P., et al., *Failure of Chains by Bending on Deepwater Mooring Systems*, in *Offshore Technology Conference*. 2005, Offshore Technology Conference.

[40] Miller, J.D., G.R. Kärrsten, and C.E. Haveman, *Best Practices for Minimizing Mooring Failures at the Fairlead.* ASME 2014, 2014(45387): p. V01BT01A028.

[41] Hellum, V., S. Ding, and T. Lassen. *Fatigue of Mooring Chains Connected to Offshore Floating Structures Considering Out of Plane Bending Effects*. in *ASME 2019 38th International Conference on Ocean, Offshore and Arctic Engineering*. 2019.

[42] Ridge, I.M.L., R.E. Hobbs, and J. Fernandez, *Predicting the Torsional Response of Large Mooring Chains*, in *Offshore Technology Conference*. 2006, Offshore Technology Conference.

[43] Ridge, I., P. Smedley, and R. Hobbs, *Effects of Twist on Chain Strength and Fatigue Performance: Small Scale Test Results.* ASME 2011, 2011(44335): p. 183-189.

[44] Martinez Perez, I. and Ø. Gabrielsen. *Computational Fatigue Assessment of Chains Working in Twisted Conditions*. in *ASME 2019 38th International Conference on Ocean, Offshore and Arctic Engineering*. 2019.

[45] Hobbs, R.E. and I.M.L. Ridge, *Torque in Mooring Chain. Part 1: Background and Theory.* The Journal of Strain Analysis for Engineering Design, 2005. **40**(7): p. 703-713.

[46] Tipton, S. and G. Shoup, *The effect of proof loading on the fatigue behavior of open link chain.* Journal of Engineering Materials and Technology, 1992. **114**(1): p. 27-33.

[47] DNVGL, *Offshore Standards DNVGL-OS-E302 Offshore mooring chain*. 2018.

[48] Shoup, G.J., S.M. Tipton, and J.R. Sorem, *The Influence of Proof Loading on the Fatigue Life of Anchor Chain*, in *Offshore Technology Conference*. 1992, Offshore Technology Conference.

[49] Abolfathi, E., et al., *The Effect of the Manufacturing Test Load on the Fatigue of Hoist Chains.* Proceedings of the Institution of Mechanical Engineers, Part B: Journal of Engineering Manufacture, 1995. **209**(2): p. 133-139.

[50] Xie, X.-f., et al., *A model to predict the relaxation of weld residual stress by cyclic load: Experimental and finite element modeling.* International Journal of Fatigue, 2017. **95**: p. 293-301.

[51] Fernández, J., et al. *Influence of the Mean Load on the Fatigue Performance of Mooring Chains*. in *Offshore Technology Conference*. 2019. Offshore Technology Conference.

[52] Gabrielsen, Ø., et al. *Mean Load Impact on Mooring Chain Fatigue Capacity: Lessons Learned From Full Scale Fatigue Testing of Used Chains*. in *ASME 2019 38th International Conference on Ocean, Offshore and Arctic Engineering*. 2019. American Society of Mechanical Engineers Digital Collection.

[53] Gao, Z., T. Moan, and S.E. Heggelund, *Time Variant Reliability of Mooring System Considering Corrosion Deterioration.* ASME 2005, 2005(41960): p. 203-210.

[54] Crapps, J., et al., *Strength Assessment of Degraded Mooring Chains*, in *Offshore Technology Conference*. 2017, Offshore Technology Conference.

[55] Lotfollahi Yaghin, A. and R.E. Melchers, *Long-term inter-link wear of model mooring chains.* Marine Structures, 2015. **44**: p. 61-84.

[56] Wang, S., et al., *Assessing Fatigue Life of Corroded Mooring Chains Through Advanced Analysis*, in *Offshore Technology Conference*. 2019, Offshore Technology Conference: Houston, Texas. p. 25.

[57] Huang, Y., S.-T. Tu, and F.-Z. Xuan, *Pit to crack transition behavior in proportional and non-proportional multiaxial corrosion fatigue of 304 stainless steel.* Engineering Fracture Mechanics, 2017. **184**: p. 259-272.

[58] Huang, Y., et al. *Numerical Investigation of Stress Concentration Factor at Irregular Corrosion Pit Under Tension-Torsion Loading*. in *ASME 2014 Pressure Vessels and Piping Conference*. 2014. American Society of Mechanical Engineers.

[59] Xu, S.-h. and Y.-d. Wang, *Estimating the effects of corrosion pits on the fatigue life of steel plate based on the 3D profile.* International Journal of Fatigue, 2015. **72**: p. 27-41.

[60] Rampi, L. and P. Vargas, *Methodology to Account for Corrosive Environment on Accelerated Fatigue Test on Mooring Chains within the Chain Out of Plane Bending (OPB) Joint Industry Project (JIP).* Fatigue Design, SBM Offshore, 2011.

[61] Fredheim, S., et al. *Corrosion Fatigue Testing of Used, Studless, Offshore Mooring Chain*. in *OMAE2013-10609. Nantes: 32nd International Conference on Ocean, Offshore and Arctic Engineering*. 2013.

[62] Arredondo, A., et al. *Stress Intensity Factors in Fitness-for-Service Assessment of Cracks in Mooring Chains*. in *ASME 2018 37th International Conference on Ocean, Offshore and Arctic Engineering*. 2018. American Society of Mechanical Engineers.

[63] Ibekwe, A., et al. *Remnant Life Assessment of Bonga FPSO and SPM Mooring Chains*. in *ASME 2018 37th International Conference on Ocean, Offshore and Arctic Engineering*. 2018. American Society of Mechanical Engineers.

[64] Van, K.D., et al. *Criterion for high-cycle fatigue failure under multiaxial loading*. in *ICBMFF2*. 1989.

[65] Perez, I.M., et al. *Multiaxial Fatigue Analysis of Mooring Chain Links Under Tension Loading: Influence of Mean Load and Simplified Assessment*. in *ASME 2018 37th International Conference on Ocean, Offshore and Arctic Engineering*. 2018. American Society of Mechanical Engineers.

[66] Ellyin, F. and K.J.J.P.V.T. Golos, *A total strain energy density theory for cumulative fatigue damage.* 1988. **110**: p. 36-41.

[67] Fatemi, A. and D.F. Socie, *A CRITICAL PLANE APPROACH TO MULTIAXIAL FATIGUE DAMAGE INCLUDING OUT-OF-PHASE LOADING.* Fatigue & Fracture of Engineering Materials & Structures, 1988. **11**(3): p. 149-165.

[68] Jie, Z., F. Berto, and L. Susmel, *Fatigue behaviour of pitted/cracked high-strength steel wires based on the SED approach.* International Journal of Fatigue, 2020. **135**: p. 105564.

[69] ASTM, *E606/E606M-12, Standard test method for strain-controlled fatigue testing.* ASTM international, West Conshohocken (PA USA): Book of Standards, 2012. **3**.

[70] ASTM, *E2207-15, Standard Practice for Strain-Controlled Axial-Torsional Fatigue Testing with Thin-Walled Tubular Specimens*. 2015.

[71] Armstrong, P.J., *A mathematical representation of the multiaxial Bauschinger effect.* CEBG Report RD/B/N, 731, 1966.

[72] Jiang, Y. and P. Kurath, *Characteristics of the Armstrong-Frederick type plasticity models.* International Journal of Plasticity, 1996. **12**(3): p. 387-415.

[73] Chaboche, J.L., *A review of some plasticity and viscoplasticity constitutive theories.* International Journal of Plasticity, 2008. **24**(10): p. 1642-1693.

[74] Zarandi, E.P. and B.H. Skallerud, *Experimental and numerical study of mooring chain residual stresses and implications for fatigue life.* International Journal of Fatigue, 2020. **135**: p. 105530.

[75] Zarandi, E.P. and B.H. Skallerud, *Cyclic behavior and strain energy-based fatigue damage analysis of mooring chains high strength steel.* Marine Structures, 2020. **70**: p. 102703.

[76] Gates, N.R. and A. Fatemi, *Multiaxial variable amplitude fatigue life analysis using the critical plane approach, Part II: Notched specimen experiments and life estimations.* International Journal of Fatigue, 2018. **106**: p. 56-69.

Appendix A: Appended papers

Paper 1: Cyclic behavior and strain energy-based fatigue damage analysis of mooring chains high strength steel

Zarandi, E.P. and B.H. Skallerud, Cyclic behavior and strain energy-based fatigue damage analysis of mooring chains high strength steel. Marine Structures, 2020. 70: p. 102703.

https://doi.org/10.1016/j.marstruc.2019.102703

Cyclic behavior and strain energy-based fatigue damage analysis of mooring chains high strength steel

Ershad P. Zarandi*[1], Bjørn H. Skallerud[1]
[1]Department of Structural Engineering
Norwegian University of Science and Technology (NTNU)
Richard Birkelands vei 1A, 7491, Trondheim, Norway
*corresponding author: ershad.p.zarandi@ntnu.no

Abstract

This study investigates the low-cycle fatigue behavior of mooring chains high-strength steel grade R4
under different strain amplitudes and strain ratios at room temperature. A fatigue test program has been carried out on small low cycle fatigue specimens cut from large mooring chains. The experimental results characterize the cyclic stress-strain relationship, the mean stress relaxation behavior, and the cyclic plasticity parameters of the material. Strain energy density is correlated with fatigue life through a simple power-law expression and very well represented by Basquin-Coffin-Mansion relationship. Further, a non-linear elastic-plastic material model is calibrated to the experimental stress-strain curves and used for the estimation of energy dissipation in the specimens under applied cyclic loads. The predicted fatigue life using the calibrated material parameters demonstrates a close agreement with the experimental fatigue life. Numerical simulations are carried out to analyze local plastic straining and assess crack initiation at the pit site of corroded mooring chains considering the multiaxial stress state. An energy-based approach is employed to estimate the number of cycles needed for a crack to initiate from an existing corrosion pit.

Keywords strain energy density; fatigue life prediction; cyclic plasticity; hardening/softening; finite element; offshore mooring chain

1 Introduction

In the last decades, energy sources at sea and under the seabed have captured engineering society's attention. As a result, the number of floating offshore production systems and facilities has increased [1]. Continuous operation of these offshore facilities, however, is directly dependent on the integrity of their mooring systems that keep these facilities in position during an operation when subjected to cyclic loads from wave, wind, and current as well as a continuous exposure to a corrosive environment. A mooring line is as strong as its weakest element, and a single line failure increases the load level on the adjacent lines and may cause failure in them ending up with operation shutdown, material loss and risking human life and environment. The high rate of failure of mooring chains used in the offshore industry necessitates improved understanding of phenomena correlated to the fatigue life of these chains, e.g. residual stresses and corrosion, to improve their design and enhance their reliability against failure [1-3]. Nucleation of fatigue cracks generally results from dynamic plastic straining. The amount of plastic straining at the corrosion pit site in mooring chains depends on the applied load as well as the material response to it. The elastic-plastic material behavior under cyclic loading conditions is more complex than that under monotonic loading. Hence, investigation of cyclic response and fatigue properties of mooring chain materials is of great importance to the prediction of the fatigue crack growth rate and the remaining fatigue life of pitted mooring chains.

Offshore industry standards (e.g. see [4, 5]) require mooring chains to be proof load (PL) tested to assure their strength capability before being installed offshore. The PL testing involves axially loading the chain up to 70% of its minimum breaking load (MBL), introducing high multiaxial residual stresses (RS) in the chain links. Finite element analysis of the heat treatment process conducted before the PL test has shown that there are RS in all three axial, hoop, and radial directions due to nonhomogeneous plastic deformation caused by different heating/cooling times of the material at the surface and in the core of chain rods [6]. However, the axial RS, which are the largest in magnitude and of high importance as they are normal to the crack faces commonly seen in chain links, are later replaced by greater RS from proof loading. The RS are an influential factor in the remaining life estimation of mooring chains at service and the finite element (FE) simulation of the PL test has revealed that the predicted RS is highly dependent on the chain material, dimensions, and PL level [7-9]. To date, the offshore industry standards lack an explicit consideration of the effects of PL level and material grade on fatigue life of different size mooring chains. An improved model combined with little knowledge of actual residual stresses is sub-optimal and does not bring the fatigue assessment methodology much further. Hence, providing quantitative information on residual stresses and their changes/relaxation in safety-critical components is of high value. This requires a proper material model that accounts for elastic-plastic material response under both monotonic and cyclic loading conditions.

Several investigations have indicated the significance of corrosion on mooring chains fatigue life [10, 11]. Some work has been carried out to assess the residual breaking strength of these severely corroded chains, see e.g. [12, 13], and consider the effect of uniform corrosion, as defined in the industry guidelines, on the chains MBL [14]. However, the fatigue strength of the pitted chains is still debatable and not studied. Small corrosion pits can act as stress raisers at the chain link surface, and as a result, reduce the chain fatigue life [15, 16]. Numerical investigations on the stress concentration factor of corrosion pits on round bars and flat plates have identified the pit aspect ratio as the main influencing parameter [15-18]. This investigation has been taken further employing experimental observation as well as elastic-plastic material models to determine strain localization and elastic-plastic stress distribution around critical pits and their transition into cracks [19-21]. Nevertheless, strain evolution at the pit site in curved round bars, e.g. mooring chain links, has not been studied to date. Cyclic plasticity and basic fatigue properties for the R4 chain material investigated in the current study are also lacking.

Large-scale fatigue tests have been conducted on both new and used mooring chains in simulated seawater in the past years and the results are presented elsewhere [4, 22, 23]. However, little attention has been paid to the characterization of the cyclic response of these chain materials. To enhance the understanding of the damage phenomena and mechanisms affecting the fatigue life of offshore mooring chains, e.g. RS and local corrosion, an appropriate material law is essential for accurate prediction of RS and its gradient that has been shown to be influential on fatigue crack growth [8, 9, 24]. This requires the development of analytical and numerical models along with experimental work. Plastic strain accumulation around pitting holes in mooring chains generally ends in fatigue crack initiation at those locations. Thus, using cyclic material data in FE models, a better prediction of stress gradient around a pit/crack after N cycles of service load is achieved compared to the case where only the monotonic material properties are employed. Moreover, cyclic plasticity tests provide input to the numerical models to quantify RS relaxation over the chains service life.

In this paper, the fatigue properties and cyclic plasticity behavior of mooring chain steel grade R4 is investigated. The tests include strain-controlled fatigue testing at different strain amplitudes and strain ratios of small specimens cut from the straight part of a studless chain link. Section 2 outlines the experimental details and relevant theoretical background. Section 3 provides a comprehensive study of the behavior of the material under various cyclic loads. In addition, plastic/total strain-life curves, as well as cumulative plastic strain energy density (SED)-life curves are constructed based

on the fully reversed fatigue test data to estimate the fatigue life of notched and unnotched components. Lastly, in Section 4, finite element simulations are carried out and plastic dissipation at the pit sites on a corroded mooring chain link is investigated. Accordingly, the number of cycles needed for a crack to initiate from an existing corrosion pit is predicted.

2 Methodology

2.1 Experimentation details

Mooring chains high strength steel grade R4 is investigated in this paper. The monotonic mechanical properties of the material are listed in Table 1. The chemical composition of the material can be found in [25]. Uniaxial strain-controlled cyclic tests were carried out on the samples machined out from the straight part (non-welded side) of an installation chain link with the diameter of $114\ mm$ and retrieved from service. The specimens were polished in a drilling machine using first a 320- and then a 600-grit sandpaper. The final polishing stage was done longitudinally using a 1000-grit sandpaper to remove circumferential machining marks and generate a smooth surface (with roughness no higher than 0.2μm). The geometry of the specimens is according to ASTM E606 [26] and illustrated in Figure 1. The ASTM E606 procedure was employed for the uniaxial strain-controlled cyclic tests. The tests were carried out in a 100 kN Dynacell servo-hydraulic test system at 0.125Hz frequency. The tests were started in compression to avoid buckling problems. The longitudinal strain was measured continuously throughout each test using a calibrated extensometer with a 10 mm gauge length attached to the specimen. The triangular waveform was used for the straining of the specimens as it provides a constant effective strain rate. The tests were run until the complete separation of the specimen into two parts. However, failure was defined based on a 50% tensile load drop, i.e. the ratio of the maximum tensile load at the cycle of failure goes below 50% of that at the first cycle. The uniaxial experimental program includes 12 specimens successfully tested under five strain ranges ranging from 0.8% to 2% and four strain ratios of $(R_\varepsilon = \varepsilon_{min}/\varepsilon_{max})$ of -1, -0.3, 0, 0.3. Data from the tests with fractures outside of the gauge section of the specimens were considered invalid and excluded from data analyses. The test program was divided into 3 parts. 1) Single-step fully reversed ($R_\varepsilon = -1$), in which several specimens were tested at different strain ranges ($\Delta\varepsilon$) to investigate the strain range effect on the material cyclic response. 2) Multi-step fully reversed ($R_\varepsilon = -1$), where the sample was loaded at the strain range of 0.008 for a block of 1024 cycles followed by a block of 16 cycles at the strain range of 0.015, to study loading sequence effect. This strain sequence was repeated until the fracture of the specimen. 3) Single-step with different strain ratios, where the tests were conducted at the constant strain range of 0.009 but different strain ratios to study the effect of strain ratio on the mean stress relaxation. All experiments were conducted in room temperature and more than 200 data points per cycle were collected for data analyses.

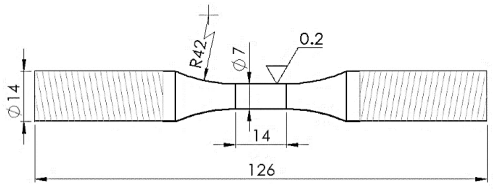

Figure 1: The geometry of uniaxial fatigue test specimens, dimensions in mm

Table 1: Mechanical material properties of the mooring chain steel grade R4

Average Vickers hardness (HV10 at **22**°C)	[HV]	303

Average toughness (Charpy-V at $-\mathbf{20}$℃)	[J]	151
Elasticity modulus ($\boldsymbol{E}$)	[GPa]	207
True yield stress ($\boldsymbol{R_{p0.2}}$)	[MPa]	843
True ultimate stress ($\boldsymbol{R_m}$)	[MPa]	1010
Total extension at maximum force ($\boldsymbol{A_{gt}}$)		0.071
Area reduction		0.68
Poisson's ratio (taken from **[27]**)		0.3

2.2 Theoretical framework

2.2.1 Stress-strain relation

The monotonic stress-strain curve can be expressed by Ramberg-Osgood relation [28] as:

$$\varepsilon = \frac{\sigma}{E} + \left(\frac{\sigma}{K}\right)^{1/n} \tag{1}$$

where σ and ε are true stress and total strain values respectively, E is the elasticity modulus, K is the strain hardening coefficient, and n is the strain hardening exponent of the material.

Similar relation as in (1) can be written for the material's cyclic stress-strain curve based on the true stress-total strain curves at the half-life of cyclic test specimens (i.e. stable hysteresis loops) tested at different strain ranges with $R_\varepsilon = -1$, in other words, a locus of tips superposed by stable hysteresis loops at different strain ranges. Thus, the cyclic stress-strain amplitude relation is written as:

$$\varepsilon_a = \frac{\sigma_a}{E'} + \left(\frac{\sigma_a}{K'}\right)^{1/n'} \tag{2}$$

where σ_a and ε_a are true stress and total strain amplitudes respectively, E' is the cyclic elasticity modulus averaged for the all studied strain ranges, K' is the cyclic strain hardening coefficient, and n' is the cyclic strain hardening exponent of the material. K, n, K' and n' are identified using the least square method and the corresponding values are listed in Table 3.

2.2.2 Strain-life relation

The test data Part 1, i.e. single-step and fully reversed tests, are analyzed on the basis of Basquin-Coffin-Manson (BCM) strain-life relationship as follows [29, 30]:

$$\varepsilon_{ta} = \varepsilon_{ea} + \varepsilon_{pa} = \frac{\sigma'_f}{E}\left(2N_f\right)^b + \varepsilon'_f\left(2N_f\right)^c \tag{3}$$

where ε_{ta}, ε_{ea}, and ε_{pa} are, respectively, the total, elastic, and plastic strain amplitudes, σ'_f and ε'_f are the fatigue strength and ductility coefficients and b and c are the fatigue strength and ductility exponents of the material. These parameters are identified using the least square method and the corresponding values are listed in Table 4.

2.2.3 Cyclic plasticity modeling

The elastic-plastic response of the material is essential for accurate numerical simulations of the components experiencing cyclic plasticity whether in the global or local domain, e.g. mooring chains with pitted surfaces. Regardless of the methodology used to estimate the remaining fatigue life of pitted mooring chains, an advanced cyclic plasticity model is required to accurately identify stresses, strains, and SED at the chains pit site. Therefore, this part is dedicated to the cyclic plasticity modeling of the material under study.

The rate-independent non-linear plasticity model considered in the current work combines kinematic and isotropic hardening. Hence, the yield function (f), which governs the onset of the plastic deformation, is expressed as:

$$f = \varphi(\boldsymbol{\sigma} - \boldsymbol{\chi}) - (\sigma_0 + R) \leq 0 \tag{4}$$

where $\boldsymbol{\sigma}$ and $\boldsymbol{\chi}$ are the stress and backstress tensors and assumed to be symmetric respectively, σ_0 refers to the yield stress at zero plastic strain, R denotes the isotropic work-hardening variable, and φ is the von Mises equivalent stress and is calculated, assuming that the material is isotropic and pressure insensitive, as follows:

$$\varphi = \sqrt{\frac{3}{2}(\boldsymbol{\sigma}' - \boldsymbol{\chi}'):(\boldsymbol{\sigma}' - \boldsymbol{\chi}')} \tag{5}$$

where $\boldsymbol{\sigma}'$and $\boldsymbol{\chi}'$ are the stress and backstress deviators respectively. Assuming small deformations, strains in an elastic-plastic model can be decomposed into elastic (reversible) and plastic (irreversible) parts using the Poisson's ratio and cyclic elastic modulus presented in Table 1 and Table 3 respectively. The isotropic work-hardening variable on the basis of Voce law reads:

$$\begin{gathered} R = Q_\infty(1 - exp(-bp)) \\ \dot{R} = h_R\dot{\lambda} \qquad , \qquad h_R = Q_\infty b\, exp(-bp) \end{gathered} \tag{6}$$

where p is the equivalent plastic strain, h_R is the hardening modulus, Q_∞ and b are the saturated value of R and the rate of saturation achievement respectively, and $\dot{\lambda}$ denotes a non-negative scalar (the plastic multiplier). The associated flow rule assumes that plastic flow is in a direction normal to the yield surface at the load point and determines the plastic strain rate ($\dot{\boldsymbol{\varepsilon}}^{\mathbf{p}}$) as:

$$\dot{\boldsymbol{\varepsilon}}^{\mathbf{p}} = \dot{\lambda}\frac{\partial f}{\partial \boldsymbol{\sigma}} \tag{7}$$

where $\dot{\lambda} = \dot{p}$ and $\dot{p}$ is the von Mises equivalent plastic strain rate given by:

$$\dot{p} = \sqrt{\frac{2}{3}\dot{\boldsymbol{\varepsilon}}^{\mathbf{p}}:\dot{\boldsymbol{\varepsilon}}^{\mathbf{p}}} \tag{8}$$

Kinematic work-hardening that has been introduced to the yield function of the material through a backstress tensor is written based on Armstrong- Frederick parameters [31] as:

$$\begin{gathered} \dot{\boldsymbol{\chi}} = c\dot{\boldsymbol{\varepsilon}}^{\mathbf{p}} - \gamma\boldsymbol{\chi}\dot{p} \\ \dot{\boldsymbol{\chi}} = \mathbf{h}^{\boldsymbol{\chi}}\dot{\lambda} \qquad , \qquad \mathbf{h}^{\boldsymbol{\chi}} = c\frac{\partial f}{\partial \boldsymbol{\sigma}} - \gamma\boldsymbol{\chi} \end{gathered} \tag{9}$$

where $\mathbf{h}^{\boldsymbol{\chi}}$ is a second order tensor, $c\ and\ \gamma$ are material parameters, and $\dot{\boldsymbol{\chi}}$ denotes the rate of backstress tensor. Using Hooke's law, the consistency condition ($\dot{\lambda} \cdot \dot{f} = 0$) determines the plastic multiplier:

$$\dot{\lambda} = \frac{\frac{\partial f}{\partial \boldsymbol{\sigma}}:\mathbf{C}:\dot{\boldsymbol{\varepsilon}}}{\frac{\partial f}{\partial \boldsymbol{\sigma}}:\mathbf{C}:\frac{\partial f}{\partial \boldsymbol{\sigma}} + \frac{\partial f}{\partial \boldsymbol{\sigma}}:\mathbf{h}^{\boldsymbol{\chi}} + h_R} \tag{10}$$

where **C** is the elastic stiffness matrix, and $\dot{\boldsymbol{\varepsilon}}$ is the total strain rate tensor. An implicit return-mapping algorithm has been used to provide a converged solution for the non-linear algebraic equations for expressing the non-linear hardening of the material.

To identify the kinematic and isotropic hardening parameters for the material under study, the procedure explained above has been scripted and run in MATLAB software. The parameters to be identified get initial values and used in the developed routine to simulate the stress-strain curves at cycles number 10, 100, and half-life to properly simulate both the transient and stabilized material cyclic response under strain range used in the test program part. The simulated curves are then compared with those from experiment at the corresponding cycles and the difference error is defined as the objective function to be minimized in an optimization algorithm. The MATLAB routine "fminsearchbnd" has been used for the optimization. Using this routine, the parameters can vary within defined ranges in the optimization process. The initial guesses, the lower, and the upper bands for the parameters used in the optimization algorithm as well as the sets of calibrated parameters providing optimized stress-strain curves at cycle 10, 100, and half-life at each strain range of the fatigue tests Part 1 are listed in Table 5.

2.2.4 Fatigue life prediction using strain energy density (SED)

The strain-life relation presented previously is generally applicable to the cases where there is no mean stress in the specimen or component. This type of loading, however, rarely exists in real applications. Unlike the strain-based or stress-based approaches, the SED approach is independent of the orientation of reference axes and, by accounting for stresses as well as strains, handles the cases with non-zero mean stress/strain in the same way it does to the cases with fully reversed stress/strain-controlled loadings. From low cycle fatigue (LCF) to high cycle fatigue (HCF) regimes, SED is able to explain complex phenomena tied with crack initiation and propagation and thus, is used here for fatigue life estimation of the specimens tested under uniaxial strain-controlled loading with various strain ranges and strain ratios and crack initiation from an existing pit on a pitted chain link.

The plastic SED at half-life (ΔW_p) can be expressed by a simple power law as a function of the number of reversals to failure ($2N_f$):

$$\Delta W_p = \alpha\left(2N_f\right)^{\beta} \tag{11}$$

where $\alpha = 2110\ MJ/m^3$ and $\beta = -0.717$ are the material parameters and for mooring chain steel grade R4 are identified by the best fit to the experimental data Part 1.

Alternatively, the total SED at half-life (ΔW_t), defined as the sum of plastic strain energy (ΔW_p) and elastic energy associated with the tensile stress ($\Delta W_{e+} = \sigma_{max}^2/2E$) to account for mean stress [32], can be contributed to the number of reversals to failure to estimate fatigue life. This approach is more suitable for HCF, where the plastic strain energy is too small to be accurately measured. Thus, the total SED is written as:

$$\Delta W_t = \alpha'\left(2N_f\right)^{\beta'} + \Delta W_0^t \tag{12}$$

where α', β' are material parameters and ΔW_0^t is the tensile elastic energy at the fatigue limit of the material. These parameters are identified by the best fit to the experimental data Part 1 as $\alpha' =$

$1289\ MJ/m^3$, $\beta' = -0.637$ and $\Delta W_0^t = 0.17\ MJ/m^3$ corresponding to a stress amplitude of $\sigma_e = \sqrt{2 \cdot E \cdot \Delta W_0^t} = 255\ MPa$.

The variation of cumulative plastic strain energy (W_f) with the number of reversals to failure can be described by a simple power law similar to Equation (11):

$$W_f = \alpha"\left(2N_f\right)^{\beta"} \tag{13}$$

where parameters $\alpha" = 1166\ MJ/m^3$ and $\beta" = 0.27$ are identified by best fit to the experimental data Part 1, 2, and 3.

3 Results

The summary of the fatigue test results is listed in Table 2 and various aspects of the material behavior under different loading conditions are discussed in this section.

Table 2: Uniaxial fatigue life of the test specimens at various strain ranges and strain ratios

ID	Strain range ($\Delta\varepsilon$)	Strain ratio (R_ε)	Cycles to failure (N_f)
Part 1			
T1S6	0.008	-1	15041
T2S5	0.008	-1	9640
T3S3	0.009	-1	4489
T22S24	0.009	-1	7119
T4S2	0.012	-1	3022
T5S15	0.015	-1	1570
T23S7	0.015	-1	1058
T17S19	0.020	-1	646
Part 2			
T21S4	0.008-0.015	-1	10401
Part 3			
T13S22	0.009	0.33	5768
T12S23	0.009	0	6438
T7S13	0.009	-0.33	4877

3.1 Cyclic softening

Figure 2a illustrates the stress amplitude variation as a function of normalized fatigue life at different strain ranges. A similar S-shape trend in the reduction of stress amplitude is seen for all strain ranges. This behavior is common among high strength metals and alloys due to obtaining lower energy dislocation arrangement. Quick reduction in the stress amplitude values (material softening) is observed in the first 10% of the specimens' lives, thereafter, the stress amplitudes tend to stabilize and remain almost constant up until approximately 90% of life. The final 10% of the specimens' lives are involved with high load carrying reduction mainly due to the growth of macroscopic cracks until final fracture. Similar behavior has been observed for high strength steel (DIN 34CrNiMo6) [33]. To quantify the cyclic softening of the material, a softening ratio (SR) is defined as:

$$SR = \frac{\sigma_{a,1} - \sigma_{a,half-life}}{\sigma_{a,1}} \quad (14)$$

where, $\sigma_{a,1}$ and $\sigma_{a,half-life}$ are the stress amplitude at the first and the half-life cycle of the specimens respectively. The softening ratio is about 22% and nearly independent from the applied strain range for the strain-controlled tests conducted in the test program Part 1, see Figure 2b.

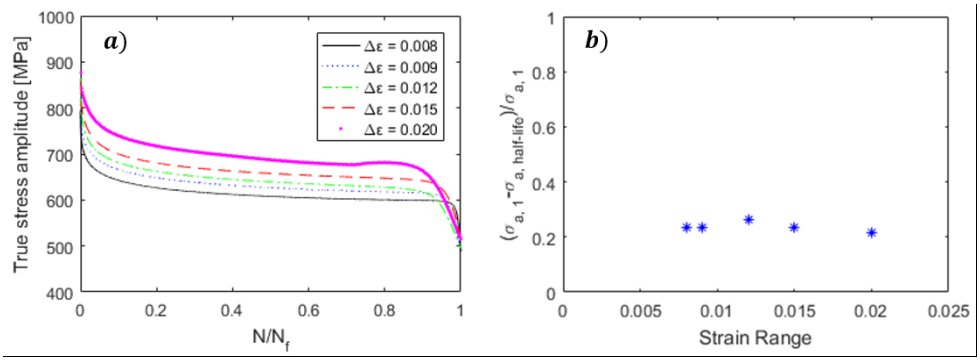

Figure 2: a) Stress amplitude vs normalized fatigue life and b) softening ratio at various strain ranges

3.2 Masing-type behavior (Strain range effect)

The stabilized hysteresis loops at the half-life of each specimen tested in Part 1 of the test program provide information on the Masing properties of the material. For a Masing-type material, the loading branches of hysteresis loops at different strain ranges coincide with the magnification of the stable cyclic stress-strain curve by a factor of two. To investigate this behavior of the material, the experimental stable cyclic stress-strain curves at different strain ranges are collected in a single graph with compressive tips coinciding at origin (0,0), as shown in Figure 3. As seen from this, the material does not follow the Masing-type behavior and the stiffness of the material reduces as strain range increases. As a result, the estimation of the hysteresis loop area using the so-called "Masing curve" overestimates the SED at any arbitrary strain range and yields conservative predictions if an energy-based fatigue model is employed. The non-Masing behavior depends on the material as well as loading and is more pronounced at higher strain ranges [34].

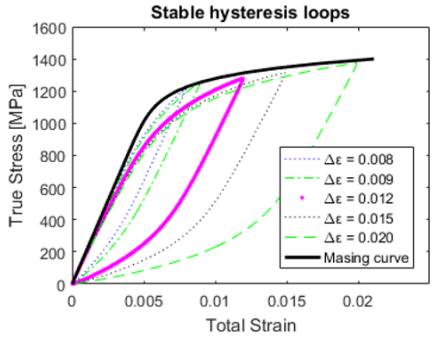

Figure 3: Stable hysteresis loops at various strain ranges plotted in a relative coordinate system at which the maximum compressive stresses coincide

3.3 Mean stress relaxation

Non-fully reversed strain-controlled loading condition results in non-zero mean stress (σ_m). As seen from Figure 4a, the normalized mean stress versus the normalized life at different strain ratios follows nearly the same trend. Almost 90% of the initial mean stress is relaxed at the half-life of the specimens, where a huge part of the relaxation occurs approximately in the first 10% of the specimens' fatigue lives. This relaxation is mainly due to the cumulative plastic straining inside the material. Thus, a smoother relaxation is expected at lower strain ranges i.e. larger effect of mean stress on fatigue life in HCF regime. For the specimens made of the material under study and cyclically loaded at the strain range of 0.009 with strain ratios varying from -0.3 to 0.3, the mean stress relaxation trend follows an S-shape curve that is little influenced by the strain ratio, see Figure 4a. However, the amount of relaxation is a linear function of the strain ratio, as shown in Figure 4b.

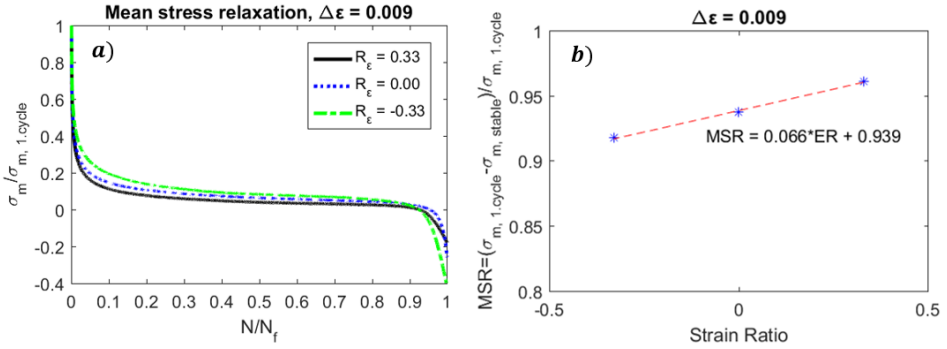

Figure 4: a) normalized mean stress vs normalized life and b) mean stress ratio (MSR) as a function of strain ratio (ER)

3.4 Loading sequence effect

The load history effect is evaluated here by analyzing the data from the multi-step uniaxial strain-controlled fatigue test, in which the specimen experiences a strain block of 1024 cycles at the strain range of 0.8% followed by a strain block of 16 cycles at strain range of 1.5%. This sequence is repeated until the specimen fractures. Figure 5a presents the variation of maximum, minimum and mean stresses values versus the number of cycles for both the multi-step and single-step tests. It is seen that the material experiences more overall softening, i.e. a 5% lower stabilized stress amplitude, in the multi-step test comparing to that in the single-step strain-controlled test at the strain range of 0.8%. The effect of overloading on the material softening decreases after the first few straining sequences and the stress amplitudes reaches to a stabilized value, see Figure 5b.

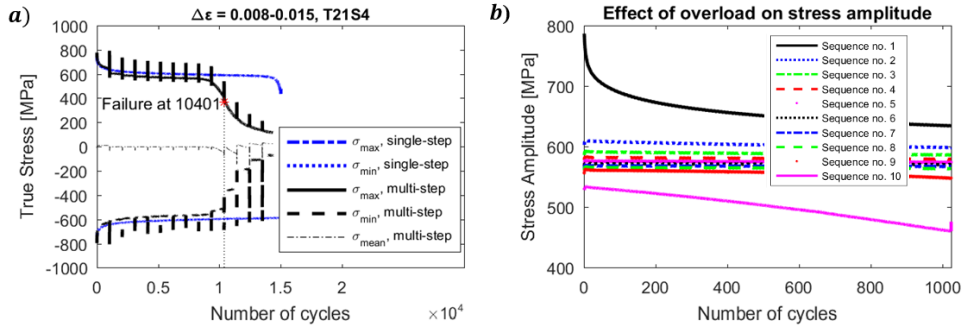

Figure 5: a) multi-step test with lower strain range of 0.008 and higher strain range of 0.015 and b) the effect of overloading on stress amplitudes at each loading sequence (blocks of 1024 cycles)

3.5 Stress-strain relation

The monotonic and cyclic stress-strain curves in Ramberg-Osgood form, Equations (1) and (2), are illustrated in Figure 6 and the identified parameters are listed in Table 3. It is seen that the cyclic stress-strain curve lays below the monotonic curve as a result of the material's cyclic softening. Hence, the use of a material model based on the monotonic response of the material in applications where components are expected to experience cyclic loading conditions, e.g. mooring chains, significantly underestimates the amount of plastic straining in the material and leads to inaccurate estimation of fatigue life. The cyclic elasticity modulus was calculated as the average value of the slope of the linear portion of the stable hysteresis loops upon strain reversal from the maximum load at different strain ranges. As this way of finding E differs from how the monotonic E is determined, a small difference is obtained.

Table 3: Identified parameters for Ramberg-Osgood relation for mooring chain steel grade R4

Strain hardening exponent ($\boldsymbol{n}$)		0.0463
Strain hardening coefficient ($\boldsymbol{K}$)	[MPa]	1124
Cyclic strain hardening exponent ($\boldsymbol{n'}$)		0.0688
Cyclic strain hardening coefficient ($\boldsymbol{K'}$)	[MPa]	966
Cyclic elasticity modulus ($\boldsymbol{E'}$)	[GPa]	193
Cyclic true yield stress ($\boldsymbol{R'_{p0.2}}$)	[MPa]	630

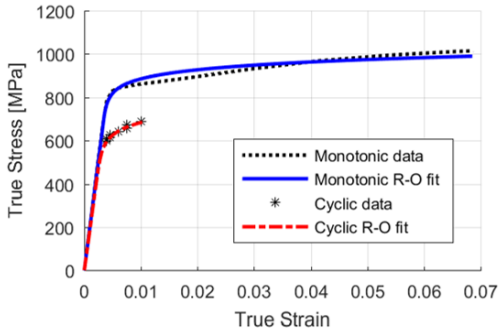

Figure 6: Monotonic and cyclic stress strain curves for the chain material steel grade R4

3.6 Strain-life relation

Plastic, elastic, and total strain amplitudes as a function the number of reversals curves, Equation (3), as well as the data points from the experimental data Part 1 are illustrated in Figure 7. The transition life (N_T), at which elastic and plastic strain amplitudes are identical, is characterized as 2139 cycles. The strain-life curve of un-notched specimens can be used for the LCF as well as HCF analysis of notched components since fatigue damage is assessed directly in terms of local strains.

Table 4: Coffin-Manson fatigue parameters, used in Equation (3), identified for the mooring chain steel grade R4

Fatigue strength exponent ($\boldsymbol{b}$)		-0.0449
Fatigue strength coefficient ($\boldsymbol{\sigma'_f}$)	[MPa]	946
Fatigue ductility exponent ($\boldsymbol{c}$)		-0.6508
Fatigue ductility coefficient ($\boldsymbol{\varepsilon'_f}$)		0.725

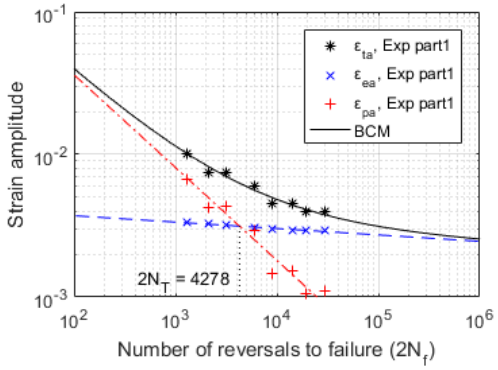

Figure 7: Total strain (solid), plastic strain (dashdotted), and elastic strain (dashed) amplitudes vs number of reversals to failure for mooring chain steel grade R4

3.7 Cyclic plasticity modeling

Figure 8 presents the comparison of numerical and experimental stress-strain curves at different strain ranges at cycles number 10, 100, and at half-life following the procedure presented in Section 2.2.3. For clarity, the hysteresis loops are partly presented. A decent agreement between the experimental and numerical stress-strain curves is observed. The stress amplitudes obtained from numerical simulations are similar to those from experimentations with a maximum difference of less than 5%. Further, a good approximation of energy dissipation during cyclic loading is achieved, which is valued for the prediction of the remaining fatigue life of notched components, e.g. pitted mooring chains, using an energy-based fatigue approach.

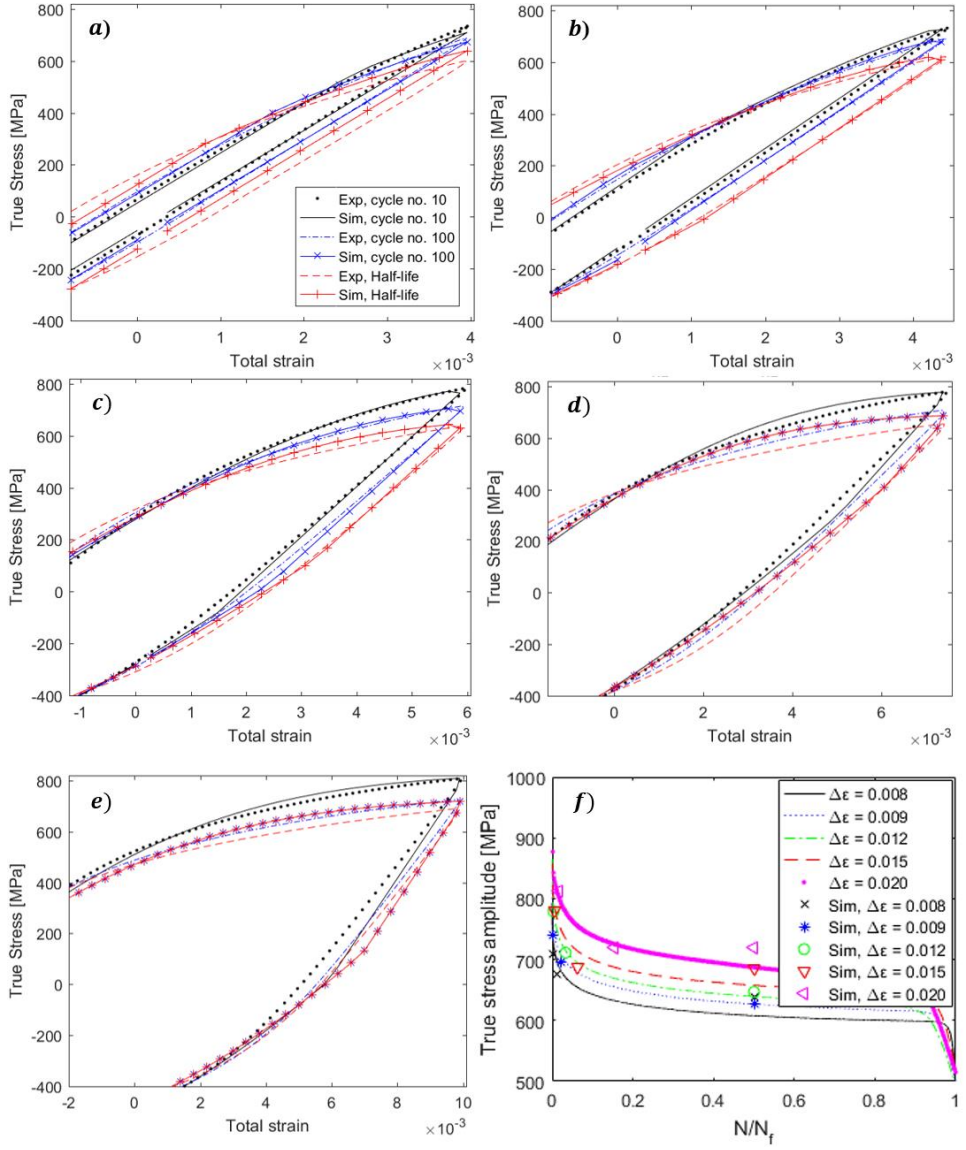

Figure 8: Visualization of the material cyclic response at cycle no. 10, 100, and half-life (saturated) at the strain ranges of a) 0.008, b) 0.009, c) 0.012, d) 0.015, e) 0.020, f) stress amplitudes; numerical simulation using the optimized hardening parameters vs experimental

The comparison of the identified parameters for different strain ranges in Table 5 shows that the material cyclic hardening/softening cannot be described by a single set of hardening parameters due to the non-Masing type behavior of the material. Thus, to get the most accurate results from numerical simulation, one should use the set of variables for the strain range closest to that in the real application.

Table 5: Parameters for non-linear combined kinematic with isotropic hardening model identified for the mooring chain steel grade R4

	σ_0 $[MPa]$	Q_∞ $[MPa]$	b	c $[MPa]$	γ
Inputs to the optimization routine					
Initial value	500	-200	2	400000	600
Lower band	300	-230	0.5	100000	300
Upper band	700	-170	10	1000000	1600
Calibrated values					
Strain range					
0.008	645	-171	7.6	398702	1234
0.009	546	-227	3.1	536565	1500
0.012	446	-185	1.4	362145	872
0.015	306	-170	5.5	449291	800
0.020	494	-196	4.3	179161	406

3.8 Fatigue life prediction

Equations (11) and (12) can be used for fatigue life estimation of specimens made of mooring chain steel grade R4 and the predictions are examined for several different strain ranges and strain ratios. Figure 10a illustrates the SED-life curve for the material under study. SED could be obtained by averaging SED over the number of cycles to failure or closely approximated by the SED at the half-life cycle of each specimen.

The fatigue lives of the specimens tested in the fatigue test program Part 1 and Part 3 are estimated using the plastic and total SED at half-life (HL) obtained from numerical simulations in Equations (11) and (12) and are denoted by $N_{f,p}$ and $N_{f,t}$ respectively. The estimated lives are compared with the experimental lives and listed in Table 6. Figure 9 illustrates how successfully the SED approach can correlate the predicted and experimental lives of the specimens over the entire range of applied strain ranges and ratios. In practice, fatigue life can be estimated using both plastic and total SED with decent accuracy, and in this investigation, the predicted lives are within a factor of 1.7 of the experimental lives.

Table 6: Experimental and predicted fatigue life using strain energy density approach

ID	**Strain range ($\Delta\varepsilon$)**	**Strain ratio (R_ε)**	$N_{f,exp}$ **[cycles]**	$\Delta W_{p,HL}$ $[MJ/m^3]$	$\Delta W_{t,HL}$ $[MJ/m^3]$	$\Delta W_{p,sat}$ $[MJ/m^3]$	$N_{f,p}$ **[cycles]**	$\Delta W_{t,sat}$ $[MJ/m^3]$	$N_{f,t}$ **[cycles]**
			Experimental			**Predicted (Numerical simulation)**			
Part 1									
T1S6	0.008	-1	15041	1.33	2.23	1.30	15088	2.38	11123
T2S5	0.008	-1	9640	1.56	2.45	1.30	15088	2.38	11123
T3S3	0.009	-1	4489	2.19	3.16	2.16	7392	3.20	6755
T22S24	0.009	-1	7119	2.29	3.26	2.16	7392	3.20	6755
T4S2	0.012	-1	3022	4.67	5.72	4.64	2546	5.73	2598
T5S15	0.015	-1	1570	7.30	8.49	7.29	1355	8.52	1373
T23S7	0.015	-1	1058	8.27	9.42	7.29	1355	8.52	1373
T17S19	0.020	-1	646	12.38	13.76	13.06	601	14.41	593
Part 3									
T13S22	0.009	0.33	5768	2.79	3.68	2.14	7493	3.18	6814
T12S23	0.009	0	6438	2.50	3.41	2.15	7445	3.19	6779
T7S13	0.009	-0.33	4877	2.05	3.09	2.20	7210	3.23	6640

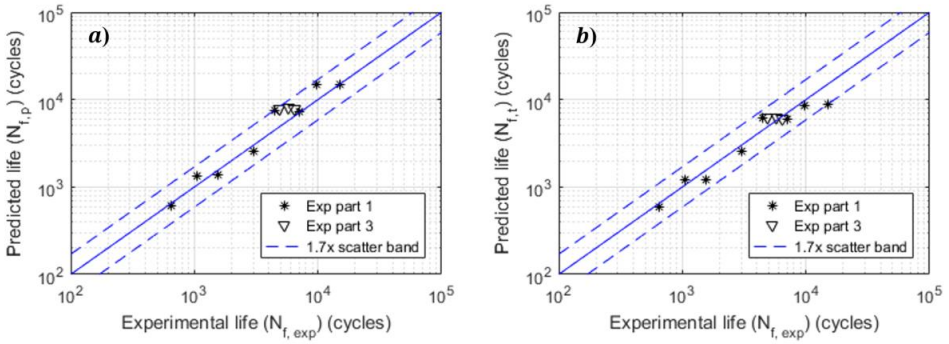

Figure 9: Experimental vs predicted fatigue life based on SED approach using a) ΔW_p and b) ΔW_t obtained from numerical simulations

As seen in Figure 10b, a higher amount of plastic strain energy is accumulated prior to failure at lower strain ranges and vice versa. In other words, fatigue toughness of the material increases as the applied dynamic load decreases. Knowing the stable plastic SED, i.e. the energy dissipation at half-life (ΔW_p), for a specimen made of the material under study, one can get a rough estimation of the number of reversals to failure using Equation (13) by substituting W_f with $\Delta W_p * N_f$. It is worth noting that the results from test Parts 2 and 3 are also added to the graph presented in Figure 10b, showing that the SED approach can properly account for variable amplitude loading as well as mean load effect. For instance, the number of loading blocks to failure (N_b) for the specimen in fatigue test Part 2 can be estimated using the stable plastic SED and cumulative plastic SED at the strain range of 0.008 and 0.015 and Palmgren-Miner rule:

$$N_b * \left[1024 * \left(\frac{\Delta W_{p\ at\ \Delta\varepsilon=0.008}}{W_{p\ at\ \Delta\varepsilon=0.008}}\right) + 16 * \left(\frac{\Delta W_{p\ at\ \Delta\varepsilon=0.015}}{W_{p\ at\ \Delta\varepsilon=0.015}}\right)\right] = 1$$

$$N_b = 10.02\ blocks$$

and knowing that each block had 1040 cycles the number of cycles to failure can be estimated as $N_f = N_b * 1040 = 10421$ cycles that is comparable with the experimental life which is 10401 cycles.

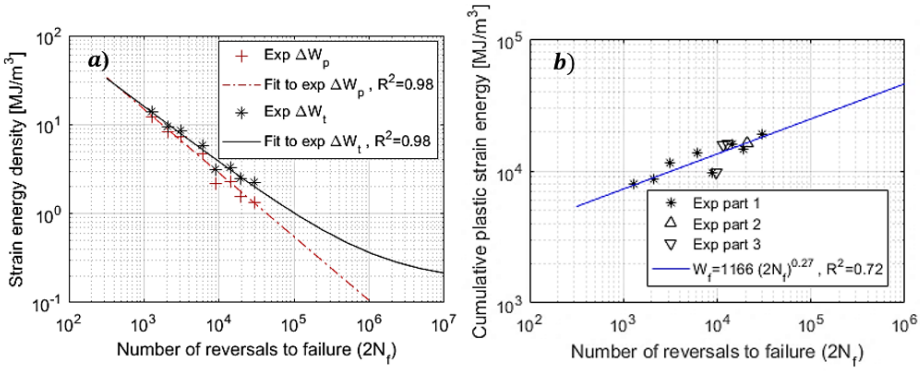

Figure 10: a) plastic strain energy density (dashdotted) and total strain energy density (solid) and b) cumulative plastic strain energy (W_f) vs number of reversals to failure ($2N_f$)

4 Case study; finite element simulation of pitted mooring chains

Fatigue cracks initiation is generally due to cyclic plastic straining. Hysteresis loop area versus life curve has been shown to be effective in the fatigue life estimation of un-notched specimens at various loading conditions. The remaining life of corroded mooring chains that experience local plastic straining around the pitting holes at the surface can be estimated in the same manner. Thus, a cyclic elastic-plastic material model is essential for accurate simulation of plastic straining at the mooring chain pit site. Such a model is herein proposed based on the obtained material hardening parameters following the procedure presented in 2.2.3. The parameters at the strain range of 0.009 are chosen to be representative for all strain ranges. The implementation of a material model based on these parameters provides a decent prediction of the material cyclic behavior at loads levels near the material yield point and acceptable predictions at higher loads. The model combining kinematic with isotropic hardening based on Armstrong-Frederick and Voce parameters is implemented in Abaqus software and utilized in plastic deformation analysis at the pit sites on chain links.

A model consisting of one complete chain link with the diameter (D) of $114mm$ and two half links are constructed. To reduce the computational efforts, only 1/8 portion of the model with three symmetry planes (XY, YZ, XZ) are used in the analysis, see Figure 11. Hard contact with the penalty method with a stiffness scale factor of 0.01 is applied to the chains contact regions to lower over-constraint issues and reduce the number of iterations required in the analysis [35]. A friction coefficient of 0.3 is used for the tangential behavior of the interaction [36].

First order hexahedral elements with reduced integration schemes (C3D8R) are used, and mesh convergence has been carried out with a finer mesh at the pit site in order to capture plastic strain localization optimally. Figure 13 illustrates the maximum principal strain contours at the pit site at the chain crown for three different mesh sizes, and maximum principal strains along path A are compared and presented in Figure 13d. It is seen that the strain is more localized at the pit wall rather than the pit bottom for the considered hemispherical pit at the chain crown. Table 8 compares von Mises stress and maximum principal strain at the critical point located at the pit wall. Considering the mesh study results presented in Table 8 and Figure 13, the model with average mesh size is able to efficiently determine stress and strain values as well as the location of the critical point at the pit site (i.e. on the pit wall) with acceptable accuracy and thus, used in the rest of the simulations.

To assess the effectiveness of the application of SED approach for the case of pitted mooring chains, a simplified case (mooring chains with smooth surfaces pitting holes) is considered herein and the effect of surface roughness inside corrosion pits is thus neglected as to date there is no data to characterize the average roughness at a typical mooring chain link corrosion pit surfaces. Three hemispherical pits with 4mm depth ($a = 4mm$) and aspect ratio (AR) of 0.5 are introduced to the model after proof load removal. This is done, using the model change interaction in Abaqus/Standard, by deactivating elements in the pits to simulate material removal. The choices of the locations, depth, and aspect ratio of the pits are made based on the information obtained from the investigation of the recovered mooring chain links after several years of service life [23, 37-39]. The modeled pits are located at the crown, the connection of the straight with the bent part (known as the K_t point), and the straight part of the middle chain link. This is to investigate crack initiation from corrosion pits at the critical fatigue failure locations on a typical studless mooring chain. In this relation, two paths are defined at the pit site; one at the pit wall and the other at the pit front of all the three pits, see Figure 11c.

The loading and boundary conditions are shown in Figure 11. The load is applied at a reference point (RP), which has restricted degrees of freedom in all directions except along the loading axis i.e. X-axis. The degrees of freedom of the half-chain cross-sections (loaded faces) at the straight parts are

kinematically coupled to those of the RP except along the Y-axis. The nominal load (the force applied on the cross-section area at the chain link straight parts) history is detailed in Figure 12 and Table 7 consisting of proof loading (PL), i.e. loading up to 70% of minimum breaking load ($MBL = 12420KN$) and unloading as defined in the standards [5], followed by a service load, which includes a mean load (ML) and a cyclic load (CL) caused by wind, wave, and seawater current. In this study, different service load levels based on what mooring chains experience during their service lives are used to investigate the effects of mean tension and the load amplitude on plastic straining at the pit site. Note that the cyclic load levels correspond to extreme storm situations and also correspond to the load levels employed in large-scale testing in order to have manageable test durations.

Table 7: Details of the applied nominal loads in FEM

Loading	***PL*** [%MBL]	***ML*** [%MBL]	***CL*** [%MBL]
Case 1	**70**	16	8
Case 2	**70**	16	10
Case 3	**70**	20	8
Case 4	**70**	20	10

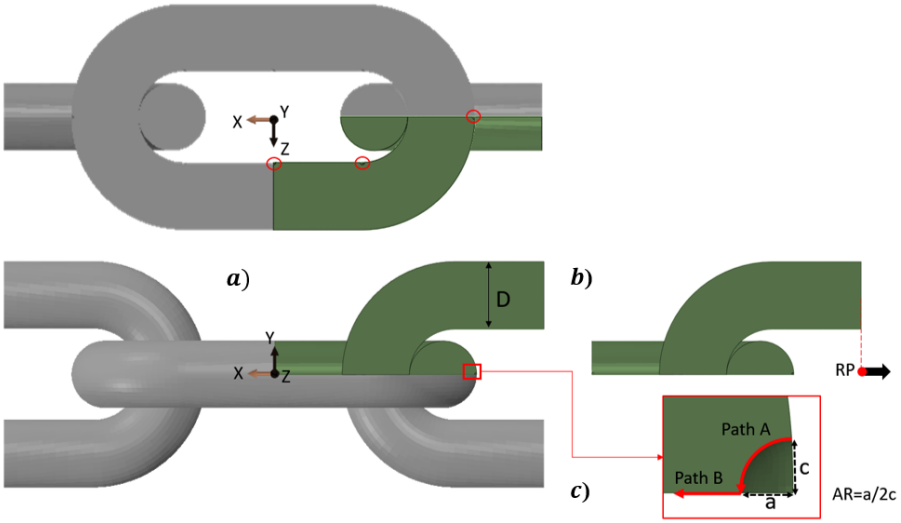

Figure 11: a) finite element model of chain links with pits at three locations (red circles) on the considered 1/8 of the entire volume (shaded) b) loading point interacted with the loaded face, and c) pits geometry and the defined paths

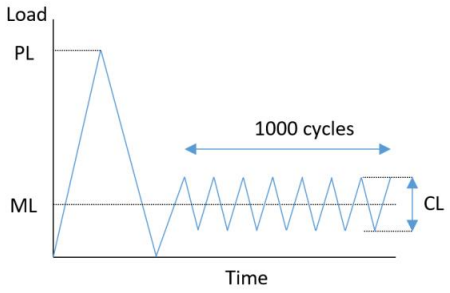

Figure 12: Loading history applied in FEM for all considered loading cases

Table 8: Comparison of von Mises stress and maximum principal strain at the critical point on the pit wall at the maximum load of loading case 1 for different mesh densities

	Coarse mesh	**Average mesh**	**Fine mesh**
No. of elements in the model	35419	38699	66713
Maximum von Mises stress [MPa]	862	882	890
Relative error in stress value wrt the fine mesh [%]	-3.1	-0.9	0
Location of maximum principal strain along the path A [mm]	0.00	0.56	0.53
Maximum principal strain	0.0059	0.0065	0.0069
Relative error in strain value wrt the fine mesh [%]	-14.9	-6.2	0

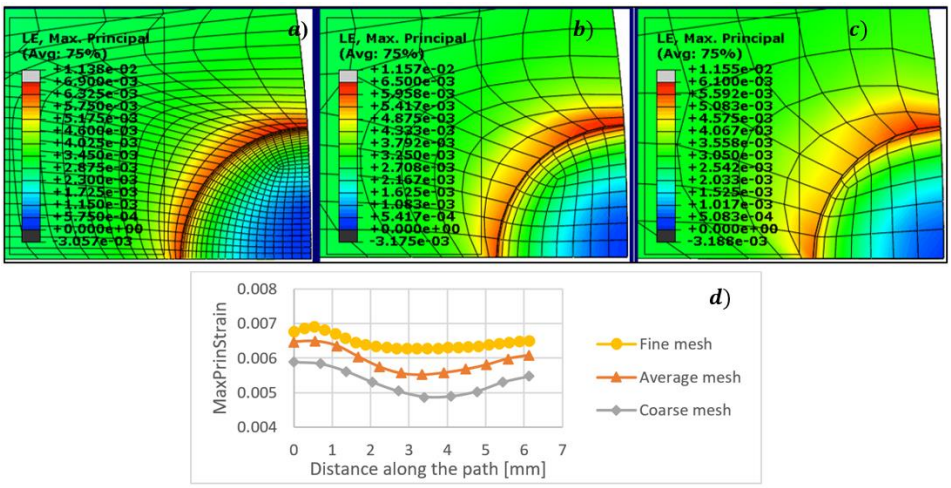

Figure 13: Local mesh at the pit site at the crown with stress contours of a) fine, b) average, c) coarse mesh, and d) comparison of maximum principal strain along path A at the maximum load of loading case 1

Investigation of von Mises equivalent plastic strain (herein denoted by PEEQ) at the pit sites is beneficial in the identification of the location of crack initiation from the considered pits. Figure 14 illustrates PEEQ variation at the wall (path A) and the front (path B) of the pits located at three

different locations on the modeled chain link after being loaded for 1000 cycles of a service load (ML=16%, CL=8% of MBL). Similar trends have been observed at the other service loading cases studied here. It is seen that the highest amount of plastic strain accumulation, almost 3 and 6 times higher than that for the pit at the K_t point and the pit at the straight part of the link respectively, is around the pit located at the chain crown highlighting the fact that this site is the most critical location for fatigue cracks on a pitted mooring chain link. Many fatigue failures have been observed at the outer radius of corroded chain crowns in large-scale fatigue tests and reported elsewhere [23, 38, 40]. In view of this, assuming the single dominant flaw approach, we will concentrate on the pit located at the chain crown for the rest of this paper.

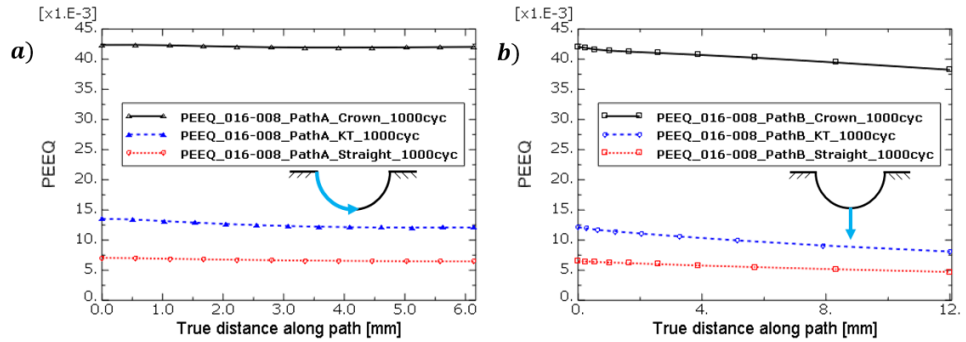

Figure 14: Comparison of the equivalent plastic strain (PEEQ) along a) path A and b) path B for the three pits located at different locations on a chain link after being loaded for 1000 cycles

A closer look at the pit located at the chain crown provides an indication of where the crack will initiate from a hemispherical pit. The comparison of PEEQ at the pit wall before and after 1000 cycles of service load shows that the plastic strain accumulation rate is maximum at a location slightly below the pit mouth, where PEEQ has also its maximum value, as shown in Figure 15c. This trend has been observed for other pit aspect ratios as well [21]. Accordingly, it is expected that cracks initiate from this location and grow until they enclose the hemispherical pit and further grow until the final fracture. Looking at the variation of PEEQ at the pit front in Figure 15b, it is observed that a larger amount of material at the pit front experiences dynamic plastic straining as the material cycles. This results in

an enlarged cyclic plastic zone and thus, higher mean stress relaxation within that zone influencing the crack growth rate at the chain crown.

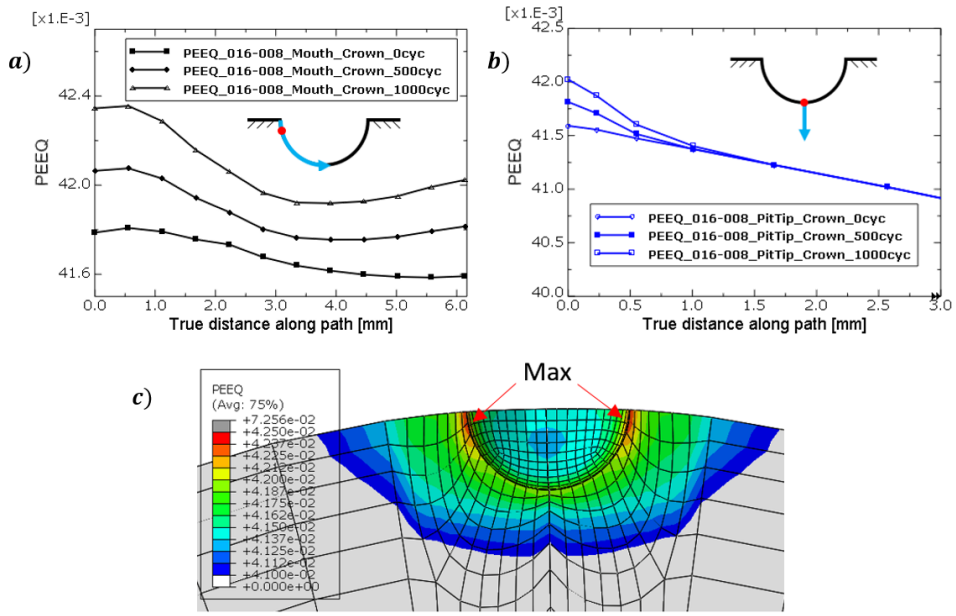

Figure 15: Plastic strain accumulation along a) path A, b) path B for the pit located at the crown of a chain link before, during, and after 1000 cycles of service load (ML=16%, CL=8% of MBL), and c) PEEQ contour plot of the pit after 1000 cycles

FE simulations have been carried out to investigate energy dissipation at the pit site located at the chain crown under different loading cases. The accumulated energy dissipated per unit volume in the critical element by plastic deformation (W_p) for the first 1000 cycle simulations at each loading condition is extracted and later extrapolated to one million cycles using polynomial fitting curves. These curves are then plotted together with the fitted curve to the W_p from the uniaxial small-scale tests and illustrated in Figure 16. Since the plastic zone at the pit site is fairly constrained by the elastic material around it, the loading condition at the pit site can be assumed to be strain-controlled. Therefore, it can be assumed that the same amount of damage is accumulated at the gauge section the fatigue specimens and at the critical location at the pit site. Thus, both will have the same life to failure (corresponding to an initiated crack size of 3.5 mm i.e. the half diameter of the small-scale specimens) if W_p at the critical point in the pit site is equal that for the fatigue specimens. Although, this is a finite crack, it is small compared to the dimensions of the chain link. Accordingly, the intersections of the curves in Figure 16 give the estimated number of cycles to crack initiation for the pitted chain link studied here.

To find out what order polynomial provides the most precise extrapolation, the simulation of the chain links at loading case 1 was continued to 10000 cycles and the resulted W_p is plotted, see Figure 17, against that obtained from the simulation of the first 1000 cycles, which is extrapolated to 10000 cycles. It is seen that using a third-order polynomial fitting curve one can find out the trend of the cumulative dissipated energy for a higher number of cycles well. Hence, the simulations at the other

loading cases were only continued to 1000 cycles to maintain the computational efforts cost-effective. The identified parameters for the fitting curves for each loading case are listed in Table 9.

The predicted lives using this energy-based approach as well as experimental fatigue lives of the corroded chain links ($D = 114mm$, grade R4) tested in simulated seawater in the lab (3.5% sodium chloride) and predictions using S-N curves presented in DNVGL-OS-E301 [22] are listed in Table 9. In the large-scale tests, the failure was defined as a through thickness crack. The presented model provides predictions of crack initiation life from a pit at the surface of corroded chain links at different loading cases studied here. The estimated crack initiation life is about 20 to 40% of the experimental total life depending on the applied load. It is worth noting that unlike the DNVGL S-N curve, the model can account for the effect of the mean load as well as the load amplitude on the fatigue life of corroded mooring chains. It is seen from the predicted lives in Table 9 that the mean load has a larger effect than the load amplitude on the fatigue crack initiation life of pitted chains subjected to the loading cases studied here. For example, comparing loading case 1 with 3, a 25% increase in the mean load at the load amplitude of 8% MBL resulted in a 57% decrease in the predicted crack initiation life while comparing loading case 1 with 2, a 25% increase in the load amplitude made the initiation life only 37% shorter. The reduction in the initiation life at a higher load amplitude (10% MBL) for the same amount of increase in the mean load is less pronounced, almost 30%, but still highly noticeable.

A recent numerical study on the fatigue crack growth in mooring chains considering the residual stresses due to proof loading has been carried out in [41]. One can employ their methodology to estimate the number of cycles needed for a crack with a certain initial size to grow and cause failure in a chain link. The cycles are later added to the number of cycles predicted by the present approach for crack initiation from a pit to provide an estimation for the total life of a corroded chain link.

Table 9: Details of different loading cases and experimental and predicted fatigue life

Nominal $\boldsymbol{ML}$ $\%\boldsymbol{MBL}$	**Nominal** $\boldsymbol{CL}$ $\%MBL$	$\boldsymbol{N_f}$ $experimental$ [cycle]	$\boldsymbol{N_f}$ $DNVGL$ [cycle]	$\boldsymbol{N_{initiation}}$ $predicted$ [cycle]	**3rd order polynomial** $ANi^3 + BNi^2 + CNi + D$				
					A(e-11)	B(e-9)	C(e-5)	D	R^2
16	8	501872*	520436	113418	2	8	20	36.9	0.998
16	10	318174*	266430	70936	7	200	40	36.9	1
20	8	-	520436	49250	20	-70	2	36.9	0.993
20	10	126614**	266430	48938	20	100	10	36.8	0.999

*Reported by Fredheim et al. in [40]

** Unpublished report

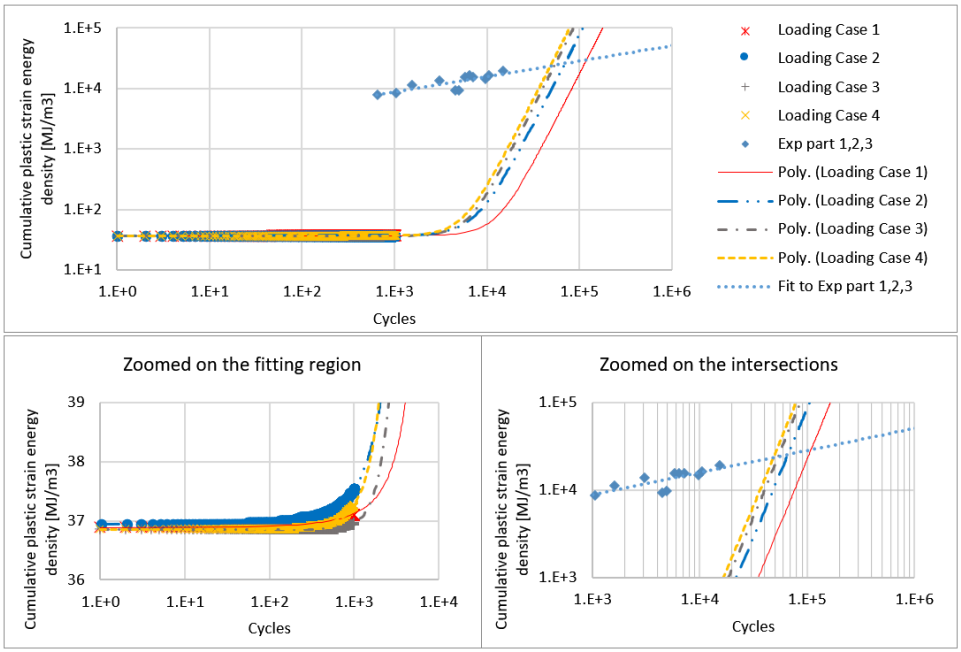

Figure 16: Polynomial fit to the maximum plastic energy dissipation at slightly below the pit mouth vs number of cycles at different loading cases

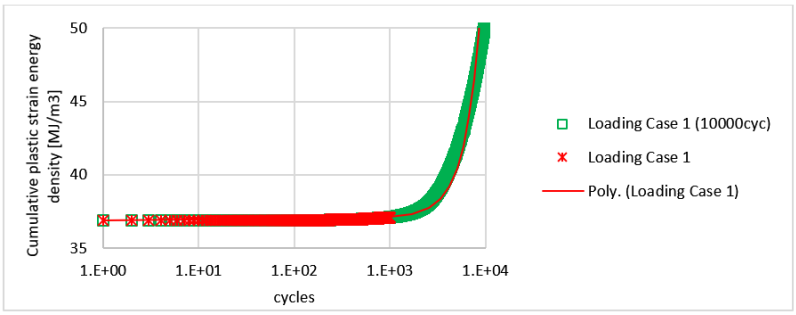

Figure 17: The comparison of results from the simulation of the first 1000 vs 10000 cycles for loading case 1

5 Summary and conclusion

Cyclic plasticity and fatigue performance of the mooring chain high strength steel grade R4 has been investigated using the data obtained from uniaxial strain-controlled fatigue tests on LCF specimens. The tests were divided into three parts; 1) single-step tests with the strain ratio of -1 and different constant strain ranges, 2) multi-step test with the strain ratio of -1 and varying strain amplitudes, and 3) tests with a constant strain range but different strain ratios. A non-linear combined kinematic and isotropic hardening model based on Armstrong-Frederick and Voce parameters has been used and calibrated to the experimental stress-strain curves. The calibrated material model has been employed in finite element simulations of pitted mooring chains at different service load levels to investigate

plastic straining at the pit sites and estimate the number of cycles for a pit to crack transition. Strain-energy based fatigue approach has been used to estimate the fatigue life of the tested specimens as well as pitted mooring chains. The methodology developed here can be used to assess the serviceability of notched components, in this case, mooring chains. The following are some important observations from this study.

- Analysis of the data from the test program Part 1 has revealed that the material experiences rapid cyclic softening for all strain ranges studied. The softening trend has not been influenced by the applied strain range and the softening ratio was almost constant and equal to 25% in all the tests. This lower strength of the material under cyclic load is especially important to the analysis of fatigue cracks initiation and propagation in the applications in which the component experiences near yield cyclic loadings e.g. pitted areas of mooring chains.
- The material's fatigue and hardening parameters have been identified using the test data Part 1. The cyclic elastic-plastic response of the material using the identified parameters has been numerically evaluated and showed to be in a good agreement with the test data. The material exhibits non-Masing behavior. Thus, the material cyclic stress-strain curves at different strain ranges cannot be numerically simulated using a singular set of hardening parameters. Hence, different sets of hardening parameters have been identified for different cyclic strain ranges.
- Analysis of the data from test Part 3 revealed that the trend of the mean-stress softening was similar for the specimens tested in the same strain range but different strain ratios. However, the amount of softening is directly proportional to the strain ratio.
- The strain energy density (SED) approach has been employed to estimate the fatigue life of the specimens. A decent agreement was observed between the experimental and the predicted fatigue life estimated using plastic and total SED obtained from numerical simulations.
- The calibrated non-linear material model has been used in the FE simulation of pitted mooring chains subjected to different cyclic loading cases. The pit at the chain crown has been identified as the most critical pit among the considered pits in the FE model. This statement is supported by the observed failure locations on fatigue tested corroded chain links. Closely looking at the pits, the maximum equivalent plastic strain has been observed at a location slightly below the mouth of this pit.
- Fatigue crack initiation from a pit on corroded chain links has been predicted employing the calibrated material model in FEM and SED approach. The predicted life is about 20 to 40% of the total life of corroded chain links tested in the lab. The effect of the mean load on the crack initiation life of corroded chains has been successfully captured and recognized to be larger than the effect of the load amplitude for the loading cases considered in this work.

Acknowledgement

The authors would like to acknowledge Equinor for providing the test material and financially supporting the experiments through the project KPN Lifemoor (RCN contract No: 280705), and the laboratory staffs at the structural engineering department of NTNU for their diligent work in performing the tests.

References

1. Fontaine, E., et al., *Industry Survey of Past Failures, Pre-emptive Replacements and Reported Degradations for Mooring Systems of Floating Production Units*, in *Offshore Technology Conference*. 2014, Offshore Technology Conference.
2. Ma, K.-t., et al., *A Historical Review on Integrity Issues of Permanent Mooring Systems*, in *Offshore Technology Conference*. 2013, Offshore Technology Conference.

3. Apos, R. Souza, and S. Majhi, *Application of Lessons Learned From Field Experience to Design, Installation and Maintenance of FPS Moorings*, in *Offshore Technology Conference*. 2013, Offshore Technology Conference.
4. ISO19901-7:2013, *Stationkeeping systems for floating offshore structures and mobile offshore units*, in *part 7 of Petroleum and natural gas industries specific requirements for offshore structures*.
5. DNVGL, *Offshore Standard DNV-OS-E302 Offshore Mooring Chain*. 2015, DNV GL AS.
6. Perez, I.M., P. Bastid, and V. Venugopal. *Prediction of Residual Stresses in Mooring Chains and its Impact on Fatigue Life*. in *ASME 2017 36th International Conference on Ocean, Offshore and Arctic Engineering*. 2017. American Society of Mechanical Engineers.
7. Bastid, P. and S.D. Smith. *Numerical Analysis of Contact Stresses Between Mooring Chain Links and Potential Consequences for Fatigue Damage*. in *ASME 2013 32nd International Conference on Ocean, Offshore and Arctic Engineering*. 2013. American Society of Mechanical Engineers.
8. Pacheco, P.M.C.L., et al. *Finite Element Residual Stress Analysis Applied to Offshore Studless Chain Links*. in *ASME 2004 23rd International Conference on Offshore Mechanics and Arctic Engineering*. 2004. American Society of Mechanical Engineers.
9. Pacheco, P.M.C.L., et al. *Analysis of the Influence of Mechanical Properties on the Residual Stress in Offshore Chain Links Using the Finite Element Method*. in *ASME 2003 22nd International Conference on Offshore Mechanics and Arctic Engineering*. 2003. American Society of Mechanical Engineers.
10. Pérez-Mora, R., et al., *Very high cycle fatigue of a high strength steel under sea water corrosion: A strong corrosion and mechanical damage coupling.* International Journal of Fatigue, 2015. **74**: p. 156-165.
11. Stiff, J.J., D.W. Smith, and N.F. Casey, *Fatigue of Mooring Chain in Air and Water - Results and Analysis*, in *Offshore Technology Conference*. 1996, Offshore Technology Conference.
12. Crapps, J., et al., *Strength Assessment of Degraded Mooring Chains*, in *Offshore Technology Conference*. 2017, Offshore Technology Conference.
13. Rosen, J., et al., *Chain FEARS JIP: Finite Element Analysis of Residual Strength of Degraded Chains*, in *Offshore Technology Conference*. 2015, Offshore Technology Conference.
14. Gao, Z., T. Moan, and S.E. Heggelund, *Time Variant Reliability of Mooring System Considering Corrosion Deterioration.* ASME 2005, 2005(41960): p. 203-210.
15. Huang, Y., S.-T. Tu, and F.-Z. Xuan, *Pit to crack transition behavior in proportional and non-proportional multiaxial corrosion fatigue of 304 stainless steel.* Engineering Fracture Mechanics, 2017. **184**: p. 259-272.
16. Huang, Y., et al. *Numerical Investigation of Stress Concentration Factor at Irregular Corrosion Pit Under Tension-Torsion Loading*. in *ASME 2014 Pressure Vessels and Piping Conference*. 2014. American Society of Mechanical Engineers.
17. Huang, Y., et al., *Quantitative correlation between geometric parameters and stress concentration of corrosion pits.* Engineering Failure Analysis, 2014. **44**: p. 168-178.
18. Cerit, M., K. Genel, and S. Eksi, *Numerical investigation on stress concentration of corrosion pit.* Engineering Failure Analysis, 2009. **16**(7): p. 2467-2472.
19. Turnbull, A., D.A. Horner, and B.J. Connolly, *Challenges in modelling the evolution of stress corrosion cracks from pits.* Engineering Fracture Mechanics, 2009. **76**(5): p. 633-640.
20. Horner, D.A., et al., *Novel images of the evolution of stress corrosion cracks from corrosion pits.* Corrosion Science, 2011. **53**(11): p. 3466-3485.
21. Xu, S.-h. and Y.-d. Wang, *Estimating the effects of corrosion pits on the fatigue life of steel plate based on the 3D profile.* International Journal of Fatigue, 2015. **72**: p. 27-41.
22. DNVGL, *Offshore standard DNVGL-OS-E301 Position mooring*. 2015, DNV GL AS.

23. Gabrielsen, Ø., K. Larsen, and S.-A. Reinholdtsen, *Fatigue Testing of Used Mooring Chain.* ASME 2017, 2017(57632): p. V001T01A072.
24. Totten, G., M. Howes, and T. Inoue, *Handbook of Residual Stress and Deformation of Steel*. ASM International.
25. Zhang, Y., N. Zettlemoyer, and P. Tubby. *Fatigue crack growth rates of mooring chain steels*. in *Proc. ASME 2012 31st Intl Conf. Ocean, Offshore and Arctic Engineering, OMAE2012-84223*. 2012.
26. ASTM, *E606/E606M-12, Standard test method for strain-controlled fatigue testing.* ASTM international, West Conshohocken (PA USA): Book of Standards, 2012. **3**.
27. Rampi, L., et al., *Chain Out of Plane Bending (OPB) Fatigue Joint Industry Project (JIP) FEA Results and Multiaxiality Study Results.* ASME 2016, 2016(49927): p. V001T01A002.
28. Ramberg, W. and W.R. Osgood, *Description of stress-strain curves by three parameters.* 1943.
29. Manson, S.S., *Behavior of materials under conditions of thermal stress*. 1954: National advisory committee for Aeronautics.
30. Coffin Jr, L.F., *A study of the effects of cyclic thermal stresses on a ductile metal.* Transactions of the American Society of Mechanical Engineers, New York, 1954. **76**: p. 931-950.
31. Armstrong, P.J., *A mathematical representation of the multiaxial Bauschinger effect.* CEBG Report RD/B/N, 731, 1966.
32. Golos, K. and F. Ellyin, *Generalization of cumulative damage criterion to multilevel cyclic loading.* Theoretical and Applied Fracture Mechanics, 1987. **7**(3): p. 169-176.
33. Branco, R.C., J.D.M.; Antunes, F.V.; Perdigão, S., *Monotonic and Cyclic Behavior of DIN 34CrNiMo6 Tempered Alloy Steel.* Metals, 2016. **6**(5): p. 98.
34. Jiang, Y. and J. Zhang, *Benchmark experiments and characteristic cyclic plasticity deformation.* International Journal of Plasticity, 2008. **24**(9): p. 1481-1515.
35. ABAQUS, V., *6.14 Documentation.* Dassault Systemes Simulia Corporation, 2014.
36. Rampi, L., et al. *Chain Out of Plane Bending (OPB) Fatigue Joint Industry Project (JIP) Static Test Program and OPB Interlink Stiffness*. in *ASME 2016 35th International Conference on Ocean, Offshore and Arctic Engineering*. 2016. American Society of Mechanical Engineers.
37. Fontaine, E., et al. *Investigation of Severe Corrosion of Mooring Chain in West African Waters*. in *The Twenty-second International Offshore and Polar Engineering Conference*. 2012. International Society of Offshore and Polar Engineers.
38. Fernández, J., W. Storesund, and J. Navas. *Fatigue Performance of Grade R4 and R5 Mooring Chains in Seawater*. in *ASME 2014 33rd International Conference on Ocean, Offshore and Arctic Engineering*. 2014. American Society of Mechanical Engineers.
39. Fontaine, E., et al. *SCORCH JIP - Feedback on MIC and pitting corrosion from field recovered mooring chain links*. in *Proceedings of the Annual Offshore Technology Conference*. 2014.
40. Fredheim, S., et al. *Corrosion Fatigue Testing of Used, Studless, Offshore Mooring Chain*. in *OMAE2013-10609. Nantes: 32nd International Conference on Ocean, Offshore and Arctic Engineering*. 2013.
41. Aursand, M. and B. Skallerud. *Numerical simulation of fatigue crack growth in offshore mooring chains*. in *10. National Conference on Computational Mechanics, MekIT'19*. 2019. Norway: CIMNE.

Paper 2: Experimental and numerical study of mooring chain residual stresses and implications for fatigue life

Zarandi, E.P. and B.H. Skallerud, Experimental and numerical study of mooring chain residual stresses and implications for fatigue life. International Journal of Fatigue, 2020. 135: p. 105530.

https://doi.org/10.1016/j.ijfatigue.2020.105530

Experimental and numerical study of mooring chain residual stresses and implications for fatigue life

Ershad P. Zarandi*[1], Bjørn H. Skallerud[1]
[1]Department of Structural Engineering
Norwegian University of Science and Technology (NTNU)
Richard Birkelands vei 1A, 7491, Trondheim, Norway
*corresponding author: ershad.p.zarandi@ntnu.no

Abstract

Residual stresses in large mooring chains were measured for the first time in this study. Two measurement techniques were employed (neutron diffraction and hole drilling). Elastic-plastic finite element simulation of the proof loading was conducted, and the computed residual stresses were compared to the experimental measurements. Further, the cyclic plasticity of the material was taken into account to investigate residual stress redistribution caused by introduction of corrosion pits and cyclic service loads. A critical damage parameter was employed to estimate fatigue crack initiation life of corroded mooring chains subjected to various service load levels considering the effect of residual stresses.

Keywords Residual stress; Neutron diffraction; Hole drilling; Finite element analysis; Crack initiation life estimation

1. Introduction

Sources of energy at sea and under the seabed have captured engineers' attentions from onshore to offshore productions in the past few decades. Accordingly, the number of the offshore production storage and offloading system has increased [1]. However, the uninterrupted operation of these offshore facilities necessitates the integrity of their mooring systems that hold these facilities in position during an operation when subjected to dynamic loads from wind, wave, and current as well as a continuous exposure to a corrosive environment. A single line failure increases the load level on the adjacent lines that may cause failure in them resulting in the operation shutdown, pollution, material loss and risking human life. The high rate of failure of offshore mooring chains demands enhanced understanding of the phenomena correlated to the fatigue life of these chains, e.g. residual stresses (RS) and corrosion, to improve their design and enhance their reliability against failure [1-3].

To assure the strength capability of mooring chains, offshore industry standards (e.g. see [4, 5]) require mooring chains to be proof load (PL) tested before being installed offshore. The test involves axially loading the chain up to 70% of its minimum breaking load (MBL) resulting in extensive plastic deformation and high RS in the chain links. To date, the offshore industry standards lack the consideration of the effects of PL level and material grade on fatigue life of different size mooring chains. The characterization of RS is essential as they directly affect the fatigue strength of materials by being added to the cyclic service stresses and act similarly as mean loads [6]. Finite element simulation of the PL test reveals that the predicted RS is highly dependent on the employed material model, chain dimensions, and PL level [7]. However, the results have not been validated experimentally.

Large-scale fatigue tests on new and used mooring chains in simulated seawater have been conducted in the past years, see e.g. [4, 8, 9]. However, little attention has been paid to characterizing the RS in the mooring chains. Dang Van fatigue criterion has been employed for lifetime estimation of non-corroded mooring chains [10]. Conservative predictions due to high compressive hydrostatic stress existing in the critical points were obtained for a typical studless chain link. Generally, an improved damage model combined with little knowledge of actual RS is sub-optimal and does not bring the

fatigue assessment methodology much further. Hence, providing quantitative information on RS in safety-critical components such as mooring chains is of high technical value.

Several investigations have indicated the significance of corrosion on mooring chains fatigue life [11, 12]. The formation of small corrosion pits that can act as stress raisers at the chain link surface results in the reduction of the chain fatigue life [13, 14]. Numerical investigations have been carried out on flat and cylindrical specimens employing elastic-plastic material models as well as experimental observation to determine strain localization and elastic-plastic stress distribution around critical pits and their transition into cracks [15-19]. Although the global RS distribution might not change significantly in the chains due to corrosion, the local RS distribution around corrosion pits dramatically changes as a result of plastic straining around pitting holes, and influence pit to crack transition and the crack growth. Therefore, the knowledge of current RS state is of great importance and can be obtained knowing the material's cyclic plastic properties. Further, knowledge of the initial RS state is essential for the prediction of the RS redistribution over the chain service life.

To date, no RS measurement has been carried out on large-scale mooring chains. In this study, the hole-drilling (HD) technique has been used to measure RS close to the surface of mooring chains, though, the curved surface of the chains as well as corrosion pits made the application of the HD technique challenging. Additionally, neutron diffraction (ND), a non-destructive technique indifferent to surface finish that can provide tri-axial through-depth measurements including RS gradients, has been employed for deeper measurements. Two chain links with the same size and material, one only subjected to proof load and no cyclic service loads and the other exposed to service loads as well as the proof load, were selected for the experiment to investigate RS changes after several years of service. The experimental measurements are compared with the RS predicted by finite element modeling (FEM) of proof loading. Further, the cyclic plasticity of the material is taken into account to investigate RS redistribution caused by local corrosion pits and cyclic service loads. The Fatemi-Socie multiaxial damage parameter [20] combined with Roessle-Fatemi hardness method [21] is employed to estimate fatigue crack initiation life of corroded mooring chains at various service load levels considering the effect of RS. The estimated lives were compared with experimental lives obtained from large-scale fatigue tests.

2. Methodology

2.1. Material and experimentation details

Two mooring chain links with $114\ mm$ nominal diameter (D) and made of steel grade R4 have been selected for the RS measurements. The links were made by the same manufacturer following the same manufacturing procedure (welding, heat treatment, and proof loading), thus, it can be assumed that RS in both links right after production were identical. One link had been exposed to the sea loads for 18 years prior to the experiment. The link, which is here referred to as the used link, had some corrosion evidence at the surface. The other link was 10 years old at the time of the experiment but had never been exposed to any cyclic service loads, as it was laid on the vessel's deck during its service life. The link, which is here referred to as the unused link, has a relatively smooth surface – close to its initial as-produced surface. The chosen links are pictured in Figure 1. The monotonic mechanical material properties of the tested chain material are provided in [19]and listed in Table 1.

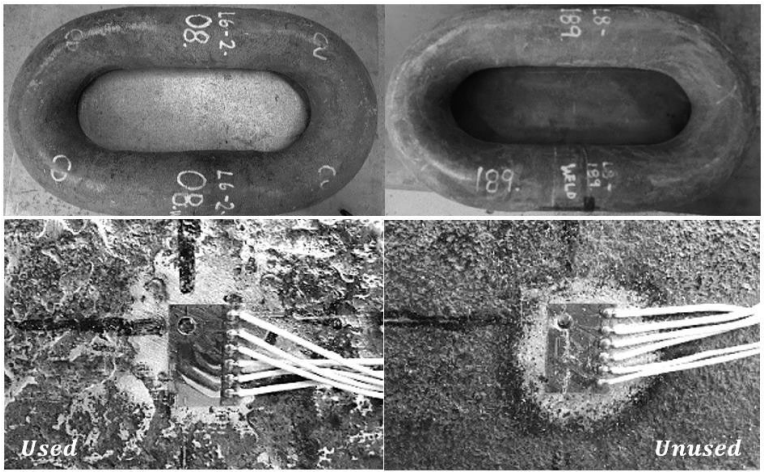

Figure 1: Chain links chosen for the experiments and the surface condition around the measurement points at the crowns using the HD technique

Several locations on each link were specified for the RS measurements; one at the middle of the bent part (known as the chain crown) that is recognized as the most critical location from the fatigue viewpoint [9] and the others at the straight parts to compare RS in the base and weld material. Marking of the measuring locations on the links was rather convenient enabling a point-to-point comparison between the two links and FE simulations. The measurement paths are illustrated in Figure 2. Local cylindrical coordinate systems at every location are defined such that radial stresses are along the R-axis, hoop stresses along the θ-axis, and longitudinal stresses along the Z-axis. Considering the geometry of the chains and loading conditions, it is assumed that these axes are principal axes.

Table 1: Mechanical material properties of the mooring chain steel grade R4

Elasticity modulus ($\boldsymbol{E}$)	[GPa]	207
True yield stress ($\boldsymbol{R_{p0.2}}$)	[MPa]	843
True ultimate stress ($\boldsymbol{R_m}$)	[MPa]	1010
Total extension at maximum force ($\boldsymbol{A_{gt}}$)		0.071
Area reduction		0.68
Poisson's ratio		0.3
Average hardness	[HB]	300

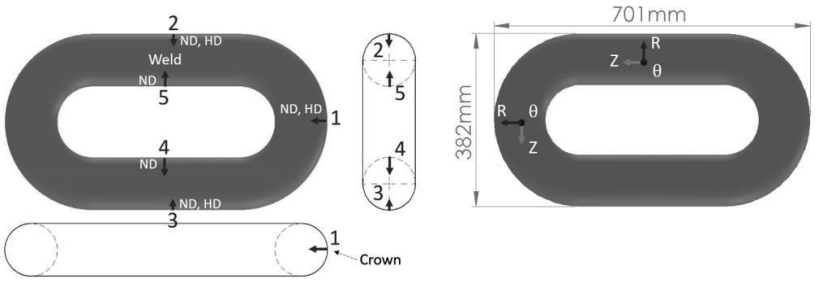

Figure 2: Schematic of the tested chain links and the measurement paths (ND: neutron diffraction, HD: hole drilling)

2.2. Residual stress measurement techniques

2.2.1. Neutron diffraction

Neutron diffraction technique has proven to be a useful tool in characterizing subsurface RS of metallic materials [22-25]. In this approach, the lattice spacing, which works as an atomic strain gage, of the stressed material is compared to that of a stress-free sample made from the same material providing the locked strain in the bulk material. Assuming that the measurement axes are aligned with the principal axes, using Hooke's law, and the measured strains (ε), one can calculate the RS as follows:

$$\varepsilon_i = (d_i - d_0)/d_0 \qquad ,i = r,\theta,Z$$
$$\sigma_i = \frac{E}{1+\nu}[\varepsilon_i + \frac{E}{1-2\nu}(\varepsilon_r + \varepsilon_\theta + \varepsilon_z)] \tag{1}$$

where d_0 denotes the average value of the lattice spacing of the stress-free crystalline material and d_i are the lattice spacings of the stressed material along the three perpendicular measurement axes. E denotes the material's Young's modulus, ν is the Poisson's ratio. It is worth noting that unlike the HD technique, the ND technique can provide a 3D characterization of the RS state in the material.

In the first part of the experimental work, deeper RS measurements at the specified locations on the links using this technique was carried out at STFC Rutherford Appleton Laboratory. The experiment was conducted using ENGIN-X, a 50m flight path instrument. To obtain 3D RS, the heavy chain links ($130Kg$ each) had to be positioned in various orientations, as in each orientation only the lattice spacing along two perpendicular axes could be measured. To facilitate this challenging task, wooden frames were designed for the links when sitting on the rotatable/movable table in ENGIN-X. The experimental setup is illustrated in Figure 3. A 4x4x4mm gauge volume was used to enable measurements further below the surface at a reasonably short time considering the limited beamtime access and neutrons' maximum penetration capability into steels. To ensure complete filling of the gage volume in the material, the center of the gage volume was precisely positioned 3 and 4 mm below the surface using theodolites. Small T-shape samples were cut from the straight parts (both the welded side and non-welded side) of the neighboring chain link to the unused chain link and used to identify the lattice spacing of the stress-free material (d_0). The above-mentioned setup provided the RS at 3 and 4mm below the surface.

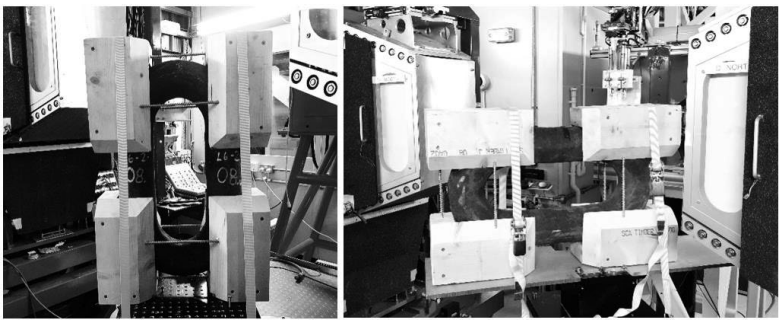

Figure 3: The ND experimental setup at ENGIN-X

2.2.2. Hole drilling

In this technique, after preparing the specimen surface, a small hole is drilled/milled incrementally into the material at the center of the strain rosette that is glued to the specimen. The released strains at each increment are measured by the strain gauges. The RS are calculated utilizing the measured released strains and Hooke's law. Assuming a non-uniform stress profile through the hole in thick workpieces as:

$$\begin{aligned} p_j &= (\varepsilon_3 + \varepsilon_1)_j/2 & P &= -\frac{E}{1+\nu}\frac{\Sigma(\bar{a}\cdot p)}{\bar{a}^2} & (\sigma_x)_j &= P_j - Q_j \\ q_j &= (\varepsilon_3 - \varepsilon_1)_j/2 & Q &= -E\frac{\Sigma(\bar{b}\cdot q)}{\bar{b}^2} & (\sigma_y)_j &= P_j + Q_j \\ t_j &= (\varepsilon_3 + \varepsilon_1 - 2\varepsilon_2)_j/2 & T &= -E\frac{\Sigma(\bar{b}\cdot t)}{\bar{b}^2} & (\tau_{xy})_j &= T_j \end{aligned} \quad (2)$$

where j refers to the sequential numbers of the hole depth steps, ε_1, ε_2, and ε_3 are measured along the three in-plane axes of the attached strain gages. $\bar{a}$ is the calibration constant for isotropic equi-biaxial stress (P) and $\bar{b}$ is the calibration constant for 45° shear stress (Q) and xy shear stress (T) respectively and tabulated for various hole depths in ASTM E837-13a [26]. It is worth noting that, using this technique, only a 2D stress state can be characterized and the RS along the axis normal to the surface is assumed to be zero through the depth of the hole.

In the second part of the experimental work, the RS at and close to the outer surface of the chain links were measured using this technique at SINTEF in Trondheim. A thin layer of the rust on the surface was removed using very fine Scotch-Brite surface conditioning discs. The strain rosette type 1-RY61-1.5/120K connected to an electronic measuring system (Spider8) was used to record the strain variation during incremental hole milling using the MTS-3000 instrument. The instrument is equipped with an air turbine enabling the end mill to spin at a speed of 400000 rpm to avoid the introduction of RS during the milling process [27]. The end mills used in the experiment are inverted truncated-cone shaped with flat ends (1-SINTCTT/1), with a maximum shank diameter of 1.60 mm. The above-mentioned setup has provided the measurement of RS at a distance of up to 1mm below the surface.

2.3. Fatigue life calculation

The Fatemi-Socie multiaxial damage parameter [20] combined with Roessle-Fatemi hardness method [21] has been employed to estimate crack initiation life of corroded mooring chains considering the present triaxial stress state and RS effect.. Using this multiaxial strain-stress based critical plane approach, satisfactory fatigue life estimations were obtained for a wide range of steels and loading conditions [28, 29]. The maximum shear strain amplitude ($\Delta\gamma_{max}/2$) as the primary parameter driving the crack and the maximum normal stress acting on the maximum shear strain plane ($\sigma_{n,max}$) as the secondary parameter are related to the fatigue life (N_f) as:

$$\begin{gathered} \frac{\Delta\gamma_{max}}{2}\left(1 + k\frac{\sigma_{n,max}}{R_{p0.2}}\right) = \left[A(2N_f)^{-0.09} + B(2N_f)^{-0.56}\right]\left[1 + kC(2N_f)^{-0.09}\right] \\ k = [0.0003(HB) + 0.0585](2N_f)^{0.09} \end{gathered} \quad (3)$$

where $R_{p0.2}$ is the material's yield stress, $A, B,$ and C are parameters given as a function of the material's Brinell hardness (HB, see Table 1):

$$A = \frac{5.53(HB) + 293}{200000}, \quad B = \frac{0.48(HB)^2 - 731(HB) + 286500}{200000}$$
$$C = \frac{1}{0.0022(HB) + 0.382} \tag{4}$$

3. Experimental results

The data presented in this section is provided in detail in [30].

3.1. Measurements at the crown

The RS at the crown of the chain links have been measured and the results are presented in Figure 4. It is seen that:

- The RS in all measurement directions are compressive in both links except the hoop RS measured by HD technique.
- The radial RS are approximately 1/4 of the longitudinal RS, which are the largest in magnitude at this region. The radial RS cannot be measured by the HD technique.
- The hoop RS measured by the ND technique are about 1/3 of the longitudinal RS.
- Using the ND technique, the RS gradients in the used chain link are opposite to that in the unused link in all measurement directions. That is, RS tends decrease with depth for the unused chain and increase with depth for the used chain. For shallower depths with the HD technique, the two links show the similar gradients with slightly lower RS in the unused link.

The last observation can be caused by the material removal at the chain surface due to the corrosive environment (in the form of corrosion pits, as seen in Figure 1) and the cyclic straining as a result of cyclic service loads intensified by the stress concentration factor at the pit site. This results in the redistribution of RS in the material near the surface.

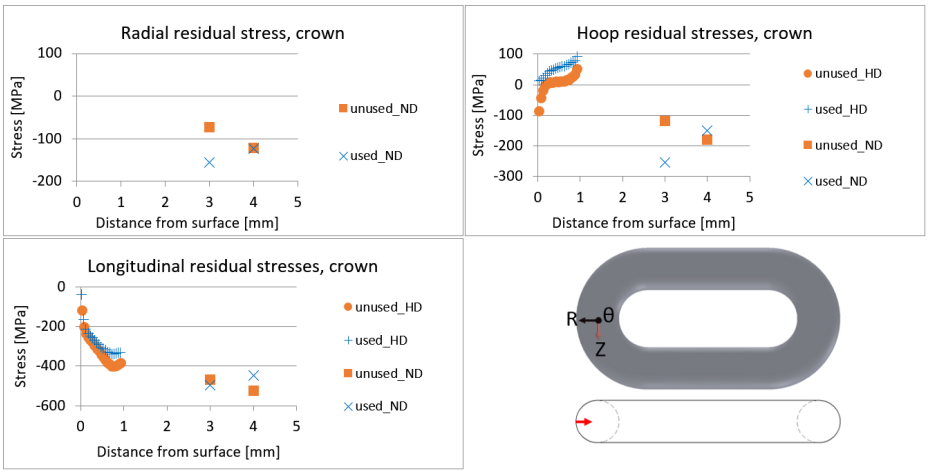

Figure 4: Comparison of residual stresses measured at the chains' crowns (location 1) using the HD and ND techniques respectively; the red arrow indicates measurement location

3.2. Measurements at the straight part (welded side)

The RS measured at location 2 on the straight part (welded side) of the links are presented in Figure 5. It is seen that:

- The RS are compressive in all three measurement directions in both chain links.
- The hoop RS gradient obtained by the HD technique on the used link is opposite to that on the unused link.
- The radial RS measured by the ND technique is about 1/2 of the longitudinal RS and almost of the same order as the hoop RS.

Due to the beamtime access limitation, in this location, the calculation of the RS in the ND technique is based on a 2-axis measurement (hoop and longitudinal) and thus, the radial strain was set to zero when calculating RS using Equation (1).

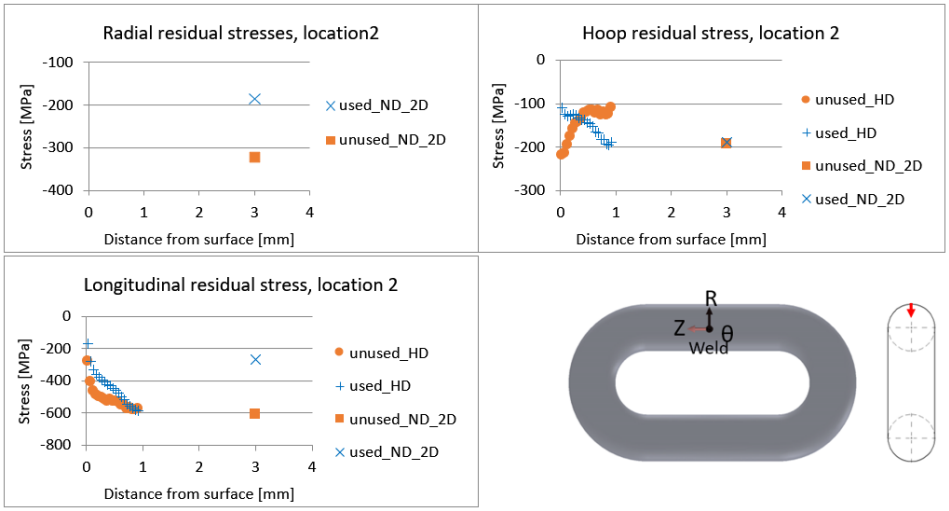

Figure 5: Comparison of residual stresses measured at the weld part of the chains (location 2) using the HD and ND techniques, the ND results with no radial strain measurement ($\varepsilon_r = 0$) have a _2D suffix; the red arrow indicates measurement location

Figure 6 presents the measured RS at the inside of the weld region (location 5). The application of the HD technique in this location was not possible due to limited space between the two straight parts of the links. It is seen from Figure 6 that:

- The measured RS are compressive in all directions in both chain links.
- The radial RS are approximately 1/3 and the hoop RS are about 1/2 of the longitudinal RS.
- The near-surface RS on the used link are smaller.
- The stress gradients on the used and unused chains follow a similar trend (increasing in magnitude by depth), however, the stress gradients in the used link (almost -200 MPa/mm in all 3 directions) are steeper than that in the unused link.

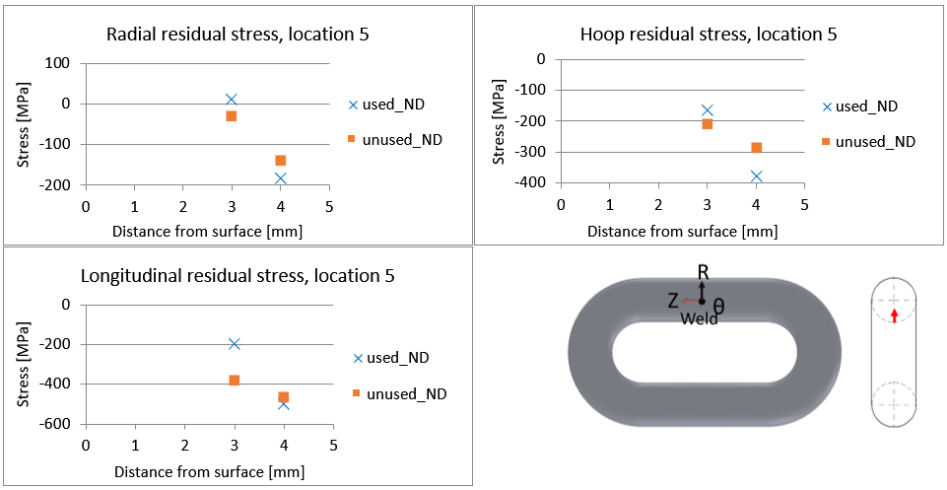

Figure 6: Comparison of residual stresses measured at the weld part of the chains (location 5) using the ND technique; the red arrow indicates measurement location

3.3. Measurements at the straight part (non-welded material)

The RS measured at location 3 on the straight part (non-welded side) of the links are presented in Figure 7. It is seen that:

- The RS are compressive in all three measurement directions in both chain links.
- The radial and hoop RS, measured by the ND technique, are approximately 1/2 of the longitudinal RS.
- The unused link has smaller RS, measured by the ND technique, in all three directions. This was opposite in the weld region (location 2).

Due to the beamtime access limitation, in this location, the calculation of the RS in the ND technique is based on a 2-axis measurement (hoop and longitudinal) and thus, the radial strain was set to zero.

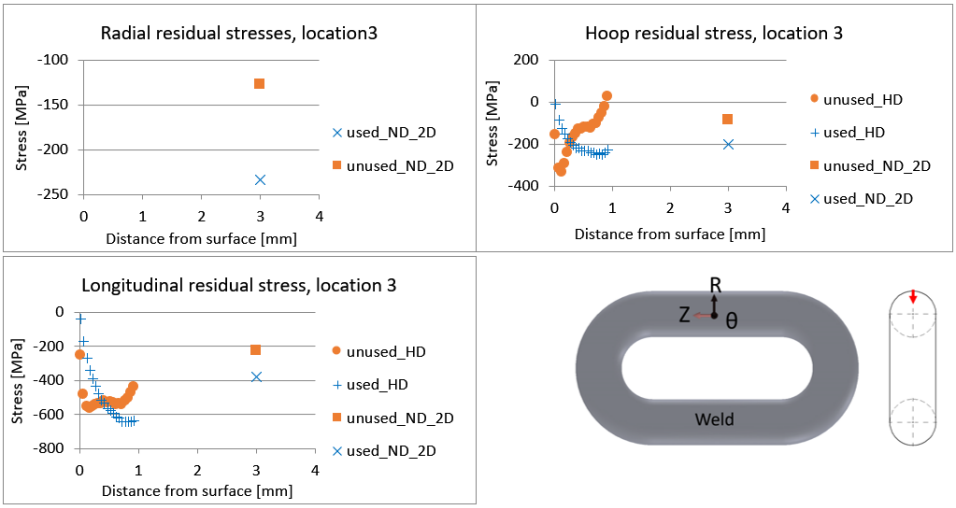

Figure 7: Comparison of residual stresses measured at the straight part of the chains (location 3) using HD and ND techniques; the red arrow indicates measurement location

Looking at the RS measured inside the straight part (location 4) of the chain links presented in Figure 8. The application of the HD technique in this location was not possible due to limited space between the two straight parts of the links. From Figure 8, it is seen that:

- The near-surface RS on the unused link are smaller. This was opposite in the weld region (location 5).
- The radial RS are approximately 1/3 and hoop RS are about 1/2 of the longitudinal RS.
- The RS gradients in the used link are opposite to them at location 5. Thus, in the weld part, faster crack initiation and slower (or even trapped) crack growth is expected, while in the straight part, slower crack initiation with a faster crack growth could occur.
- The RS gradients in the used chain link are less steep, and in opposite direction, compared to the unused link.

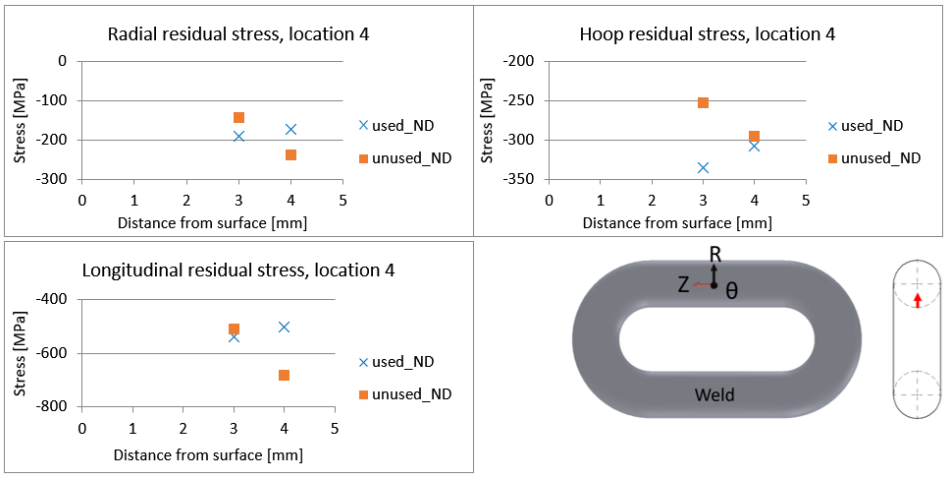

Figure 8: Comparison of residual stresses measured at the straight part of the chains (location 4) using the ND technique; the red arrow indicates measurement location

4. Finite element simulation of pitted mooring chains

A model consisting of one complete chain link ($D = 114mm$) and two half links is constructed. To reduce the computational efforts, only 1/8 portion of the model with three symmetry planes (XY, YZ, XZ) are used in the analysis, as shown in Figure 9. Hard contact with standard constraint enforcement method and a stiffness scale factor of 0.01 is applied to the chains' contact regions. A friction coefficient of 0.3 is used for the tangential behavior of the interaction [31]. First-order hexahedral elements with reduced integration schemes (C3D8R) are used, and mesh convergence has been carried out with a finer mesh close to the surface in order to capture RS gradient optimally. The mesh study has been presented in [19]. The material model used in this study combines kinematic and isotropic hardening based on Armstrong-Frederick and Voce parameters, respectively, and is applied in Abaqus software to study the RS redistribution at the pit sites on chain links during the service life (as described and calibrated in [19]). The parameters for the cyclic plasticity analysis of mooring chain steel grade R4 are calibrated such that the material model can simulate both transient and stabilized material response; the parameters are listed in Table 2. Using the calibrated parameters, the stress-strain curve in the first quarter of the first cycle resembles the stress-strain curve from the tensile test. Also note that R4 steel has similar behavior in tension and compression and shows a large cyclic softening response [19].

The proof load (PL) is defined as 70% of the minimum breaking load ($MBL = 12420KN$) [8]. The load is applied at a reference point (RP) which has restricted degrees of freedom (DOFs) in all directions except along the loading axis, i.e. X-axis. The DOFs of the half-chain cross-sections (loaded faces) at the straight parts are kinematically coupled to DOFs of the RP except along the Y-axis. To investigate the effect of corrosion pits on the RS redistribution, a hemispherical pit with 4mm depth ($a = 4mm$) and aspect ratio ($a/2c$) of 0.5 is introduced to the model after proof load removal using model change interaction in Abaqus/standard. The modeled pit is located at the chain crown where fatigue cracks are frequently observed [9, 32, 33]. Subsequently, nominal service loads (the force applied on the cross-section area of the straight parts of a chain link) are applied at the RP. The service load includes a mean load (ML) and a cyclic load (CL) caused by wind, wave, and current. In this study, different service load levels based on what typical mooring chains experience during their service lives are used to investigate the RS redistribution in a pitted studless mooring chain link during its service life. Note that the cyclic load levels correspond to extreme storm situations and the load levels employed in large-scale testing in order to have manageable test durations. Only tension-tension fatigue is considered. Also note that despite the chains being globally load controlled, the loading condition at the pit site can be assumed to be strain-controlled as the plastic zone at the pit site is fairly constrained by the elastic material around it. The loading and boundary conditions are presented in Figure 9c and Figure 9a respectively. The FE results are presented for two paths at the chain crown, shown in Figure 9b.

Table 2: Parameters for combined kinematic with isotropic hardening model identified for the mooring chain steel grade R4 [19]

$\boldsymbol{\sigma_0}$ $[\boldsymbol{MPa}]$	$\boldsymbol{Q_\infty}$ $[\boldsymbol{MPa}]$	$\boldsymbol{b}$	$\boldsymbol{c}$ $[\boldsymbol{MPa}]$	$\boldsymbol{\gamma}$
546	-227	3.1	536565	1500

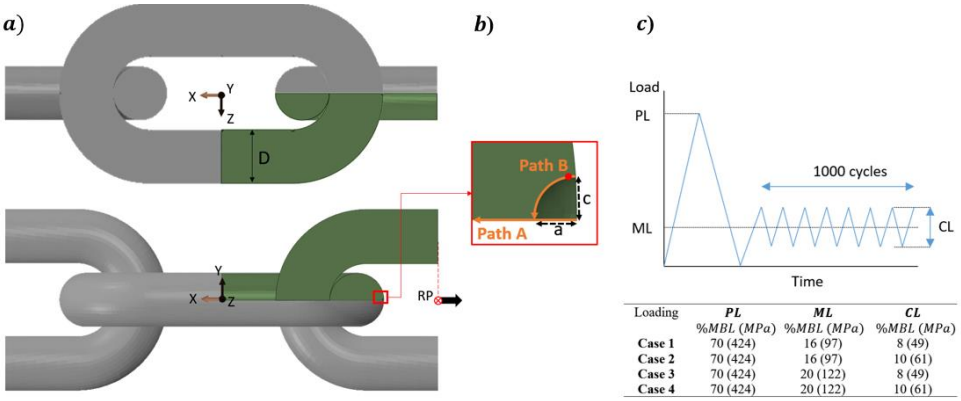

Loading	PL %MBL (MPa)	ML %MBL (MPa)	CL %MBL (MPa)
Case 1	70 (424)	16 (97)	8 (49)
Case 2	70 (424)	16 (97)	10 (61)
Case 3	70 (424)	20 (122)	8 (49)
Case 4	70 (424)	20 (122)	10 (61)

Figure 9: a) finite element model of chain links with the considered 1/8 of the entire volume (shaded), b) details of the modeled corrosion pit with the critical point (solid circle), and c) details of the applied nominal loads

The FEM predictions of the initial state of RS (right after the proof load removal) and the experimental measurements at the crown are presented in Figure 10. It is seen that the FE modeling of proof loading alone cannot predict the radial and hoop in-depth RS properly, as there can be some RS in the material from the heat treatment process that is carried out before proof loading. These RS are due to nonhomogeneous plastic deformation caused by different heating/cooling times of the material at the surface and in the core of chain rods. They appear in all three principal directions defined herein, however, the longitudinal RS are later replaced by greater RS from proof loading. The close agreement between the FEM predictions and the measurements of longitudinal RS supports this statement. Well-predicted longitudinal RS, which are also the largest in magnitude, are important when fatigue crack growth is of interest as these stresses are normal to the crack faces commonly observed in the fractured chain links.

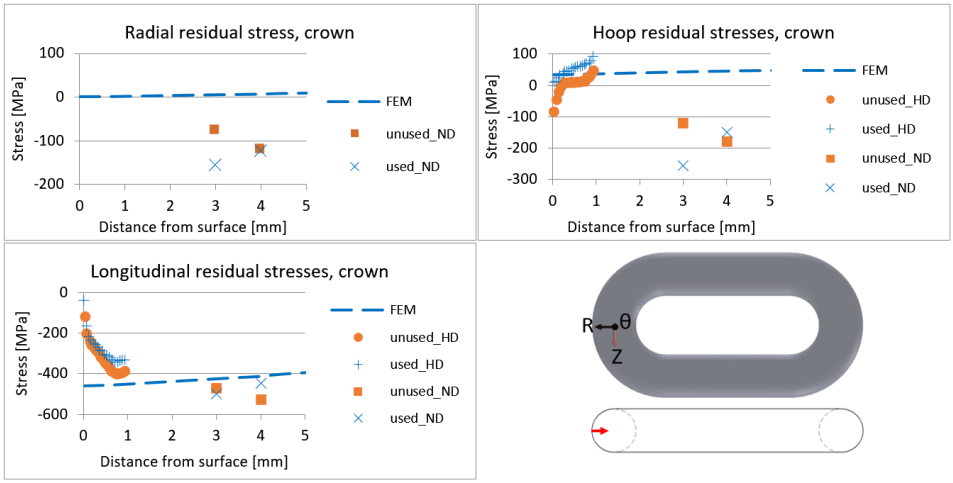

Figure 10: Comparison of residual stresses measured at the chains' crowns using HD and ND techniques with FEM predictions

The RS redistribution due to corrosion pitting and cyclic straining at the pit site is investigated at the chain crown. The computed distribution of longitudinal RS along path A (starting from the outside of the chain crown towards the contact point) before and after 1000 service load cycles are presented in Figure 11. It is seen that the material removal due to corrosion is not the main reason for the RS redistribution. Instead, the stress concentration because of the presence of the pit results in cyclic straining at the pit site ending up with a significant local change in the longitudinal RS at the bottom of the pit. In the case studied here, the stress concentration around the modeled pit resulted in introduction of higher compressive RS at the pit tip. This is also seen in the RS measured by the ND technique at this region, see Figure 10, where more compressive RS were measured at a shallower depth in the used link (i.e. closer to the real corrosion pits at the chain link surface). This change is influenced by the load range (i.e. higher compressive RS as a result of a higher applied load range) but not by the mean load.

The longitudinal RS are compressive up to $40mm$ below the chain outer surface at the crown. However, the superposition of the longitudinal stress due to service loads and RS becomes tensile at a much shorter distance from the surface, see Figure 12 and Figure 13. One should note that the overall longitudinal stress remains tensile up to half-diameter of the chain. This is important to fatigue crack growth analysis as this tensile stress will facilitate the crack growth.

Fatigue crack initiation lives of the modeled chain links with a corrosion pit for different loading cases are estimated using the multiaxial fatigue criterion described in Section 2.3. $\Delta\gamma_{max}/2$ and $\sigma_{n,max}$ are computed using the principal stresses and principal strains at the critical point extracted from the FEM results. Cyclic elastic-plastic strain analysis of pitted mooring chains has identified a point located on the pit wall and just below the pit mouth, in which accumulated plastic strain is maximum, as the critical point from the fatigue initiation point of view [19]. This critical point is shown in Figure 9b. Comparison of the estimated lives in Table 3 based on the strain and stress values at this point and a point at the bottom of the pit confirms that fatigue cracks initiate from the identified critical point on the pit wall. Hence, attention will be paid to this critical point for the rest of this article. Three scenarios are considered; first, the RS are neglected (i.e. a non-proof loaded chain link), second, the initial RS state (right after proof load removal) are considered to remain unchanged during the fatigue process, and third, the stable RS state (RS after 1000 cycles of service load) are employed for fatigue life estimation. The estimated fatigue crack initiation lives using Equation (3) are presented in Table 4. Very short lives are predicted for the non-proof loaded chain link as the effect of high compressive RS is neglected. This was also observed in the fatigue test carried out on the small lifting chains, where the non-proof loaded chains had significantly shorter lives than the proof loaded chains [34]. The estimated lives for the proof loaded chain link with the RS taken directly after proof load removal are 30% shorter (more conservative) than the case where the stable RS were used in the calculations.

The experimental fatigue lives of the corroded chain links ($D = 114mm$, grade R4) tested in simulated seawater in the lab (3.5% sodium chloride) and predictions using S-N curves presented in DNVGL-OS-E301 [8] are also provided in Table 4. In the large-scale tests, the failure was defined as a through thickness crack. The estimated crack initiation life considering the stable RS state is about 14 to 34% of the experimental (total) life depending on the applied load. It is seen that the load amplitude has a larger effect than the mean load on the fatigue crack initiation life of pitted chains subjected to the loading cases studied here. For example, comparing loading case 1 with 3, a 25% increase in the mean load at the load amplitude of 8% MBL resulted in a 15% decrease in the predicted crack initiation life while comparing loading case 1 with 2, a 25% increase in the load amplitude made the initiation life 75% shorter. The effect of the mean load is more pronounced at

lower load amplitudes. It is worth noting that unlike the DNVGL S-N curve in predicting total fatigue lives, this approach can account for the effect of the mean load as well as the load amplitude on the fatigue crack initiation life of pitted mooring chains.

Table 3: Estimated crack initiation lives based on the stress and strain values at the pit bottom and critical point on the pit wall

	Pit bottom			Critical point on the pit wall		
Loading	$\sigma_{n,max}$ [MPa]	$\Delta\gamma_{max}/2$	**Cycles**	$\sigma_{n,max}$ [MPa]	$\Delta\gamma_{max}/2$	**Cycles**
Case 1	-1	0.00397	194,682	-39	0.00414	169,440
Case 2	-15	0.00495	52,429	-29	0.00517	43,206
Case 3	51	0.00396	163,397	15	0.00412	143,833
Case 4	44	0.00494	45,357	8	0.00515	40,173

Table 4: Stress and strain values at the critical point on the pit wall, the estimated crack initiation life, and experimental total life

Loading	N_f *experimental* **Cycles**	N_f *DNVGL* **Cycles**	Non-proof loaded link			Proof loaded link, initial RS state			Proof loaded link, stable RS state		
			$\sigma_{n,max}$ [MPa]	$\Delta\gamma_{max}/2$	**Cycles**	$\sigma_{n,max}$ [MPa]	$\Delta\gamma_{max}/2$	**Cycles**	$\sigma_{n,max}$ [MPa]	$\Delta\gamma_{max}/2$	**Cycles**
Case 1	501872*	520436	488	0.00498	18,348	53	0.00417	116,585	-39	0.00414	169,440
Case 2	318174*	266430	496	0.00616	8,035	92	0.00528	29,044	-29	0.00517	43,206
Case 3	-	520436	500	0.00491	19,102	132	0.00413	96,976	15	0.00412	143,833
Case 4	126614**	266430	502	0.00620	7,795	171	0.00516	27,434	8	0.00515	40,173

*Reported by Fredheim et al. in [35]
** Unpublished report

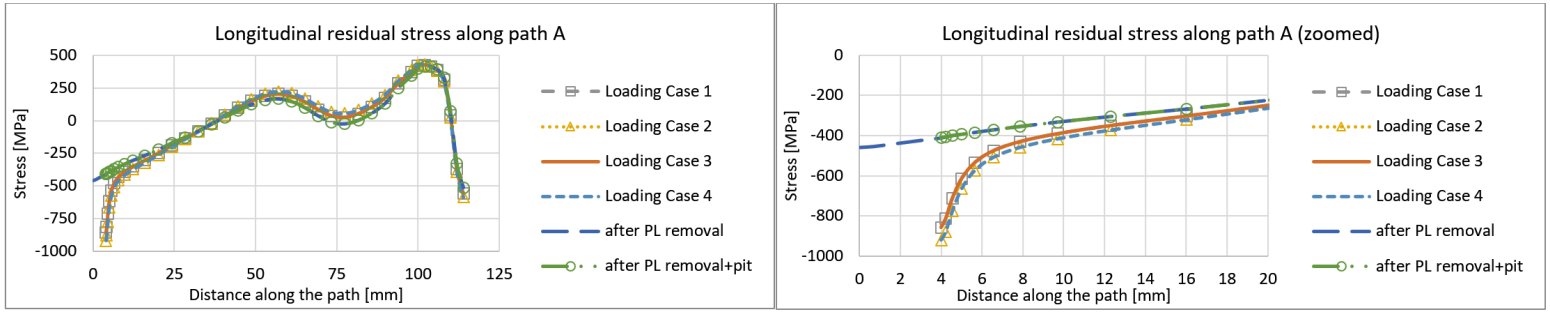

Figure 11: FE results, longitudinal residual stresses distribution along path A at the crown after proof load removal and after 1000 cycles of different service loads

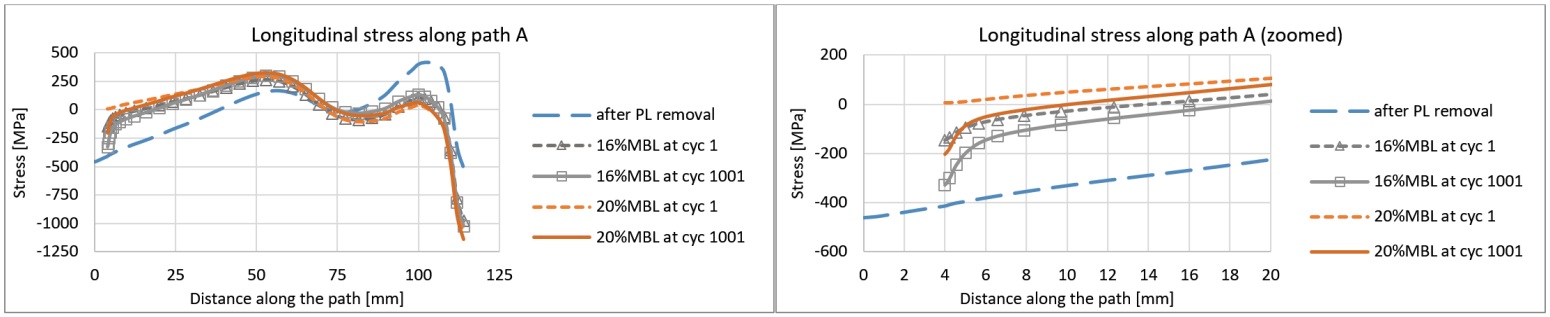

Figure 12: FE results, longitudinal stress distribution along path A at the crown at the mean load of 16 and 20% MBL before and after 1000 cycles of loading cases 1 and 3 respectively

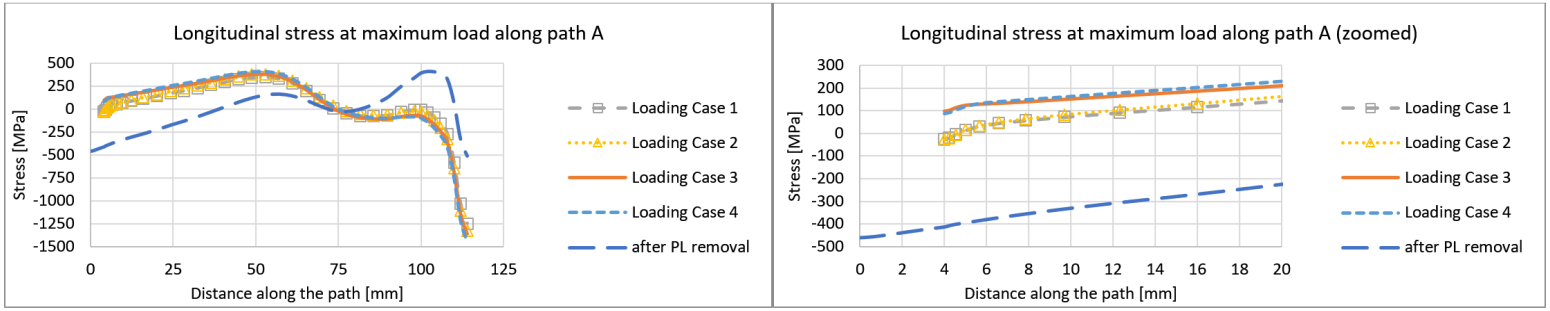

Figure 13: FE results, longitudinal stress distribution along Path A at the crown at the maximum load at different loading cases after 1000 load cycles

5. Discussion

It must be noted that measuring RS at the surface of a component using the HD technique is challenging, as in this technique RS are calculated using the measured released strains by strain gauges after each drilling increment and since at the first few increments these strains are very small, the corresponding calculated RS are small as well. This can be seen in almost every RS measured by this technique. Hence, the calculated RS may not represent the actual RS at the component surface. Therefore, the authors recommend taking the average value of the measurements in the second half of the hole depth to be representative for the RS at this half.

The complete picture of the RS in the material measured by the ND technique is essential when investigating crack growth considering crack closure. This is the case in fatigue analysis of mooring chains due to high compressive RS. The HD technique is an approach that provides in-plane RS measurement only while the ND technique gives a 3D measurement. The results from ND tests show that there are considerable radial RS (in the order of 1/3 of the maximum absolute residual strain at every point of investigation) inside the chain links (both used and unused). These RS, which are mainly from the manufacturing process, are not captured by the HD technique. As a result, the RS calculated from the 2D strain measurement do not represent the actual 3D RS in the chain material. For the sake of comparison, the radial residual strains measured in the ND technique are set to zero in Equation (1) and the hoop and longitudinal RS at the chain crown are calculated correspondingly. The results are presented in Figure 14. It is seen that the longitudinal and hoop RS calculated based on the 3D strain measurement are, respectively, 10 and 25% greater than those calculated based on the 2D strain measurements. Nevertheless, if the purpose of an experiment is to qualitatively compare the RS in two mooring links, e.g. redistribution/change of RS over a service time, the HD technique could be used as a cheap and relatively quick alternative.

From the fatigue perspective, the FE predictions of RS considering PL only are on the safe side as it predicts zero radial RS instead of the actual compressive RS just below the surface of the chain crown, see Figure 10. Alternatively, an enhanced FE model that takes the heat treatment process into account may provide a better prediction of RS in the radial directions. However, to account for this, the material properties at elevated temperatures need to be characterized.

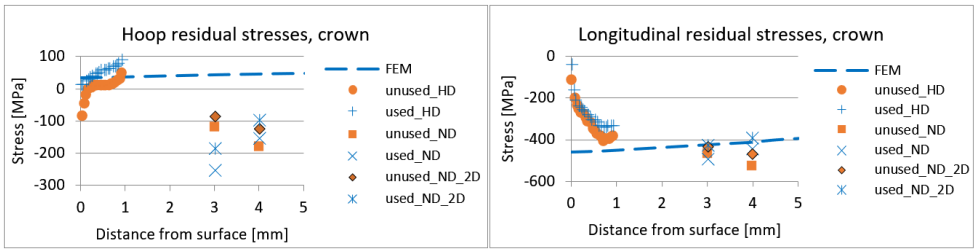

Figure 14: Residual stresses at the crown, the ND results with $\varepsilon_r = 0$ have a 2D suffix

The Fatemi-Socie multiaxial damage parameter combined with Roessle-Fatemi hardness method is an efficient method for fatigue life estimations while hardness and yield stress are the only material parameters required. Further, it provides life estimations in the applications, in which large compressive RS present in the material. The Dang Van criterion [36] gives very conservative life estimations in such a condition [10] and the Smith-Watson-Topper parameter [37] fails to predict fatigue life when the maximum stress normal to the crack plane is compressive.

The estimated lives presented in Table 4 show how different the predictions can be depending on the choice of the RS state used in the fatigue life calculation. The important role of RS on fatigue life is well accepted and thus, neglecting RS does not seem to be a reasonable choice. For simplicity, one could use the initial RS state in the fatigue crack initiation and growth models. However, it should be noted that the fatigue life estimation criteria that do not account for the RS redistribution lead to incorrect (generally more conservative) remaining life predictions, as RS change cycle by cycle as a result of cyclic plastic straining at the tip of a growing pit/crack even though the nominal load is below the materials yield limit.

In this study, different service load levels corresponding to extreme storm situations and the load levels employed in large-scale testing were studied. However, the approach is general, and a more detailed loading condition (e.g. considering several sea states) can be used in the simulation. The maximum shear strain range and the maximum normal stress on the maximum shear strain plane for each sea state can be obtained from FE simulation and using e.g. Palmgren-Miner rule, one can estimate the crack initiation life of a pitted chain link subjected to a more typical loading condition. However, the sea state data at the specific geographical location of the offshore vessel under study is required for such an assessment.

6. Conclusion

Residual stresses (RS) in offshore mooring chains have been measured for the first time. Two chain links with the same size and material, one only subjected to proof load and no cyclic service loads (herein referred to as the unused link) and the other exposed to service loads as well as the proof load (herein referred to as the used link), were selected for the experiment to investigate RS changes over the service life. The RS just below the surface were measured using the hole the drilling (HD) technique and the neutron diffraction (ND) technique has been employed for deeper measurements. Finite element (FE) simulation of the proof loading as well as cyclic service loads has been done to investigate the RS redistribution around a typical corrosion pit at the chain surface. The results were compared with the experimental measurements of RS. Further, the Fatemi-Socie multiaxial damage parameter combined with Roessle-Fatemi hardness method was employed to estimate fatigue crack initiation life of pitted mooring chains at various service load levels considering the effect of residual stresses. The key findings are:

- Both the HD and ND techniques have revealed the existence of high compressive RS in all measurement points with the longitudinal RS being the largest in magnitude. An exception was seen on the hoop RS measured by the HD technique at the crown where the RS were tensile.
- The radial RS that cannot be measured using the HD technique are rather considerable (approximately 25 to 50% of the longitudinal RS). The ND technique provides the measurement of the radial RS due to its capability of 3D residual strain measurement.
- Comparison of the RS at the crown calculated using the ND technique and based on 3D strain measurements with those calculated based on 2D strain measurements, where radial residual strain is set to zero, revealed 10 and 25% greater longitudinal and hoop RS respectively in the 3D calculation. This highlights the importance of 3D strain measurements in RS calculation. The HD technique is an approach that provides in-plane RS measurement only. As a result, the measurement made by this technique will not be the most accurate when the residual strains normal to the surface are considerable. Nevertheless, if the purpose of an experiment is to qualitatively compare the RS in two links to investigate the redistribution/change of RS over a service time, the HD technique could be used as a cheap and relatively quick alternative.

- The longitudinal RS (which are the largest in magnitude) at the chain crown predicted by FE modeling of proof loading are in a good agreement with the experimental measurements. Well-predicted longitudinal RS are important when fatigue crack growth is of interest as these stresses are normal to the crack faces commonly observed in the fractured chain links. The predicted radial and hoop RS are different from the in-depth measured values, as there can be some RS in the material from the heat treatment process that is carried out before proof loading. A more detailed FE model can be employed to better estimate the radial RS by considering the heat treatment process. However, the material properties at elevated temperatures are needed.
- The RS redistribution due to a corrosion pit and cyclic service loads has been studied. The redistribution of the RS has been explained by the stress concentration and cyclic plastic straining around corrosion pits that replaces the initial RS with greater RS. A current RS state can locally differ significantly from an initial RS state. This is important when the fatigue crack initiation and growth is to be studied.
- Very short crack initiation lives were predicted for the non-proof loaded chain link (i.e. no RS considered). The lives predicted for the proof loaded chain link in the cases where the initial RS state was used in the calculations were 30% shorter (more conservative) than the cases where the stable RS state was employed. The predicted crack initiation lives considering the stable RS state is about 14 to 34% of the experimental (total) life depending on the applied load. Further, the effect of mean load on the fatigue life has been successfully captured. This effect is larger when the load amplitude is smaller.

Acknowledgement

The authors would like to acknowledge Equinor for providing the test material and financially supporting the experiments through the project KPN Lifemoor (RCN contract No: 280705), Øystein Gabrielsen (Equinor) and Håkon Nordhagen (SINTEF) for help and discussion throughout the research process, SINTEF laboratory staffs for their assistance in performing the hole-drilling tests, and Rutherford Appleton Laboratory for granting the access to ENGIN-X and neutron beamtime. Also, the initial discussions and facilitation for ND testing with assoc prof Stephen Hall (Lund University, Solid Mechanics) are acknowledged.

References

1. Fontaine, E., et al., *Industry Survey of Past Failures, Pre-emptive Replacements and Reported Degradations for Mooring Systems of Floating Production Units*, in *Offshore Technology Conference*. 2014, Offshore Technology Conference.
2. Ma, K.-t., et al., *A Historical Review on Integrity Issues of Permanent Mooring Systems*, in *Offshore Technology Conference*. 2013, Offshore Technology Conference.
3. Apos, R. Souza, and S. Majhi, *Application of Lessons Learned From Field Experience to Design, Installation and Maintenance of FPS Moorings*, in *Offshore Technology Conference*. 2013, Offshore Technology Conference.
4. ISO19901-7:2013, *Stationkeeping systems for floating offshore structures and mobile offshore units*, in *part 7 of Petroleum and natural gas industries specific requirements for offshore structures*.
5. DNVGL, *Offshore Standards DNVGL-OS-E302 Offshore mooring chain*. 2015, DNV GL AS.
6. Totten, G.E., *Handbook of residual stress and deformation of steel*. 2002: ASM international.
7. Bastid, P. and S.D. Smith. *Numerical Analysis of Contact Stresses Between Mooring Chain Links and Potential Consequences for Fatigue Damage*. in *ASME 2013 32nd International*

Conference on Ocean, Offshore and Arctic Engineering. 2013. American Society of Mechanical Engineers.
8. DNVGL, *Offshore standards DNVGL-OS-E301 Position mooring*. 2015, DNV GL AS.
9. Gabrielsen, Ø., K. Larsen, and S.-A. Reinholdtsen, *Fatigue Testing of Used Mooring Chain.* ASME 2017, 2017(57632): p. V001T01A072.
10. Perez, I.M., et al. *Multiaxial Fatigue Analysis of Mooring Chain Links Under Tension Loading: Influence of Mean Load and Simplified Assessment*. in *ASME 2018 37th International Conference on Ocean, Offshore and Arctic Engineering*. 2018. American Society of Mechanical Engineers.
11. Pérez-Mora, R., et al., *Very high cycle fatigue of a high strength steel under sea water corrosion: A strong corrosion and mechanical damage coupling.* International Journal of Fatigue, 2015. **74**: p. 156-165.
12. Stiff, J.J., D.W. Smith, and N.F. Casey, *Fatigue of Mooring Chain in Air and Water - Results and Analysis*, in *Offshore Technology Conference*. 1996, Offshore Technology Conference.
13. Huang, Y., S.-T. Tu, and F.-Z. Xuan, *Pit to crack transition behavior in proportional and non-proportional multiaxial corrosion fatigue of 304 stainless steel.* Engineering Fracture Mechanics, 2017. **184**: p. 259-272.
14. Huang, Y., et al. *Numerical Investigation of Stress Concentration Factor at Irregular Corrosion Pit Under Tension-Torsion Loading*. in *ASME 2014 Pressure Vessels and Piping Conference*. 2014. American Society of Mechanical Engineers.
15. Turnbull, A., D.A. Horner, and B.J. Connolly, *Challenges in modelling the evolution of stress corrosion cracks from pits.* Engineering Fracture Mechanics, 2009. **76**(5): p. 633-640.
16. Horner, D.A., et al., *Novel images of the evolution of stress corrosion cracks from corrosion pits.* Corrosion Science, 2011. **53**(11): p. 3466-3485.
17. Xu, S.-h. and Y.-d. Wang, *Estimating the effects of corrosion pits on the fatigue life of steel plate based on the 3D profile.* International Journal of Fatigue, 2015. **72**: p. 27-41.
18. Turnbull, A., L. Wright, and L. Crocker, *New insight into the pit-to-crack transition from finite element analysis of the stress and strain distribution around a corrosion pit.* Corrosion Science, 2010. **52**(4): p. 1492-1498.
19. Zarandi, E.P. and B.H. Skallerud, *Cyclic behavior and strain energy-based fatigue damage analysis of mooring chains high strength steel.* Marine Structures, 2020. **70**: p. 102703.
20. Fatemi, A. and D.F. Socie, *A CRITICAL PLANE APPROACH TO MULTIAXIAL FATIGUE DAMAGE INCLUDING OUT-OF-PHASE LOADING.* Fatigue & Fracture of Engineering Materials & Structures, 1988. **11**(3): p. 149-165.
21. Roessle, M.L. and A. Fatemi, *Strain-controlled fatigue properties of steels and some simple approximations.* International Journal of Fatigue, 2000. **22**(6): p. 495-511.
22. Lee, T.L., et al., *Characterization of the residual stresses in spray-formed steels using neutron diffraction.* Scripta Materialia, 2015. **100**: p. 82-85.
23. Bouchard, P., et al., *Measurement of the residual stresses in a stainless steel pipe girth weld containing long and short repairs.* International Journal of Pressure Vessels and Piping, 2005. **82**(4): p. 299-310.
24. Hossain, S., et al., *Application of quenching to create highly triaxial residual stresses in type 316H stainless steels.* International journal of mechanical sciences, 2006. **48**(3): p. 235-243.
25. Abolfathi, E., et al., *The Effect of the Manufacturing Test Load on the Fatigue of Hoist Chains.* Proceedings of the Institution of Mechanical Engineers, Part B: Journal of Engineering Manufacture, 1995. **209**(2): p. 133-139.
26. ASTM, *E837-13, Standard Test Method for Determining Residual Stresses by the Hole-Drilling Strain-Gage Method*. 2013.

27. *MTS3000-RESTAN, System for measureing residual stress by hole-drilling method, EVAL back calculation software*. 2015, SINT Technology: Italy.
28. Shamsaei, N. and S.A. McKelvey, *Multiaxial life predictions in absence of any fatigue properties.* International Journal of Fatigue, 2014. **67**: p. 62-72.
29. Shamsaei, N. and A. Fatemi, *Effect of hardness on multiaxial fatigue behaviour and some simple approximations for steels.* Fatigue & Fracture of Engineering Materials & Structures, 2009. **32**(8): p. 631-646.
30. Zarandi, E.P., T.L. Lee, and B.H. Skallerud, *Data on residual stresses of mooring chains measured by neutron diffraction and hole drilling techniques.* Data in Brief, 2020. **30**: p. 105587.
31. Rampi, L., et al. *Chain Out of Plane Bending (OPB) Fatigue Joint Industry Project (JIP) Static Test Program and OPB Interlink Stiffness*. in *ASME 2016 35th International Conference on Ocean, Offshore and Arctic Engineering*. 2016. American Society of Mechanical Engineers.
32. Fernández, J., W. Storesund, and J. Navas. *Fatigue Performance of Grade R4 and R5 Mooring Chains in Seawater*. in *ASME 2014 33rd International Conference on Ocean, Offshore and Arctic Engineering*. 2014. American Society of Mechanical Engineers.
33. Brown, M., et al., *SS: Mooring System Integrity: Phase 2 Mooring Integrity JIP - Summary of Findings*, in *Offshore Technology Conference*. 2010, Offshore Technology Conference.
34. Tipton, S. and G. Shoup, *The effect of proof loading on the fatigue behavior of open link chain.* Journal of Engineering Materials and Technology, 1992. **114**(1): p. 27-33.
35. Fredheim, S., et al. *Corrosion Fatigue Testing of Used, Studless, Offshore Mooring Chain*. in *OMAE2013-10609. Nantes: 32nd International Conference on Ocean, Offshore and Arctic Engineering*. 2013.
36. Van, K.D., et al. *Criterion for high-cycle fatigue failure under multiaxial loading*. in *ICBMFF2*. 1989.
37. Smith, R., P. Watson, and T. Topper, *A stress-strain parameter for the fatigue of metals.* Journal of Materials, 1970. **5**(4): p. 767-778.

Paper 3: Data on residual stresses of mooring chains measured by neutron diffraction and hole drilling technique

Zarandi, E.P., T.L. Lee, and B.H. Skallerud, Data on residual stresses of mooring chains measured by neutron diffraction and hole drilling techniques. Data in Brief, 2020. 30: p. 105587.

https://doi.org/10.1016/j.dib.2020.105587

Data on residual stresses of mooring chains measured by neutron diffraction and hole drilling techniques

Ershad P. Zarandi*[1], Tung L. Lee[2], Bjørn H. Skallerud[1]

1. Department of Structural Engineering, Norwegian University of Science and Technology (NTNU), Richard Birkelands vei 1A, 7491, Trondheim, Norway
2. ISIS Neutron Source, Science and Technology Facilities Council, Rutherford Appleton Laboratory, Harwell Campus, OX110QX, United Kingdom

*Corresponding author: Ershad P. Zarandi (ershad.p.zarandi@ntnu.no)

Abstract

Residual stresses in large offshore mooring chains have been measured for the first time and presented in this article. Two chain links with the same size and material, one only subjected to proof load and no cyclic service loads and the other exposed to service loads as well as the proof load, were selected for the experiment. The residual stresses just below the surface were measured using the hole-drilling technique and the neutron diffraction technique was employed for deeper measurements. The data can be used to investigate residual stress redistribution in the chain links because of material removal due to corrosion and cyclic service loads that the chains are exposed to during the service time. Moreover, the data can be used to validate numerical models for predicting residual stresses. A more detailed interpretation of the data presented in this article is provided in "Experimental and numerical study of mooring chain residual stresses and implications for fatigue life" [1].

Keywords

Residual stress; Offshore mooring chain; High strength steel; Neutron diffraction; Hole drilling

Specifications table

Subject	Engineering
Specific subject area	Offshore engineering
Type of data	Table
How data were acquired	Neutron diffraction, ENGIN-X neutron diffractometer at STFC Rutherford Appleton Laboratory, United Kingdom Hole drilling, strain rosette type 1-RY61-1.5/120K, electronic measuring system (Spider8), inverted truncated-cone shaped with flat ends end mills (1-SINTCTT/1), MTS-3000 instrument at SINTEF, Norway
Data format	Raw and Analyzed

Parameters for data collection	Two chain links with the same size and material, one only subjected to proof load and no cyclic service loads and the other exposed to service loads as well as the proof load, were selected for the experiment.
Description of data collection	Residual stresses at several locations on two chain links were measured using the neutron diffraction and hole drilling techniques.
Data source location	Department of structural engineering Norwegian university of science and technology (NTNU) Trondheim, Norway
Data accessibility	With the article
Related research article	Ershad P. Zarandi, Bjørn H. Skallerud, Experimental and numerical study on mooring chain residual stresses and implications for fatigue life, International Journal of Fatigue, https://doi.org/10.1016/j.ijfatigue.2020.105530

1. Value of data

- Residual stresses in large offshore mooring chains have been measured for the first time and can be used for validation of numerical/analytical models for predicting residual stresses.
- Data can be used in the revision of offshore mooring chains design guidelines/standards.
- The fatigue life estimation of offshore mooring chains can be taken to an advanced level using the presented data.
- Data can be compared with the measurements made by other measurement techniques e.g. X-ray or deep hole drilling.
- Data can be used as an educational tool for learning how to compute residual stresses from the raw data obtained by the neutron diffraction and hole drilling techniques.

2. Data description

The raw and analyzed data on the residual stresses (RS) of offshore mooring chains is presented in this article. RS at different locations on two chain links were measured using two different techniques; Neutron Diffraction (ND) and Hole Drilling (HD). Figure 1 provides details of the reference (stress-free) samples cut from a chain link and used for the ND technique. The lattice spacings of the stress-free samples cut from the chain material are listed in Table 1. Figure 2 illustrates a schematic of the neutron beam paths at the chain crown for measuring hoop and longitudinal RS. The raw data from the ND technique (lattice spacing d) and the computed strains (ε) using procedure explained in Section 3.1.1 are provided in Table 2. The corresponding calculated RS (σ) are presented in Table 3. Figure 3 provides the details of the strain rosette used in the HD technique. The raw data obtained by HD technique test ($\varepsilon_1, \varepsilon_2,$ and ε_3) on the chain links and corresponding RS along the strain gage axes ($\tau_1, \tau_2, \tau_3, \sigma_1, \sigma_2, and\ \sigma_3$) as well as maximum and minimum principal stresses (σ_{max} and σ_{min}) and

β angles calculated following the procedure explained in 3.1.2 are provided in Table 4, Table 6, and Table 8 for the unused chain link and Table 5, Table 7, and Table 9 for the used chain link.

3. Experimental Design, Materials, and Methods

The material used in this experiment was from the mooring chain steel grade R4. Two chain links, one referred to as the used and the other as the unused, with the same size (nominal diameter of 114 mm) and made by the same manufacturer where selected. The used link had been exposed to the sea loads for 18 years before the experiment and had some corrosion evidence at the surface. The unused link was 10 years old at the time of the experiment but had never been exposed to any cyclic service loads, as it was laid on the vessel's deck during its service life. The unused link had a relatively smooth surface. The chosen links are pictured in Figure 1 in [1]. The monotonic mechanical material properties of the tested chain material are provided in [2].

Five locations on each chain link were specified for RS measurements; one at the middle of the bent part (known as the chain crown) and the others at the straight parts to compare RS in the material in welded side with those in the non-welded side (base material). The locations correspond to the critical locations from fatigue point of view. Further, marking of the measuring locations on the links was rather convenient enabling a point-to-point comparison between the two links and FE simulations. The measurement paths are shown in Figure 2 in [1]. A local cylindrical coordinate system at every location is defined such that radial stresses are along the R-axis, hoop stresses along the θ-axis, and longitudinal stresses along the Z-axis. The strain rosettes for the HD technique are glued such that the axes passing through the strain gauges no. 1 and 3, shown in Figure 3, are aligned with the hoop and longitudinal directions respectively.

3.1. Residual stress measurement techniques

3.1.1. Neutron diffraction

RS can be measured non-destructively via ND that essentially uses the lattice planes in polycrystalline materials as atomic strain gauges. The lattice strain is determined from the shift in the lattice parameter when compared to the corresponding unstressed state. The corresponding stress can then be derived from the deduced lattice strain using the material elastic stiffness. Neutrons offer significantly larger penetration depth (up to several centimeters) in most metallic materials as compared to other diffraction methods and therefore is ideal to probe stresses non-destructively deep within bulk engineering components. Assuming that the measurement axes are aligned with the principal axes, using the measured strains (ε) and Hooke's law, one can calculate the RS as follows:

$$\begin{aligned} \varepsilon_i &= (d_i - d_0)/d_0 \qquad , i = r, \theta, Z \\ \sigma_i &= \frac{E}{1+\nu}[\varepsilon_i + \frac{E}{1-2\nu}(\varepsilon_r + \varepsilon_\theta + \varepsilon_z)] \end{aligned} \tag{1}$$

where d_i are the lattice spacings of the stressed material along the three perpendicular measurement axes and d_0 denotes the average value of the lattice spacing of the stress-free crystalline material. E denotes the material's Young's modulus and ν is the Poisson's ratio provided in [2].

The uncertainties in the stresses derived ($\Delta\sigma_i$) is calculating using [3],

$$(\Delta\sigma_i)^2 = \left(\frac{A_{err}}{d_0}\right)^2 \left[\begin{array}{c} B_{err}(\Delta d_i)^2 + C_{err}^2(\Delta d_0)^2 + \\ D_{err}^2\left((\Delta d_r)^2 + (\Delta d_\theta)^2 + (\Delta d_z)^2\right) \end{array} \right]$$
$$A_{err} = \frac{E}{1+\nu}\,,\; B_{err} = \frac{1}{1-2\nu}\,,\; C_{err} = \frac{1+\nu}{1-2\nu}\,,\; D_{err} = \frac{\nu}{1-2\nu} \qquad (2)$$

In the first part of the experiment, RS at a few millimeters under the surface at the specified locations on the links were measured using this technique. The work was carried out using ENGIN-X, [4], the time-of-flight neutron diffractometer at ISIS Neutron Source, Rutherford Appleton Laboratory. The diffractometer uses a pulsed polychromatic neutron beam and is optimized for strain measurements with two detectors aligned at fixed scattering angles of $2\theta = \pm 90°$ that allows simultaneous measurement of two principal strain axes. To obtain 3D RS, the heavy chain links must be positioned in two orientations because in each orientation the lattice spacing along only two perpendicular axes could be measured. Wooden frames were designed for the links to be mounted on the rotation and translation sample stage in ENGIN-X. The experimental setup is shown in Figure 3 in [1]. A 4x4x4mm gauge volume was used to enable measurements to be completed at considerable depths below the surface of the links at a reasonably short time considering the limited beamtime access and neutrons' maximum penetration capability into steels. The center of the gauge volume was positioned at 3 and 4 mm below the surface using theodolites. At such depths, the gauge volume is completely filled with the link material and pseudo-strain effects were avoided [5]. Small T-shape samples, as illustrated in Figure 1, were cut from the straight parts (both the welded side and non-welded side) of the adjacent chain link to the unused chain link and used to determine the lattice spacing of the stress-free material (d_0). The above-mentioned setup provided the RS at 3 and 4mm below the surface, see e.g. Figure 2.

Due to the beamtime access limitation, the calculation of the RS in locations 2 and 3 is based on a 2-axis measurement (hoop and longitudinal), and thus, the radial strain was set to zero when calculating RS using Eq. (1).

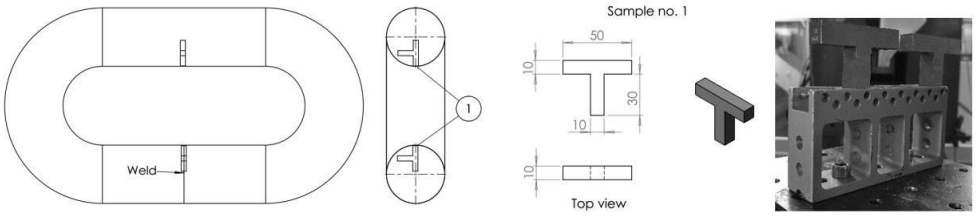

Figure 1: Details of the reference samples for the neutron diffraction technique

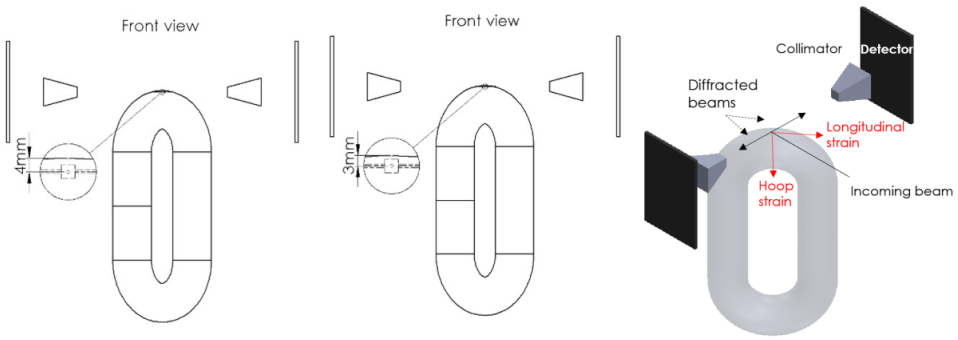

Figure 2: Schematic of the neutron beam paths at the chain crown for measuring hoop and longitudinal residual stresses

3.1.2. Hole drilling

In this technique, after preparing (dust removal and polishing) the specimen surface, a strain gauge is glued to the specimen and a small hole is drilled (or milled) incrementally into the material at the center of the strain rosette. The released strains at each increment are measured by the strain gauges. The RS are then calculated utilizing the integral method [6], measured released strains, and Hooke's law. Assuming a non-uniform stress profile through the hole in thick workpieces as:

$$\begin{aligned} p_j &= (\varepsilon_3 + \varepsilon_1)_j/2 & \bar{\mathbf{a}}\,\mathbf{P} &= \frac{E}{1+\nu}\mathbf{p} & (\sigma_1)_j &= P_j - Q_j \\ q_j &= (\varepsilon_3 - \varepsilon_1)_j/2 & \bar{\mathbf{b}}\,\mathbf{Q} &= E\,\mathbf{q} & (\sigma_3)_j &= P_j + Q_j \\ t_j &= (\varepsilon_3 + \varepsilon_1 - 2\varepsilon_2)_j/2 & \bar{\mathbf{b}}\,\mathbf{T} &= E\,\mathbf{t} & (\tau_{13})_j &= T_j \end{aligned} \qquad (3)$$

$$(\sigma_{max})_j, (\sigma_{min})_j = P_j \pm \sqrt{Q_j^2 + T_j^2}$$

$$\beta_j = \frac{1}{2} arctan(\frac{T_j}{Q_j})$$

where j refers to the serial numbers of the hole depth steps, and ε_1, ε_2, and ε_3 are measured along the three axes of the attached strain gages. $\boldsymbol{p}$, $\boldsymbol{q}$, and $\boldsymbol{t}$ denote the strain vectors, and $\mathbf{P}$, $\mathbf{Q}$, and $\mathbf{T}$ are the incremental transformed stress vectors. $\bar{\mathbf{a}}$ is the calibration constant matrix for isotropic equi-biaxial stress (P) and $\bar{\mathbf{b}}$ is the calibration constant matrix for 45° shear stress (Q) and xy shear stress (T) and their elements for different hole depths can be extracted from the tables in ASTM E837-13a [7]. σ_{max} and σ_{min} are the principal stresses and β is the angle measured clockwise from gauge 1 to the maximum principal stress axis, see Figure 3.

In the second part of the experiment, the RS at and close to the surface of the chain links were measured using this technique at SINTEF in Trondheim. Only RS at the locations around the links (locations 1, 2, and 3 in Figure 2 in [1]) were measured as the hole drilling instrument couldn't be placed in the limited space between the straight parts of the links. A thin layer of the rust on the surface was removed using very fine Scotch-Brite surface conditioning discs. The strain rosette type 1-RY61-1.5/120K, shown in Figure 3, connected to an electronic measuring system (Spider8) was used to record the strain variation during incremental hole milling using the MTS-3000 instrument. The rosettes were glued to the surfaces of the links in a way that the axes 1 and 3 of the strain gages were aligned with the hoop (θ-axis) and longitudinal (Z-axis) directions respectively, see e.g. Figure

1 in [1] and Figure 3. The instrument is equipped with an air turbine enabling the end mill to spin at a speed of 400000 rpm to avoid the introduction of RS during the milling process [8]. The end mills used in the experiment are inverted truncated-cone shaped with flat ends (1-SINTCTT/1), with a maximum shank diameter of 1.60 mm. The above-mentioned setup has provided the measurement of RS at a distance of up to 1mm below the surface. The RS were computed using the measured released strains via EVAL7.14 software.

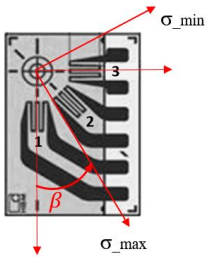

Figure 3: Details of the strain rosette used in the hole drilling technique

Table 1: Lattice spacing for the reference (stress-free) samples averaged on the three considered axes (radial, hoop, longitudinal)

	d_0 (averaged)	Uncertainty (Δd_0 averaged)
BASE	2.86783	0.000057
WELD	2.86789	0.000072

Table 2: Neutron diffraction data, measured d-spacings and corresponding computed residual strains

Location	Position below the surface [mm]	Measured Lattice Parameter, d [Å]						Strain [με]					
		Radial (R)		Hoop (θ)		Longitudinal (Z)		ε_R		ε_θ		ε_Z	
		d	Δd	d	Δd	d	Δd	ε	Δε	ε	Δε	ε	Δε
USED_LOC3	3			2.86664	0.000164	2.86339	0.000210			-414.9	60.5	-1548.2	75.9
USED_LOC4	3	2.86883	0.000105	2.86622	0.000132	2.86253	0.000109	348.7	41.7	-561.4	50.1	-1848.1	42.9
USED_LOC4	4	2.86882	0.000088	2.86638	0.000198	2.86283	0.000159	345.2	36.6	-505.6	71.8	-1743.5	58.9
USED_LOC2	3			2.86640	0.000098	2.86492	0.000212			-519.5	42.4	-1035.6	78.1
USED_LOC5	3	2.86959	0.000070	2.86636	0.000164	2.86578	0.000101	592.8	35.0	-533.5	62.4	-735.7	43.2
USED_LOC5	4	2.86898	0.000078	2.86549	0.000233	2.86332	0.000198	380.1	37.0	-836.9	85.0	-1593.5	73.4
USED_LOC1	3	2.8688	0.000071	2.86702	0.000158	2.86264	0.000133	338.2	31.8	-282.4	58.6	-1809.7	50.4
USED_LOC1	4	2.86859	0.000063	2.86811	0.00021	2.86279	0.000171	265.0	29.6	97.6	75.9	-1757.4	62.8
UNUSED_LOC3	3			2.86757	0.000141	2.86503	0.000122			-90.7	53.0	-976.3	46.9
UNUSED_LOC4	3	2.86902	0.000081	2.86705	0.000197	2.86238	0.000312	414.9	34.5	-272.0	71.5	-1900.4	110.6
UNUSED_LOC4	4	2.86858	0.000092	2.86757	0.000262	2.86059	0.000260	261.5	37.7	-90.7	93.5	-2524.6	92.8
UNUSED_LOC2	3			2.86775	0.000160	2.86026	0.000214			-48.8	61.2	-2660.5	78.7
UNUSED_LOC5	3	2.86991	0.000066	2.86669	0.000049	2.86363	0.000082	704.4	34.1	-418.4	30.4	-1485.4	38.0
UNUSED_LOC5	4	2.86906	0.000088	2.86644	0.000044	2.86321	0.000069	408.0	39.7	-505.6	29.4	-1631.9	34.7
UNUSED_LOC1	3	2.86925	0.000075	2.86845	0.000154	2.86213	0.000118	495.1	32.9	216.2	57.3	-1987.6	45.7
UNUSED_LOC1	4	2.86908	0.000066	2.86805	0.000132	2.86178	0.000122	435.9	30.4	76.7	50.1	-2109.6	46.9

Table 3: Neutron diffraction data, computed residual stresses

Location	Position below the surface [mm]	Stress [MPA], based on 3 axes measurements						Stress [MPA], based on 2 axes measurements (i.e. $\varepsilon_R = 0$ in Equation (1))					
		Radial (R)		Hoop (θ)		Longitudinal (Z)		Radial (R)		Hoop (θ)		Longitudinal (Z)	
		σ	$\Delta\sigma$	σ	$\Delta\sigma$	σ	$\Delta\sigma$	σ	$\Delta\sigma$	σ	$\Delta\sigma$	σ	$\Delta\sigma$
USED_LOC3	3							-234.0	16.3	-199.7	18.9	-379.8	21.3
USED_LOC4	3	-190.2	10.9	-334.8	11.6	-539.3	11.0	-287.2	11.1	-253.3	14.3	-457.8	13.1
USED_LOC4	4	-172.1	12.9	-307.3	15.5	-504.0	14.4	-268.1	15.6	-233.5	20.3	-430.3	18.3
USED_LOC2	3							-185.4	14.4	-188.5	14.9	-270.5	20.6
USED_LOC5	3	13.6	11.1	-165.4	13.2	-197.6	11.6	-151.3	12.6	-171.2	17.1	-203.4	14.1
USED_LOC5	4	-184.0	15.0	-377.4	18.3	-497.6	17.3	-289.7	18.9	-298.5	24.3	-418.8	22.5
USED_LOC1	3	-155.3	10.9	-253.9	12.8	-496.7	12.1	-249.4	13.0	-187.4	16.7	-430.1	15.4
USED_LOC1	4	-124.1	12.9	-150.7	16.1	-445.5	15.0	-197.8	16.5	-97.5	21.5	-392.3	19.4
UNUSED_LOC3	3							-127.2	11.9	-87.1	15.2	-227.8	14.3
UNUSED_LOC4	3	-143.5	16.9	-252.7	19.0	-511.5	22.2	-258.9	21.7	-191.2	23.8	-450.0	30.0
UNUSED_LOC4	4	-239.0	17.1	-295.0	20.8	-681.8	20.7	-311.7	22.2	-192.5	27.5	-579.3	27.4
UNUSED_LOC2	3							-322.9	16.7	-192.3	19.3	-607.3	22.0
UNUSED_LOC5	3	-31.0	8.5	-209.5	8.2	-379.0	8.8	-226.9	8.2	-196.2	9.5	-365.7	10.7
UNUSED_LOC5	4	-141.3	9.0	-286.5	8.3	-465.5	8.6	-254.8	7.6	-225.9	9.0	-404.9	9.9
UNUSED_LOC1	3	-73.4	10.6	-117.8	12.4	-468.0	11.4	-211.1	12.3	-86.3	16.1	-436.5	14.3
UNUSED_LOC1	4	-121.1	9.9	-178.2	11.3	-525.6	11.0	-242.3	11.6	-126.3	14.6	-473.7	14.1

Table 4: Hole drilling data at the crown (location 1) of the unused link

Depth [mm]	$\boldsymbol{\varepsilon_1}$ $[\mu\varepsilon]$	$\boldsymbol{\varepsilon_2}$ $[\mu\varepsilon]$	$\boldsymbol{\varepsilon_3}$ $[\mu\varepsilon]$	$\boldsymbol{\sigma_{min}}$ $[MPa]$	$\boldsymbol{\sigma_{max}}$ $[MPa]$	$\boldsymbol{\beta}$ [°]	$\boldsymbol{\sigma}$ **on 1** $[MPa]$	$\boldsymbol{\tau}$ **on 1** $[MPa]$	$\boldsymbol{\sigma}$ **on 2** $[MPa]$	$\boldsymbol{\tau}$ **on 2** $[MPa]$	$\boldsymbol{\sigma}$ **on 3** $[MPa]$	$\boldsymbol{\tau}$ **on 3** $[MPa]$
0.025	2.47	0.25	-0.60	-115	-84	10	-85.3	-5.3	-94.4	14.3	-114.0	5.3
0.075	3.25	6.47	9.47	-199	-43	-5	-44.1	14.3	-135.1	76.8	-197.6	-14.3
0.125	3.23	13.57	21.51	-237	-17	-6	-19.4	21.2	-148.2	107.6	-234.7	-21.2
0.175	1.77	22.07	36.94	-254	-2	-5	-4.1	22.1	-150.2	124.1	-252.2	-22.1
0.225	-0.84	31.39	54.84	-266	5	-4	4.0	20.0	-150.0	134.1	-264.2	-20.0
0.275	-4.39	41.12	74.59	-277	9	-3	8.0	16.8	-151.0	142.3	-276.5	-16.8
0.325	-8.72	51.03	95.73	-293	8	-3	7.7	13.3	-155.7	150.1	-292.5	-13.3
0.375	-13.73	60.92	117.88	-311	9	-2	8.3	10.4	-161.6	159.5	-310.6	-10.4
0.425	-19.30	70.66	140.72	-322	11	-1	11.1	7.4	-162.6	166.2	-321.3	-7.4
0.475	-25.38	80.15	163.91	-342	10	-1	10.4	5.2	-170.7	175.9	-341.5	-5.2
0.525	-31.87	89.26	187.16	-353	12	0	12.0	3.1	-173.5	182.3	-352.6	-3.1
0.575	-38.72	97.92	210.15	-367	12	0	12.2	1.5	-178.8	189.6	-366.9	-1.5
0.625	-45.85	106.04	232.62	-383	12	0	11.8	0.1	-185.7	197.4	-383.0	-0.1
0.675	-53.18	113.55	254.32	-388	17	0	16.6	-1.3	-184.3	202.2	-387.8	1.3
0.725	-60.65	120.40	275.04	-401	17	0	16.8	-2.5	-189.6	208.9	-401.1	2.5
0.775	-68.18	126.55	294.64	-398	24	1	23.9	-3.9	-183.4	211.1	-398.3	3.9
0.825	-75.69	132.00	312.99	-396	28	1	27.4	-5.3	-178.9	211.6	-395.8	5.3
0.875	-83.13	136.76	330.04	-391	35	1	35.0	-6.9	-170.8	212.8	-390.5	6.9
0.925	-90.44	140.87	345.79	-383	51	1	51.1	-8.5	-157.4	217.0	-382.9	8.5
0.975	-97.55	144.35	360.24	-367	74	1	73.9	-10.1	-136.1	220.1	-366.3	10.1

Table 5: Hole drilling data at the crown (location 1) of the used link

Depth [mm]	ε_1 [$\mu\varepsilon$]	ε_2 [$\mu\varepsilon$]	ε_3 [$\mu\varepsilon$]	σ_{min} [MPa]	σ_{max} [MPa]	β [°]	σ on 1 [MPa]	τ on 1 [MPa]	σ on 2 [MPa]	τ on 2 [MPa]	σ on 3 [MPa]	τ on 3 [MPa]
0.025	0.28	-1.30	-2.15	-37	12	-11	10.2	9.1	-21.8	22.9	-35.7	-9.1
0.075	-1.77	3.11	5.40	-162	15	-9	10.1	28.6	-102.0	83.4	-156.7	-28.6
0.125	-4.42	8.56	14.93	-213	23	-9	17.4	35.5	-130.6	112.5	-207.6	-35.5
0.175	-8.20	15.67	27.78	-235	31	-8	26.0	37.4	-139.1	127.7	-229.5	-37.4
0.225	-12.99	23.78	42.97	-246	38	-8	33.1	37.6	-141.5	137.0	-241.0	-37.6
0.275	-18.66	32.51	59.84	-256	44	-7	38.9	37.6	-143.5	144.8	-250.7	-37.6
0.325	-25.08	41.62	77.94	-267	47	-7	41.9	37.9	-148.1	152.2	-262.4	-37.9
0.375	-32.13	50.93	96.91	-282	49	-7	44.5	38.7	-154.9	160.8	-277.0	-38.7
0.425	-39.69	60.30	116.42	-288	53	-7	48.8	38.7	-156.3	166.4	-283.9	-38.7
0.475	-47.64	69.58	136.18	-303	55	-6	50.9	39.4	-163.2	174.7	-298.4	-39.4
0.525	-55.87	78.63	155.91	-309	58	-6	53.6	39.0	-164.8	179.3	-305.1	-39.0
0.575	-64.29	87.35	175.36	-318	60	-6	55.9	38.7	-167.7	184.9	-313.8	-38.7
0.625	-72.79	95.61	194.28	-329	61	-6	57.1	38.4	-172.2	190.9	-324.8	-38.4
0.675	-81.30	103.35	212.51	-331	65	-5	61.1	37.3	-170.4	194.2	-327.3	-37.3
0.725	-89.74	110.49	229.88	-340	67	-5	63.2	36.7	-173.3	199.8	-336.4	-36.7
0.775	-98.05	117.02	246.29	-338	71	-5	68.1	35.2	-168.5	201.3	-334.6	-35.2
0.825	-106.18	122.93	261.69	-336	74	-5	70.8	33.8	-164.8	201.8	-332.8	-33.8
0.875	-114.09	128.24	276.04	-332	79	-5	76.8	32.7	-159.2	203.3	-329.8	-32.7
0.925	-121.73	132.97	289.33	-330	91	-4	88.8	32.6	-151.8	208.1	-327.3	-32.6
0.975	-129.08	137.16	301.60	-319	110	-4	107.5	32.6	-136.9	211.8	-316.1	-32.6

Table 6: Hole drilling data at the straight part, welded side, (location 2) of the unused link

Depth [mm]	$\boldsymbol{\varepsilon_1}$ $[\mu\varepsilon]$	$\boldsymbol{\varepsilon_2}$ $[\mu\varepsilon]$	$\boldsymbol{\varepsilon_3}$ $[\mu\varepsilon]$	$\boldsymbol{\sigma_{min}}$ $[MPa]$	$\boldsymbol{\sigma_{max}}$ $[MPa]$	$\boldsymbol{\beta}$ [°]	$\boldsymbol{\sigma}$ **on 1** $[MPa]$	$\boldsymbol{\tau}$ **on 1** $[MPa]$	$\boldsymbol{\sigma}$ **on 2** $[MPa]$	$\boldsymbol{\tau}$ **on 2** $[MPa]$	$\boldsymbol{\sigma}$ **on 3** $[MPa]$	$\boldsymbol{\tau}$ **on 3** $[MPa]$
0.025	3.66	2.78	0.71	-280	-220	-15	-223.6	14.9	-264.8	26.3	-276.2	-14.9
0.075	11.65	17.03	20.35	-406	-215	-2	-214.7	5.1	-315.3	95.5	-405.7	-5.1
0.125	19.50	32.79	43.32	-466	-196	0	-196.4	2.0	-333.2	134.9	-466.1	-2.0
0.175	26.83	51.06	71.97	-491	-175	0	-175.2	1.5	-334.7	158.0	-491.1	-1.5
0.225	33.33	70.87	104.55	-502	-158	0	-158.3	1.8	-331.9	171.8	-501.9	-1.8
0.275	38.79	91.42	139.64	-508	-146	0	-145.6	2.0	-328.8	181.3	-508.1	-2.0
0.325	43.15	112.11	176.13	-517	-141	0	-141.1	1.7	-331.0	188.2	-517.5	-1.7
0.375	46.39	132.45	213.14	-526	-136	0	-135.6	0.5	-331.4	195.2	-526.1	-0.5
0.425	48.53	152.07	250.00	-518	-122	0	-122.0	-1.2	-318.9	198.1	-518.1	1.2
0.475	49.66	170.72	286.18	-529	-121	0	-121.3	-3.4	-321.9	204.0	-529.4	3.4
0.525	49.85	188.22	321.28	-528	-115	1	-115.1	-6.1	-315.3	206.3	-527.6	6.1
0.575	49.19	204.44	355.02	-536	-115	1	-115.6	-9.0	-316.6	209.9	-535.4	9.0
0.625	47.80	219.34	387.17	-552	-121	2	-121.8	-12.0	-324.9	215.0	-551.9	12.0
0.675	45.75	232.90	417.59	-552	-116	2	-116.3	-15.0	-318.9	217.5	-551.3	15.0
0.725	43.15	245.14	446.18	-574	-126	2	-126.6	-17.7	-332.1	223.3	-573.1	17.7
0.775	40.07	256.10	472.89	-572	-121	3	-121.8	-20.2	-326.3	224.7	-571.2	20.2
0.825	36.61	265.85	497.69	-580	-127	3	-128.4	-21.9	-331.7	225.3	-578.9	21.9
0.875	32.83	274.45	520.59	-582	-126	3	-126.8	-23.3	-330.3	226.8	-580.4	23.3
0.925	28.80	281.98	541.63	-576	-109	3	-110.1	-24.4	-317.9	232.2	-574.5	24.4
0.975	24.58	288.53	560.85	-551	-76	3	-77.4	-25.0	-288.5	236.1	-549.6	25.0

Table 7: Hole drilling data at the straight part, welded side, (location 2) of the used link

Depth [mm]	ε_1 $[\mu\varepsilon]$	ε_2 $[\mu\varepsilon]$	ε_3 $[\mu\varepsilon]$	σ_{min} $[MPa]$	σ_{max} $[MPa]$	β [°]	σ on 1 $[MPa]$	τ on 1 $[MPa]$	σ on 2 $[MPa]$	τ on 2 $[MPa]$	σ on 3 $[MPa]$	τ on 3 $[MPa]$
0.025	1.41	0.77	0.05	-173	-109	-1	-108.8	0.8	-141.6	31.9	-172.6	-0.8
0.075	5.50	9.80	13.99	-279	-124	0	-124.4	0.1	-201.9	77.3	-279.1	-0.1
0.125	9.79	19.80	30.50	-333	-129	4	-129.5	-13.0	-218.1	101.5	-332.6	13.0
0.175	14.33	31.29	51.48	-362	-127	6	-129.7	-25.7	-218.8	114.8	-359.3	25.7
0.225	18.92	43.54	75.66	-380	-126	8	-130.3	-34.2	-218.6	122.5	-375.3	34.2
0.275	23.39	56.20	102.07	-394	-126	8	-132.0	-38.6	-221.6	128.2	-388.3	38.6
0.325	27.60	69.07	129.89	-410	-133	8	-138.4	-39.7	-231.6	132.9	-404.3	39.7
0.375	31.45	82.00	158.53	-426	-138	8	-143.9	-39.2	-243.3	138.6	-421.0	39.2
0.425	34.85	94.84	187.47	-430	-137	7	-141.7	-37.7	-245.9	141.9	-425.5	37.7
0.475	37.74	107.44	216.31	-450	-145	7	-149.2	-37.0	-260.4	148.2	-445.6	37.0
0.525	40.10	119.63	244.73	-460	-147	7	-151.1	-37.0	-266.1	152.0	-455.1	37.0
0.575	41.90	131.26	272.46	-477	-153	7	-157.7	-38.0	-277.1	157.4	-472.5	38.0
0.625	43.13	142.19	299.29	-502	-164	7	-169.3	-40.3	-293.0	164.0	-497.4	40.3
0.675	43.82	152.33	325.04	-515	-167	7	-172.0	-42.8	-298.0	168.8	-509.6	42.8
0.725	43.98	161.63	349.57	-546	-182	7	-187.5	-46.0	-317.6	176.1	-539.6	46.0
0.775	43.63	170.06	372.78	-556	-184	7	-189.8	-47.9	-321.8	179.9	-549.6	47.9
0.825	42.81	177.63	394.58	-571	-192	7	-198.8	-48.7	-333.0	183.0	-564.7	48.7
0.875	41.57	184.41	414.93	-582	-196	7	-202.6	-48.5	-340.7	186.6	-575.8	48.5
0.925	39.94	190.44	433.79	-587	-190	7	-195.8	-47.7	-341.0	192.9	-581.6	47.7
0.975	37.97	195.78	451.17	-574	-168	6	-173.1	-45.3	-325.9	198.1	-569.4	45.3

Table 8: Hole drilling data at the straight part, non-welded side, (location 3) of the unused link

Depth [mm]	$\boldsymbol{\varepsilon_1}$ $[\mu\varepsilon]$	$\boldsymbol{\varepsilon_2}$ $[\mu\varepsilon]$	$\boldsymbol{\varepsilon_3}$ $[\mu\varepsilon]$	$\boldsymbol{\sigma_{min}}$ $[MPa]$	$\boldsymbol{\sigma_{max}}$ $[MPa]$	$\boldsymbol{\beta}$ [°]	$\boldsymbol{\sigma}$ **on 1** $[MPa]$	$\boldsymbol{\tau}$ **on 1** $[MPa]$	$\boldsymbol{\sigma}$ **on 2** $[MPa]$	$\boldsymbol{\tau}$ **on 2** $[MPa]$	$\boldsymbol{\sigma}$ **on 3** $[MPa]$	$\boldsymbol{\tau}$ **on 3** $[MPa]$
0.025	-1.01	-0.50	-1.00	-253	-157	-1	-157.4	2.1	-207.3	47.8	-253.0	-2.1
0.075	10.78	15.74	21.27	-483	-318	5	-318.8	-13.9	-386.6	81.7	-482.2	13.9
0.125	23.69	34.81	47.34	-555	-334	0	-333.9	0.9	-445.5	110.7	-555.3	-0.9
0.175	37.50	58.39	79.49	-564	-293	-5	-294.8	21.3	-450.0	134.0	-562.7	-21.3
0.225	50.25	84.46	115.18	-554	-241	-7	-245.9	37.3	-435.1	151.9	-549.7	-37.3
0.275	61.07	111.54	152.75	-541	-196	-8	-202.5	46.1	-414.8	166.2	-535.0	-46.1
0.325	69.74	138.51	191.10	-536	-169	-8	-175.0	47.7	-400.2	177.5	-530.0	-47.7
0.375	76.37	164.59	229.50	-537	-154	-6	-158.6	43.0	-388.6	187.0	-532.5	-43.0
0.425	81.23	189.28	267.41	-521	-131	-5	-134.4	34.3	-360.6	192.0	-518.4	-34.3
0.475	84.58	212.25	304.43	-530	-130	-3	-131.0	23.6	-353.6	199.0	-529.0	-23.6
0.525	86.65	233.32	340.24	-526	-122	-2	-122.4	13.0	-337.2	201.8	-526.0	-13.0
0.575	87.61	252.42	374.54	-533	-121	0	-121.4	2.8	-329.8	205.6	-532.6	-2.8
0.625	87.57	269.59	407.12	-546	-124	1	-124.5	-4.6	-330.7	210.8	-546.1	4.6
0.675	86.58	284.87	437.76	-536	-108	1	-108.4	-9.6	-312.4	213.6	-535.6	9.6
0.725	84.67	298.38	466.32	-542	-102	1	-102.5	-11.3	-311.0	219.9	-542.2	11.3
0.775	81.90	310.24	492.72	-520	-75	1	-75.4	-10.7	-286.7	222.0	-519.4	10.7
0.825	78.31	320.57	516.94	-503	-55	1	-55.1	-7.7	-271.2	223.8	-502.7	7.7
0.875	74.00	329.50	538.99	-475	-22	1	-21.7	-4.0	-244.5	226.7	-475.2	4.0
0.925	69.10	337.17	558.96	-440	27	0	26.5	-0.4	-206.3	233.2	-439.8	0.4
0.975	63.76	343.70	576.97	-387	89	0	89.4	1.5	-150.2	238.1	-386.8	-1.5

Table 9: Hole drilling data at the straight part, non-welded side, (location 3) of the used link

Depth [mm]	$\boldsymbol{\varepsilon_1}$ $[\boldsymbol{\mu\varepsilon}]$	$\boldsymbol{\varepsilon_2}$ $[\boldsymbol{\mu\varepsilon}]$	$\boldsymbol{\varepsilon_3}$ $[\boldsymbol{\mu\varepsilon}]$	$\boldsymbol{\sigma_{min}}$ $[\boldsymbol{MPa}]$	$\boldsymbol{\sigma_{max}}$ $[\boldsymbol{MPa}]$	$\boldsymbol{\beta}$ [°]	$\boldsymbol{\sigma}$ **on 1** $[\boldsymbol{MPa}]$	$\boldsymbol{\tau}$ **on 1** $[\boldsymbol{MPa}]$	$\boldsymbol{\sigma}$ **on 2** $[\boldsymbol{MPa}]$	$\boldsymbol{\tau}$ **on 2** $[\boldsymbol{MPa}]$	$\boldsymbol{\sigma}$ **on 3** $[\boldsymbol{MPa}]$	$\boldsymbol{\tau}$ **on 3** $[\boldsymbol{MPa}]$
0.025	-0.52	-2.79	-2.60	-40	-9	88	-40.4	-1.2	-23.6	-15.6	-9.2	1.2
0.075	3.88	4.39	2.70	-170	-84	-38	-116.8	41.7	-169.0	10.5	-137.7	-41.7
0.125	9.30	14.19	10.59	-268	-125	-30	-161.6	62.2	-259.1	35.3	-232.2	-62.2
0.175	16.44	28.75	23.47	-338	-154	-26	-188.7	71.8	-318.0	57.5	-303.6	-71.8
0.225	24.73	47.07	40.78	-392	-175	-22	-206.6	76.3	-359.8	76.8	-360.2	-76.3
0.275	33.63	68.23	61.82	-436	-191	-20	-220.0	78.7	-392.4	93.7	-407.5	-78.7
0.325	42.72	91.39	85.81	-478	-208	-18	-233.9	80.2	-422.8	108.8	-451.4	-80.2
0.375	51.64	115.79	111.95	-516	-221	-17	-245.7	82.1	-450.3	122.5	-490.8	-82.1
0.425	60.09	140.79	139.51	-534	-221	-16	-244.4	81.9	-459.8	133.4	-511.2	-81.9
0.475	67.86	165.79	167.81	-564	-231	-15	-252.9	82.8	-480.5	144.7	-542.4	-82.8
0.525	74.80	190.32	196.26	-578	-231	-14	-251.1	81.6	-485.8	153.1	-557.2	-81.6
0.575	80.81	213.98	224.38	-594	-233	-13	-252.2	80.2	-493.7	161.3	-574.8	-80.2
0.625	85.84	236.45	251.77	-616	-242	-12	-259.5	78.6	-507.6	169.6	-598.6	-78.6
0.675	89.89	257.51	278.10	-622	-240	-12	-255.8	75.0	-506.5	175.7	-607.2	-75.0
0.725	92.98	276.99	303.16	-645	-252	-11	-265.1	71.8	-520.0	183.1	-631.3	-71.8
0.775	95.17	294.80	326.76	-645	-248	-10	-259.0	66.4	-512.4	187.0	-633.1	-66.4
0.825	96.53	310.91	348.80	-646	-248	-9	-257.8	60.1	-507.1	189.2	-636.2	-60.1
0.875	97.14	325.31	369.21	-643	-244	-8	-251.2	53.9	-497.2	192.1	-635.3	-53.9
0.925	97.09	338.08	387.97	-635	-229	-7	-235.1	49.3	-481.5	197.0	-629.1	-49.3
0.975	96.47	349.28	405.09	-605	-195	-6	-199.5	44.5	-444.4	200.4	-600.4	-44.5

Acknowledgement

The authors would like to acknowledge Equinor for providing the test material and financially supporting the experiments through the project KPN Lifemoor (RCN contract No: 280705), SINTEF laboratory staffs for their assistance in performing the hole-drilling tests, and Rutherford Appleton Laboratory for granting the access to ENGIN-X and neutron beamtime. Also, the initial discussions and facilitation for ND testing with assoc prof Stephen Hall (Lund University, Solid Mechanics) are acknowledged.

Competing interests

None.

References

[1] Zarandi, E.P. and B.H. Skallerud, *Experimental and numerical study of mooring chain residual stresses and implications for fatigue life*. International Journal of Fatigue, 2020. **135**: p. 105530.

[2] Zarandi, E.P. and B.H. Skallerud, *Cyclic behavior and strain energy-based fatigue damage analysis of mooring chains high strength steel.* Marine Structures, 2020. **70**: p. 102703.

[3] Reimers, W., et al., *Neutrons and synchrotron radiation in engineering materials science*. From Fundamentals to Material and component characterization, KGaA, Weinhein: Wiley-VCH Verlag GmbH & Co. 2008.

[4] Santisteban, J., et al., *ENGIN-X: a third-generation neutron strain scanner*. Journal of Applied Crystallography, 2006. **39**(6): p. 812-825.

[5] Lee, T.L., et al., *Characterization of the residual stresses in spray-formed steels using neutron diffraction.* Scripta Materialia, 2015. **100**: p. 82-85.

[6] Schajer, G.J.J.o.E.M. and Technology, *Measurement of non-uniform residual stresses using the hole-drilling method. Part I—Stress calculation procedures.* 1988. **110**(4): p. 338-343.

[7] ASTM, *E837-13, Standard Test Method for Determining Residual Stresses by the Hole-Drilling Strain-Gage Method*. 2013.

[8] *MTS3000-RESTAN, System for measureing residual stress by hole-drilling method, EVAL back calculation software*. 2015, SINT Technology: Italy.